High Reynolds Number Horizontal and Vertical Axis Wind Turbine Experiments

Mark Aaron Mattone Miller

A Dissertation
Presented to the Faculty
of Princeton University
in Candidacy for the Degree
of Doctor of Philosophy

Recommended for Acceptance
by the Department of
Mechanical and Aerospace Engineering
Adviser: Professor Marcus Hultmark

November 2018

Abstract

The large scale of modern wind turbines has created a disconnect between laboratory experiments and field-scale operation. Due to the added complexity of a non-dimensional frequency, based on the turbine angular velocity, conventional wind tunnel facilities are not able to match all non-dimensional parameters between laboratory and field-scale. The ever-increasing size of wind turbines continues to highlight this discrepancy, yet more is demanded of new models and simulations in the form of accuracy with actual turbine operation. To address this issue a unique wind tunnel facility has been employed to study the Reynolds number scaling of both horizontal and vertical axis wind turbine geometries, or HAWTs and VAWTs, respectively. With the additional control provided over the fluid density, Reynolds numbers and non-dimensional rotational rates are matched between model and full-scale. To operate successfully in the pressurized environment, an entire suite of models, sensors, and test platforms were developed. This allowed for highly controlled and accurate measurements to be made of wind turbine performance with respect to both power and thrust coefficients.

The results indicate that a Reynolds number based on the flow at the rotor chord is the preferred way to scale Reynolds number behavior for both horizontal and vertical axis wind turbine models. For the first time, a wide enough range of Re was explored to confirm the value for which the models achieved Reynolds number invariance. In addition, the performance of the tripped HAWT rotor was explored with a well-characterized trip geometry and it was observed that the threshold to achieve invariance in the power coefficient was reduced from the un-tripped case. Vertical axis experiments included a study of several solidity values across a range of Reynolds numbers with the goal of adding to the understanding of scaling effects for a wide range of VAWT designs. The conclusions drawn, and reference data gathered during the course of these experiments is now available for use as a validation case for further

development of models, comparison to numerical simulations, and for increasing the knowledge base of canonical HAWT and VAWT operation.

Acknowledgements

My time at Princeton would not have been possible without the support and guidance of a great number of people. The first of which is my advisor, Marcus Hultmark. Your infectious optimism and continual interest in the project helped to propel me through the very challenging parts of this work. I am very grateful that you accepted me into your group and never ceased to believe in everyone's ability to succeed. It has been truly inspiring to work with you, and I have learned so much from the amazing example that you set for your students. No doubt the incredible esprit de corps we all were lucky enough to experience was thanks to your efforts. My gratitude also goes out to our lab, what a great, supportive, and thoughtful group of people. I would especially like to thank my partners in crime Clay Byers and Matthew Fu. In addition to the trials and tribulations of general exams, you both helped me with many research hurdles and were great support along the way. There are a number of people who really deserve more than a mention in a thesis, graduation would not have been possible without their help. Thanks to Dan Hoffman for everything, especially our coffee breaks and buffet trips. Also thanks to Glenn Northey who generously gave his time and vast knowledge to help us get this project manufactured and off the ground. Also thanks to Lex Smits for letting me borrow your incredible wind tunnel for five whole years. There were a number of collaborators who helped with numerous aspects of this work, and I am indebted to them all. Thanks to Janik Kiefer for all the climbing in and out of the wind tunnel, and the ten thousand other things you helped me with. For all of the assistance with the VAWT, I have Subrahmanyam Duvvuri to thank, that project would not have happened without you. Also thanks to Arthur Phidd, Christy Elford, Lucy Tang, Soumya Sudhakar, Benhur Johnson, Stefan Scholten, Claudia Brunner, and Melissa Fan for all your hard work on the wind turbine project. Finally a thank you to the machinists Barry Runner and Larry

McIntyre at the SEAS shop and Bill Dix plus his cohort at the Physics machine shop, this project literally would not have been built without your help.

Outside the world of Princeton, the person I owe so much to is Elizabeth. You helped me in so many ways that I will not even attempt to list them all. The support, optimism, friendship, and help you provided me in this adventure have been tremendous. I would also be remiss if I did not thank my classmates. You were great study partners, GSG party-goers, sushi-palace eaters, general-exams quizzers, and overall a great group of friends. Finally, my thanks goes out to my parents who gave so much of themselves to help me get to where I am today. Your support and guidance throughout my entire life has led me here, and for that I am eternally grateful.

This work was supported by the National Science Foundation (grand CBET-1435254 and CBET-1652583) and a grant from the Andlinger Center for Energy and the Environment at Princeton University.

This dissertation carries T#3365 in the records of the Department of Mechanical and Aerospace Engineering.

To my parents.

Contents

List of Tables

List of Figures

Chapter 1

Introduction

1.1 Motivation

The design of modern wind turbines has been defined by an ever-increasing physical scale, with new, commercially available rotors exceeding 200 meters in diameter. The drive towards larger rotors is primarily motivated by reducing overall turbine cost. This is particularly relevant for offshore wind farms where a considerable portion of the total expense is the foundation materials and installation, with one report citing a value of 25% compared with the turbine cost plus installation of 33% (Blanco, 2009). Furthermore, the operations and maintenance (O&M) expenses must be included which may account for 5 to 20% over the lifetime of a farm. Newer, larger turbines means less units to maintain, per kilo-Watt-hour produced, than a farm comprised of smaller units. These reasons make it clear why the current trend is to reduce the number of turbines by increasing the capacity of each individual unit, especially for offshore, but also for onshore wind farm installations (Cotrell et al., 2014). While not as costly to install or maintain as offshore units, land-based turbines are also predicted to continue increasing in rotor diameter, although at a slower rate than offshore due to restrictions on rotor blade length and tower diameter when transporting

over land (Cotrell et al., 2014). Larger rotors bring some disadvantages as well, notably challenges during construction and installation where specialized equipment is needed. Alternative technologies such as on-site tower manufacturing and segmented blades may help alleviate some of these restrictions for onshore installations (Cotrell et al., 2014). Large offshore turbines may be manufactured near the sea port and therefore face less restrictions for transportation, although as mentioned installation and maintenance can be costly.

Despite the technical and installation challenges faced when developing large wind turbine rotors, the general trend has been to continue producing larger diameters with the average onshore turbine increasing from 73 (m) in 2005 to 102 (m) in 2015 (40% gain), while offshore units increased from 90 to 119 (m) (32% gain) in the same period. New units are projected to exceed 135 meters onshore and 190 offshore by 2030, with most experts agreeing that this will be the major driver in further reducing the cost of wind energy (Wiser et al., 2016)[1]. One of the major challenges facing the wind energy sector today is how to adequately model these large machines while increasing the predictive accuracy of the current design tools. In the past, incremental growth of turbine scale made adaptation of modeling and design tools an equally incremental process. New designs require increased accuracy while reducing uncertainty so that additional optimization can be performed and overall cost can continue to be reduced. While many advancements have been made in the modeling and design of composite materials, generators, power inverters and transmission, and control and monitoring systems, the methods for determining the input loads from the wind have remained relativity constant since the early days of wind energy. The fundamental method for determining aerodynamic loads is known as Blade Element Momentum theory (or BEM) and has remained essentially the same since being developed in 1935 by Glauert (Glauert, 1935; Hansen, 2007; Madsen et al., 2007). It is widely used in industry

[1]Since this review was published, several on-shore turbines have been developed at $D \geq 158$ (m).

due to the low computational cost and the legacy of modeling and validation efforts on which the most current iterations are based. Any deficiencies in the method are typically overcome by applying various engineering-type models to account for things such as three-dimensional and rotational effects, high thrust loadings, yawed and turbulent inflow, and many others, some of which are proprietary developments by the manufacturers. The strength of BEM is that if used within the confines of the empirical data upon which the corrections are based, it can work quite well for predicting the rotor loads. However, the modeling approach does not lead to additional insight when off-design conditions are encountered; as can be the case in a real wind farm. Therefore designs must be conservative and are typically evolutionary instead of revolutionary, as evidenced by the four-plus decade popularity of the three-bladed, horizontal-axis wind turbine.

The increasing pace of development for large wind turbines highlights the need for additional understanding of wind turbine aerodynamics at large to very large scales. As discussed further in the following sections, increasing physical scale or size is the equivalent to increasing the non-dimensional, aerodynamic parameter known as the Reynolds number, which describes the ratio between inertial and viscous forces in the flow. Traditional wind tunnel facilities, where the test section dimensions are on the order of a meter, cannot be used to study full-scale aerodynamics of wind turbines because the Reynolds numbers possible are two orders of magnitude (or more) below the full-size wind turbine (as discussed in greater detail in section 1.2). In the past, two methodologies have been adopted to avoid the scaling/Reynolds number issue. The most obvious of which is simply to build and test full-size models in the field (requiring the costly construction of a full-scale prototype). Field tests do have drawbacks other than cost such as large uncertainties about inflow conditions and rotor geometry unknowns (details of the aerodynamic surfaces are often proprietary, making conclusions about specific input parameters difficult). The other method is

to use very large facilities with near-full-scale models to capture information about the aerodynamics. Large-scale wind tunnel testing has only been completed for a handful of cases due to the cost and complexity associated with using these facilities (Simms et al., 2001; Snel et al., 2007). Considering the difficulty of matching Reynolds number effects, model testing was listed among the biggest research challenges facing the wind energy sector in a recent review article (van Kuik et al., 2016).

In this thesis a new methodology is developed for testing wind turbine models under controlled inflow conditions, while still matching the important aerodynamic parameters of the full-scale units including the large Reynolds numbers. This was accomplished using a compressed air wind tunnel known as the High Reynolds number Test Facility (HRTF). With this specialized wind tunnel, careful studies can be made of various inflow parameter effects on the performance of wind turbine models, including Reynolds number effects, over a range on the same order of magnitude as the full-scale. A single person may run this facility and acquire data at many different operating points, drastically lowering cost and complexity compared to other experiments where the same aerodynamic parameters were matched. The novel approach of these experiments makes for a valuable reference point and validation tool when developing models, performing numerical simulations, and possibly as part of future wind turbine designs.

The following sections of this chapter provide additional background and detail on the Reynolds-dependent operation of wind turbines. Non-dimensional forms of the governing equations are developed which give the proper scaling parameters for compressible flows with rotation, directly applicable to numerical and experimental work in this field. An overview of the horizontal axis wind turbine (HAWT) is then given with regard to its dependency on Reynolds number effects. Following this the vertical axis wind turbine (VAWT) is discussed. Although less commercially successful than the HAWT, the VAWT also suffers from a lack of understanding

regarding Reynolds number effects for similar reasons. The VAWT geometry and complex method of operation (relative to the standard HAWT) is discussed and a separate review of the relevant literature on Reynolds number effects is given. This chapter is concluded by a summary of motivations in light of current literature.

1.2 Dynamic Similarity and Scaling

Dynamic similarity between two flows implies that experimental data gathered from one can be used to predict the behavior of the other. This is the fundamental approach taken by experimental fluid mechanics in which tests on models can be used to predict the performance of full-scale prototypes such as airplanes, ships, rockets, and wind turbines. The core aspect of dynamic similarity is the matching of all relevant non-dimensional parameters to the problem at hand. Determining these parameters can be accomplished by using the governing equations or via dimensional analysis (Kundu and Cohen, 2008). Included in the requirements of dynamic similarity is the additional similarity of non-dimensional initial and boundary conditions as these quantities define the solution given by the governing equations. If the input parameters are altered from the flow of interest, the solution will be different. Despite the conditions on matching non-dimensional parameters and on geometric similarity, as noted by Kundu and Cohen (2008), it is not always possible to attain full similarity in a model study. In such cases, corrections must be made to the experimental data to account for these differences. The degree and extent of the corrections is a source of uncertainty, and is generally dealt with by using a conservative approach. A complete consideration of the problem would include some reference experiments which maintain dynamic similarity that act as validation cases to which corrections and models can be compared. In this way a rigorous understanding of the relative importance

of certain geometric features and non-dimensional parameters may be used to make quantitative decisions about the effect on turbine performance.

When determining the relevant non-dimensional parameters using dimensional analysis, a critical step is choosing the dimensional parameters of interest for the system at hand. These can be classified into one of two groups: independent and dependent parameters, which obviously depend on the flow of interest. Independent parameters are set by the experimentalist, and typically include fluid properties and free-stream conditions. Measured quantities fall under the category of dependent parameters and include drag or lift force, power produced, etc. Independent parameters are used to reduce dependent ones into quantities which characterize the behavior of a model. These statements may seem obvious, but each parameter reveals the nuanced choices of the experimentalist. For instance, axial torque is a dependent quantity for a wind turbine while velocity is set by the experiment. The opposite is true of fan or blower-type experiments where the free-stream velocity is a function of the applied shaft torque. Another implication of dynamic similarity is the importance of various length-scale ratios in a problem. Just as similarity must be maintained for the initial conditions, if non-dimensional boundary conditions are not exactly the same between model and full-scale; additional length-scale ratios are present which creates new non-dimensional parameters (i.e., chord to radius or span to chord) that govern the resulting flow field.

The problem is somewhat more straightforward if the governing equations are known. The relevant independent and dependent parameters may be chosen to non-dimensionalize the equations in a direct manner. However, care must be taken that the correct equations are used in the analysis. Missing terms relevant to the full-scale will cause the model to behave in a different manner. An example of this is neglecting gravity effects in free-surface flows, as they play a large role in the resulting fluid dynamics. The following sections detail how the non-dimensional parameters relevant

to wind turbine aerodynamics are determined from the governing equations. Dependent and independent parameters are first chosen, which characterize the problem, followed by non-dimensionalization of the governing equations. Finally, the implications of the results, read through the lens of experimental and numerical scholarship on wind turbine aerodynamics, are discussed.

1.2.1 Governing Equations

The basic governing equations for wind turbine aerodynamics also fundamentally apply to propellers, fans, and other systems with rotation. The theoretical basis given here was based upon the so-called General Fan Scaling Laws (GFSL) developed by Sardar (2001). These were mainly modifications to the basic Navier-Stokes equations which allowed for consideration of the flow in a rotating frame of reference. The analysis here develops these ideas further by including the effects of compressibility. The conservation of mass is written in compressible form using Einstein notation as:

$$\frac{\partial \rho}{\partial t} + \frac{\partial \rho u_j}{\partial x_j} = 0 \tag{1.1}$$

where ρ is the fluid density and the velocity vector is given by $u_j = \langle u_1, u_2, u_3 \rangle$ and j is a dummy index. The Navier-Stokes equation governs fluid motion and is given in its most general form for a Newtonian fluid operating in the non-rotating frame as:

$$\rho \left[\frac{\partial u_i}{\partial t} + u_j \frac{\partial u_i}{\partial x_j} \right] = -\frac{\partial p}{\partial x_i} + \frac{\partial}{\partial x_j} \left[\mu \left(\frac{\partial u_i}{\partial x_j} + \frac{\partial u_j}{\partial x_i} \right) - \frac{2\mu}{3} \left(\frac{\partial u_m}{\partial x_m} \right) \delta_{ij} \right] \tag{1.2}$$

the fluid pressure is given by p, fluid viscosity is given by μ, $B_{f,i}$ represents the body forces, while j and m are dummy indices. To include the effects of rotation, the frame of reference must be changed via the following (as derived in Kundu and Cohen, 2008):

$$\left.\frac{du_i}{dt}\right|_{fixed} = \left.\frac{du_i}{dt}\right|_{rot.} + 2\epsilon_{ijk}\Omega_j u_k|_{rot.} - \Omega^2 R_i \tag{1.3}$$

where Ω_j is the angular velocity vector and R_i the vector component perpendicular to the axis of rotation. Substituting this into equation 1.2, new terms appear due to the rotation.

$$\begin{aligned}\rho\left[\frac{\partial u_i}{\partial t} + u_j\frac{\partial u_i}{\partial x_j}\right] = -\frac{\partial p}{\partial x_i} + \frac{\partial}{\partial x_j}\left[\mu\left(\frac{\partial u_i}{\partial x_j} + \frac{\partial u_j}{\partial x_i}\right) - \frac{2\mu}{3}\left(\frac{\partial u_m}{\partial x_m}\right)\delta_{ij}\right] \\ + \rho\left[\Omega^2 R_i - 2\epsilon_{ijk}\Omega_j u_k\right]\end{aligned} \tag{1.4}$$

The fourth governing equation is for energy, and is written for a compressible, real gas as:

$$\rho\frac{Dh}{Dt} = \frac{Dp}{Dt} + \frac{\partial}{\partial x_j}\left(k\frac{\partial T}{\partial x_j}\right) + \frac{\mu}{2}\left[\frac{\partial u_i}{\partial x_j} + \frac{\partial u_j}{\partial x_i}\right]^2 \tag{1.5}$$

where h is the enthalpy, T the temperature and k the heat conductivity (Smits, 2009). The fluid has also been assumed Newtonian and to obey the Fourier heat conduction equation. Further simplification can be achieved by assuming perfect gas behavior such that:

$$dh = C_{\mathrm{p}}dT \qquad\qquad R = C_{\mathrm{p}} - C_{\mathrm{v}} \tag{1.6}$$

where C_{p} and C_{v} are the specific heats at constant pressure and constant volume, respectively, while R is the gas constant. The relations of equation 1.6 greatly simplify the governing equations. The effect of deviations from perfect gas behavior due to real gas effects are discussed in section 1.2.3. It is then straightforward to get the final form of the energy equation in terms of the temperature:

$$\rho C_{\mathrm{p}} \frac{DT}{Dt} = \frac{Dp}{Dt} + \frac{\partial}{\partial x_j}\left(k\frac{\partial T}{\partial x_j}\right) + \frac{\mu}{2}\left[\frac{\partial u_i}{\partial x_j} + \frac{\partial u_j}{\partial x_i}\right]^2 \tag{1.7}$$

1.2.2 Scaling of the Governing Equations

In order to non-dimensionalize the governing equations, scaling parameters must be chosen for each variable in equations 1.1, 1.4, and 1.7. For the case of the horizontal axis wind turbine the relevant scales can be deduced from the sketch of figure 1.1. Here the turbine is rotating at a constant rate with fixed inflow velocity. The resulting scaling parameters are given by the equations of 1.8, 1.9, and 1.10. Although this example focuses on the HAWT geometry, the analysis for a vertical axis wind turbine or other rotating system is very similar with the scaling parameters adjusted accordingly.

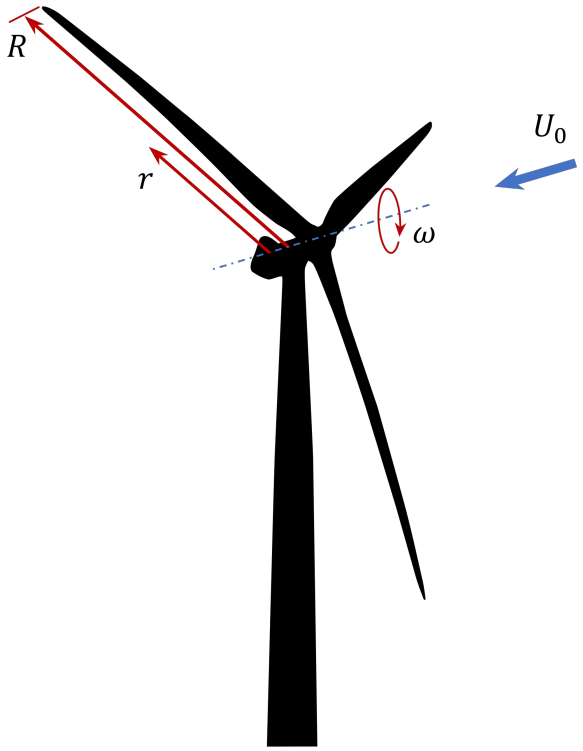

Figure 1.1: Horizontal axis wind turbine geometry showing relevant scaling parameters.

$$x_i^* = \frac{x_i}{L} \qquad R_i^* = \frac{R_i}{L} \qquad u_i^* = \frac{u_i}{U_0} \qquad t^* = \frac{tU_0}{L} \tag{1.8}$$

$$p^* = \frac{p}{\rho_0 U_0^2} \qquad T^* = \frac{T - T_0}{\Delta T} \qquad \Omega^* = \frac{\Omega_i}{\omega} \tag{1.9}$$

$$\mu^* = \frac{\mu}{\mu_0} \qquad \rho^* = \frac{\rho}{\rho_0} \qquad k^* = \frac{k}{k_0} \qquad C_{\mathrm{p}}^* = \frac{C_{\mathrm{p}}}{C_{\mathrm{p},0}} \tag{1.10}$$

The parameter L is a relevant length-scale such as the rotor radius, R, diameter, or chord length, ω the constant angular velocity of the turbine, and parameters with a subscript "0" denote free-stream quantities. The parameter $\Delta T = T_r - T_0$ is defined as the temperature difference between a reference value and the free-stream. Using these parameters, the governing equations of motion can be re-scaled in the following ways.

$$\frac{\partial \rho^*}{\partial t^*} + \frac{\partial \rho^* u_j^*}{\partial x_j^*} = 0 \tag{1.11}$$

The non-dimensional form of the continuity equation indicates that for the scaling parameters chosen, both terms are of the same order. The Navier-Stokes equation takes the form:

$$\begin{aligned} \frac{Du_i^*}{D_t^*} = &-\frac{\partial p^*}{\partial x_i^*} + \frac{1}{[Re]} \frac{\partial}{\partial x_j^*} \left\{ \mu^* \left(\frac{\partial u_i^*}{\partial x_j^*} + \frac{\partial u_j^*}{\partial x_i^*} - \frac{2}{3} \frac{\partial u_m^*}{\partial x_m^*} \delta_{ij} \right) \right\} \\ &+ \left([Str]^2 \Omega^{*2} R_i^* - 2[Str] \epsilon_{ijk} \Omega_j^* u_k^* \right) \end{aligned} \tag{1.12}$$

The bracketed terms of equation 1.12 give the non-dimensional coefficients which control the relative order of magnitude of each term:

$$\text{Reynolds number} \qquad [Re] = \frac{\rho_0 U_0 L}{\mu_0} \tag{1.13}$$

$$\text{Strouhal number} \qquad [Str] = \frac{\omega L}{U_0} \tag{1.14}$$

where the easily recognized Reynolds number is present. With the current scaling variables, the exact form of Re has not been specified. In fact a multitude of Reynolds numbers may be prescribed for a wind turbine using any number of length-scales for L. If the conditions of exact geometric similarity are followed between a model and the full-scale, it will not matter which length-scale ratio is chosen to define Re. Any newly defined Reynolds number for a model of exact scaled geometry will simply be a product of any other Reynolds number, with the factor between them being the ratio of length-scales. This is the reason for geometric similarity between model and full-scale. Without this condition, new length-scale ratios will create additional non-dimensional parameters and thus the two flows will not be dynamically similar. The literature contains many variations of the Reynolds number defined at various locations on the rotor (Vermeer et al., 2003). The effort is motivated by identifying the most "dynamically relevant" location on the rotor whose Reynolds number has something of a first-order effect on the observed operational state of the turbine. The problem with interpreting these values across experiments is that comparison becomes very difficult if not impossible when length-scale ratios have been altered to achieve a particular Reynolds number. In reality, there may be a length scale which properly characterizes Reynolds number effects, but this has not been extensively studied and the variety of wind turbine designs indicate this is a very large parameter space. The most effective means of comparison would be to include detailed geometrical descriptions of the model under test with clear and reproducible definitions of the Reynolds number (i.e., based on measurable quantities in the flow).

The Strouhal number is also present and characterizes the rotational effects. In wind turbine literature this is often denoted as the tip speed ratio, λ, when using the radius as the length-scale. This parameter is similar to the advance ratio for propellers or the volume flow coefficient for pumps and fans. The commonality being the frequency dependency, with each variation based on the relevant scaling parameters of the specific flow under consideration. The non-dimensional energy equation takes the form:

$$\rho^* C_p^* \frac{DT^*}{Dt^*} = [Ec]\frac{Dp^*}{Dt^*} + \frac{1}{[Re][Pr]}\frac{\partial}{\partial x_j^*}\left(k^*\frac{\partial T^*}{\partial x_j^*}\right) + \frac{[Ec]}{[Re]}\left(\frac{\partial u_i^*}{\partial x_j^*} + \frac{\partial u_j^*}{\partial x_i^*}\right) \tag{1.15}$$

where again the bracketed terms denote the non-dimensional parameters:

$$\text{Prandtl number} \qquad [Pr] = \frac{\mu_0 C_{\mathrm{p},0}}{k_0} \tag{1.16}$$

$$\text{Eckert number} \qquad [Ec] = \frac{U_0^2}{C_{\mathrm{p},0}(T_w - T_0)} \tag{1.17}$$

The Prandtl number is a combination of the physical properties of the flow and is the ratio of momentum to thermal diffusivity, combined with the Reynolds number it forms the Péclet number which represents the ratio of heat transfer via convection to heat transfer from conduction. The Eckert number is also present and characterizes heat dissipation in the flow. The value of this parameter is typically small in most of the wind turbine operating environment due to the large value of $C_\mathrm{p} \approx 1000$ (J/kg K) in air. Velocities near the tip may however produce much larger Ec values since $U_0 \approx 100$ (m/s) are possible, indicating the Eckert number remains relevant to the flow physics. This parameter can be re-written as:

$$[Ec] = [Ma]^2 \frac{a^2}{C_{\mathrm{p},0}\Delta T} \tag{1.18}$$

where a is the sound speed. This equation shows the effect of Mach number is hidden inside the Eckert number, use of the isentropic relationships for a perfect gas ($a^2 = \gamma R_u T$) and equations 1.6, further simplification is possible:

$$[Ec] = (\gamma - 1)[Ma]^2 \frac{T_0}{\Delta T} \tag{1.19}$$

Thus the Mach number remains an important parameter for wind turbine studies and must be considered when matching the dynamics of the full scale. When all of these non-dimensional parameters are matched between the flow of interest and the model under test, along with boundary and initial conditions, the two flows are said to be dynamically similar.

1.2.3 Implications of Dynamic Similarity

To properly match the model to full-scale, the parameters listed in section 1.2.2 must be matched exactly along with boundary and initial conditions. Boundaries are typically characterized by ratios of length-scales such as radius to chord length, hub diameter to radius, and nacelle to rotor frontal area are all possible choices. Practically speaking, small deviations from strict length-scale similarity may be permitted if proper justification is provided. It follows logically that the rotor, as the primary aerodynamic surface of interest and that which has the largest effect on the wake structure, should aim to most closely match the full-scale. Other length-scale ratios may also be important during model testing, such as the blockage ratio:

$$B_R = \frac{A_{\mathrm{rotor}}}{A_{\mathrm{tunnel}}} \tag{1.20}$$

where A_{rotor} is the frontal, swept area of the turbine rotor and A_{tunnel} is the cross-sectional area of the tunnel. In the field, $B_R \to 0$ (with the ground having a blockage-like effect at some point) while HAWT experiments have been performed at a range of blockage ratios, from $B_R = 100\%$ to fractions of a percent (Mikkelsen, 2004; Vermeer et al., 2003). This illustrates the difficulty of achieving true full-dynamic similarity with the flow of interest in the laboratory or in simulations. Other length-scales of importance are tower diameter and nacelle dimensions. In practical terms, full dynamic similarity may be impossible to achieve or if achieved may not be a flow of engineering interest (i.e., the problem has been oversimplified to allow for model testing). It is therefore useful to apply corrections where possible to account for these practical deficiencies.

Other simplifications were made when developing the non-dimensional forms of the governing equations. One of these is the assumption of a perfect-gas relationship, to which no real gas truly holds but which many working fluids approximate to an acceptable degree. Without these simplifications, in particular to the energy equation, proper scaling could not have taken place to directly show the dependency on $[Ec]$ and $[Ma]$. The equations themselves can be used to judge the error in these assumptions, or appropriate real-gas relations can be used to evaluate it:

$$p = \rho Z R T \tag{1.21}$$

the parameter Z represents a compressibility factor which is commonly used to express deviations from ideal-gas behavior. This factor varies by only a small amount for pressurized, dry air over a wide range of fluid pressure and temperature ranges. For instance, Z changes by only approximately 10% in the range of 1 to 240 (bar) (at fixed $T = 23°\text{C}$).

Other terms in the governing equations have been specifically left out of the current discussion as they are not of primary importance to the flow dynamics of wind

turbines. For instance, the Froude number $[Fr] = U_0/\sqrt{g_0 L}$ is typically included in the case of free-surface interactions or when density gradients are present in the fluid. For most field-scale turbines this is not the case. Although slight density gradients do exist in the atmosphere due to hydrostatic pressure, these are easily taken into account by re-defining the pressure term such that $\tilde{p} = p + \rho_0 g_0 x_3$ (Sardar, 2001). In this way, when the body force is included in the governing equations, there are no additional non-dimensional parameters which need to be matched. For hydrokinetic or floating turbines, Froude number effects may need to be included but are not discussed in this thesis.

The choice of velocity scale, U_0, must also be considered carefully in the context of wind turbines. Although any choice of velocity to define U_0 is valid, some choices may better capture the scaling of turbine performance or flow dynamics than another. When considering the Reynolds number, a more appropriate scaling parameter may be the aforementioned chord-based value which typically uses some estimate of the local blade velocity. For horizontal axis wind turbines, the relevant velocity scale is often chosen as the magnitude of the free-stream and angular velocity times the radial distance of the section, r:

$$U_{rel} = \sqrt{U^2 + (\omega r)^2} \tag{1.22}$$

For the Mach number, a different velocity scale than the free-stream is appropriate, such as the tangential velocity at the tip, ωR. The ratio of this velocity to the free-stream is given by the tip speed ratio, which is the most common version of the Strouhal number used in the wind energy field:

$$[\lambda] = \frac{\omega R}{U} \tag{1.23}$$

and for HAWT operation is typically from 2 to 10, indicating that the tip velocity is much larger than the free-stream and most likely to be affected by compressibility effects. For VAWT operation, λ is typically lower with values from 1 to 5. As can be seen, the effects of rotating flow have far reaching implications when matching the non-dimensional parameters.

1.3 Reynolds Number Behavior of Wind Turbines

As noted by Schlichting (2000), determining the functional dependence of a parameter on Reynolds number is in many cases theoretically impossible. This is due to the highly-nonlinear and coupled behavior of the equations of motion as discussed in section 1.2.2, with the added complications of having three-dimensional boundary conditions. Therefore experiments and numerical simulations of the governing equations are needed to gain understanding of how important parameters scale with Reynolds number. Still, even these methods have challenges due to the large range of length-scales present; for both simulations and experiments cost becomes an increasingly important factor to consider and some concessions must be made. From a practical point of view, full dynamic similarity may not always be necessary to capture the relevant flow physics of engineering interest. If deviations must be made from the governing non-dimensional parameters, boundary, and/or initial conditions, the question is then which parameters are of primary importance and how large can these deviations be while still retaining the nature of the flow? Given the discussion of section 1.2.2, the parameters most relevant to the study of all wind turbine geometries are the following:

$$Re = \frac{\rho U L}{\mu}; \qquad \lambda = \frac{\omega R}{U}; \qquad Ma = \frac{\omega R}{a} \tag{1.24}$$

where U, μ, a, and ρ are all taken as free-stream values, L a relevant length-scale, R the rotor radius, and ω the fixed rotor angular velocity. Without any consideration of the rotor geometry in question, the inverse relationship with velocity present in Re and λ makes simultaneous matching of both parameters challenging in model testing. Consequently, both horizontal and vertical axis wind turbine experiments are often performed at reduced Reynolds numbers or tip speed ratios (Vermeer et al., 2003). The scale-disparity between laboratory and field is revealed when comparing some commonly-used Reynolds number values to those typically found in experiments. For field-scale turbines, operating with standardized inflow conditions of $\rho = 1.225$ (kg/m^3), $\mu = 18.3 \times 10^{-6}$ (Pa·s), and $U = 10$ (m/s), some representative Reynolds numbers based on diameter can be calculated. For small HAWT turbines of $D = 20$ (m), $Re_D = 13.4 \times 10^6$, while more modern machines are approaching $D = 200$ (m) so that $Re_D = 134 \times 10^6$. Both units typically operate over a range of $\lambda \in [2, 10]$. While not as widely available as commercial HAWTs, VAWTs still achieve large Reynolds numbers in the field due to their relatively large scale. On the smaller side, diameters of $D = 2.17$ (m) have been commercially produced (Miller et al., 2018), and have an associated $Re_D = 1.5 \times 10^6$. While on the larger end, $D = 19$ (m) turbines were sold for many years (FloWind, 1996), giving similar Re_D values to the smaller HAWT units, near 13×10^6. As discussed later, VAWT units operate at lower tip speed ratios than HAWTs, typically in the range of $\lambda \in [1, 6]$. For both HAWT and VAWT geometries operating in the field, Re_D values are therefore very large, leading to the hypothesis that Reynolds number invariance is assured during operation. However, it is currently unknown what value of Reynolds number is

sufficient for invariance or even if Re_D is the correct parameter to quantify invariant behavior. To date no extensive study has been made which spans a large enough Reynolds number range to fully investigate these claims. This is primarily due to the difficulty of achieving dynamic similarity in an experiment as discussed in the following.

The challenge of model scaling can be demonstrated using the parameters of equation 1.24. Re-writing in terms of the length-scale reduction, $\chi = R_{\text{full-scale}}/R_{\text{model}}$, where the model radius has been chosen as the defining length-scale for Re. Dynamic similarity stipulates that:

$$\frac{Re_{\text{model}}}{Re_{\text{full-scale}}} = 1 = \frac{1}{\chi}\frac{U_{\text{model}}}{U_{\text{full-scale}}}\frac{\nu_{\text{full-scale}}}{\nu_{\text{model}}}$$

where $\nu = \mu/\rho$ is the kinematic viscosity. For atmospheric wind tunnels the ratio $\nu_{\text{full-scale}}/\nu_{\text{model}}$ is fixed at unity so the only parameter available for matching Re is the velocity ratio such that $U_{\text{model}}/U_{\text{full-scale}} = \chi$. However if this is the case then matching the tip-speed ratio implies that:

$$\frac{\omega_{\text{model}}}{\omega_{\text{full-scale}}} = \chi\frac{U_{\text{full-scale}}}{U_{\text{model}}} = \chi^2$$

therefore the rotation rate must be the length-scale ratio squared. For even a modest reduction of $\chi = 10$, the model would need to spin at $\omega_{\text{model}} \approx 953$ (rad/s) or $9,100$ (r.p.m.) creating significant mechanical challenges for balancing and control. Perhaps more problematic is when the Mach number effects are considered:

$$\frac{Ma_{\text{model}}}{Ma_{\text{full-scale}}} = \chi$$

due to the sound speed remaining constant between model and full-scale. This simple example means that unless χ is kept very low, testing HAWT or VAWT models in conventional, atmospheric wind tunnels cannot achieve dynamic similarity for even

small field turbines. As discussed in section 1.4.4, the typically experimental approach is to vary the Re_D over whatever range is allowed by the facility to try and evaluate if invariance is achieved. This method has two primary issues both stemming from the small range of Re_D values typically considered. The first is that a noticeable Reynolds number dependency may not be evident over the small range tested and Re_D values are typically one to two orders of magnitude below the full-scale. It thus remains an open question as to how the flow dynamics of both HAWTs and VAWTs change with Reynolds number when considering the range tested in typical wind tunnels up to the full-scale Re_D values. The following sections review the relevant literature on the topic of Reynolds number scaling for horizontal and then vertical axis wind turbines.

1.4 Horizontal Axis Wind Turbines

The reality of field-scale wind turbine operation is that a multitude of conditions are possible; all of which may in some way depend on the Reynolds number. The power-producing regime is typically of high interest and in the ideal case is made up of airfoil sections operating in the attached-flow regime. In contrast, other modes of operation such as startup (very low tip speeds), mis-aligned inflow (yawed flow case), or parked (stationary) rotor state, may involve highly separated flow on parts of the rotor and non-steady operation. It is highly likely that commonalities exist between all operating states, and although many off-design operational modes are interesting from a fluid-mechanics point of view, practically speaking the power-producing state is of prime concern. This is the region in which a power producing (and hence profitable) wind turbine is designed to spend the majority of its lifetime. There is also a wealth of knowledge available from decades of research in the field. This thesis is therefore motivated to address the operational space of attached flow at what would be considered standard operating conditions, i.e. near the peak in turbine performance.

The following provides a brief review of the dominant sources of Reynolds number effects when a HAWT is in this regime. First, the blade element is introduced as a link between two-dimensional aerodynamics and wind turbine operation. Then the Reynolds number characteristics of sectional airfoil performance are discussed. This is followed by a brief review of rotational effects and the current state of understanding regarding the driving flow phenomena. Finally some general comments are made regarding the coexistence of these two effects and how their shared dependence on Reynolds number may be influencing some of the behavior commonly seen in HAWT operation.

1.4.1 Blade Element Formulation

Unlike experiments with two-dimensional airfoil sections, on which the Reynolds number influence may be straightforward to characterize, horizontal axis wind turbines involve a more complex mechanism by which changes in airfoil performance ultimately affect global parameters such as measured thrust and power coefficient of the entire rotor. Thus many experiments have attempted to measure sectional performance along a rotor blade so that distinctions may be drawn between nominally two-dimensional airfoil operation, and the three-dimensional conditions on the rotor. Typically measurements are made at specific radial locations via blade-level techniques such as pressure taps or hot film anemometers (Simms et al., 2001). Models of this type are quite complex and very few experiments have been conducted at high enough Reynolds numbers to be representative of full-scale values (Schepers and Snel, 2007; Simms et al., 2001). The other option involves numerical simulations using computational fluid dynamics (or CFD, Sanderse et al., 2011). These give some insight, but are often limited by the enormous range of length-scales present. This forces many studies to use low grid resolution and then to rely on two-dimensional airfoil information as input. The question is then how accurate are these methods at capturing the flow

physics unique to the rotating, three-dimensional system? An even simpler method of determining rotor performance, known as Blade Element Momentum theory or BEM, also cannot directly simulate three-dimensional Reynolds number effects, but again relies on two-dimensional input data and various corrections (Hansen, 2007). The fundamental assumption of BEM involves quasi-one-dimensional momentum balance to solve for the outer flow interaction with the rotor coupled to a blade element which determines the sectional performance of the rotor. An iterative method is used to converge on a solution for both the blade element and momentum equations. Typically the sectional airfoil characteristics are modified before being used as input to the BEM solver along with other corrections which account for effects due to the 3-D nature of the flow on the entire rotor (Hansen, 2007; Jamieson, 2018).

Despite the simplicity of BEM, the theoretical basis behind the method can lend some physical insight into possible Reynolds number dependent behavior of the rotor. The observed operation may in part be explained by examining the BEM equations themselves, an approach which cannot typically be pursued with other numerical solution methods. Care must be taken when using this approach, as BEM inherently assumes that radial sections of the rotor act independently. Therefore many of the complicating effects of unsteadiness, three-dimensionality, separation, Reynolds number dependency, dynamic stall, and rotational influences must be modeled. For this reason, detailed experiments and simulations of HAWT aerodynamics are crucial to further understanding of the various flow phenomena. The problem is simplified for experimental or numerical work if the flow is laminar and the turbine axis of rotation is aligned with the incoming flow. In this condition many of the more complicated operating modes, such as dynamic stall, do not play an important part in the flow physics (Schreck and Robinson, 2002, this is not necessarily the case for the VAWT as discussed in section 1.5.1). This allows for focus to be placed on Reynolds number and rotational effects. Thus a turbine rotor operating in this manner can be considered

the canonical case for the horizontal axis wind turbine, and is a simplified case compared with field operation. Further modifications can be made to allow for unsteady effects such as turbulent inflow, but these are outside the scope of this thesis which is focused on the canonical method of HAWT operation. In order to understand how changes in the sectional airfoil performance affect the rotor operation when in this state, the following gives an overview of the blade element concept. This is then naturally followed by a review of the literature concerning Reynolds number dependence of two-dimensional airfoil aerodynamics.

Considering the blade-element formulation of the sectional power coefficient, the power and thrust produced by a section of the rotor may be given as a function of the relative velocity at the airfoil, U_{rel}, the sectional airfoil lift and drag coefficients, C_l and C_d, the number of rotor blades, N_b, and the flow angle from the rotor plane, ϕ (Hansen, 2007; Jamieson, 2018). Here the flow angle is the geometric sum of the angle of attack, α, the blade twist at the section β, and the collective blade pitch, θ_p (defined as positive into the flow), such that $\phi = \alpha + \beta + \theta_p$. During steady-state operation with a fixed geometry, β and θ_p remain fixed. The loads at the blade section are then defined by the geometry of figure 1.2.

The sectional loads can be solved geometrically by considering a series of blade elements located at different radial stations from the hub. Additional equations are needed to solve for the rotor performance, this is accomplished with a momentum-based theory to solve for U_{rel} and ϕ. As a simplification, the relative velocity can be approximated by $U_{rel} \approx \sqrt{U_0^2 + (\omega r)^2} = U_0\sqrt{1 + \lambda^2}$ for a rotor in the power producing regime at moderate-to-high tip speed ratios. For the discussion in this thesis, only the blade-element needs to be considered. Not discussed is the feedback like mechanism which alters the flow momentum through the rotor and which in some way depends on the sectional airfoil properties. The following is mainly concerned with small deviations from the canonical rotor operational state, and thus

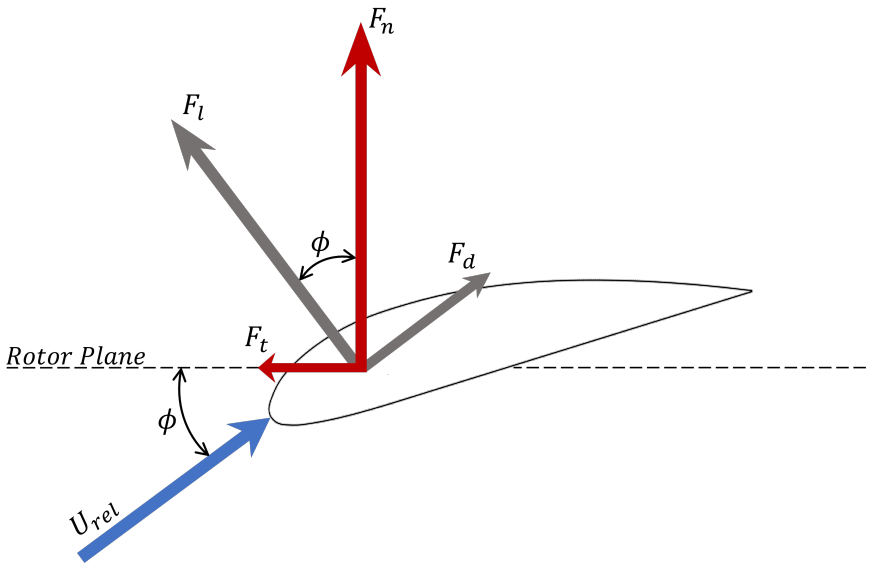

Figure 1.2: Geometry of the HAWT blade element at a section located distance r from the rotor hub.

development of the momentum equations is not undertaken. This is discussed in more detail in the following. The lift and drag at each blade element can be solved geometrically and give the sectional loading for an element of width dr as:

$$dF_l = C_l \frac{1}{2} \rho U_{rel}^2 c dr \tag{1.25}$$

$$dF_d = C_d \frac{1}{2} \rho U_{rel}^2 c dr \tag{1.26}$$

where c is the local chord length, and C_l and C_d the sectional airfoil polars. In a typical simulation the values of these last two parameters are chosen from a look-up table for the given airfoil section. The rotor power is due to the force component in the tangential direction. Using the geometry of figure 1.2, this force can be solved in terms of the lift and drag coefficients and local flow conditions:

$$dF_t = \frac{1}{2}\rho U_{rel}^2 c \left[C_l \sin(\phi) - C_d \cos(\phi)\right] dr \tag{1.27}$$

The sectional power is then found by multiplying this value by each section's tangential force and its radial location times the angular velocity, $\omega r dF_t$.

$$dP = \frac{1}{2}\rho N_b c U_{rel}^2 \left[C_l \sin(\phi) - C_d \cos(\phi)\right] \omega r dr \tag{1.28}$$

Since the focus of this discussion is the nominal case of maximum power-production, the tip speeds must be moderate to high, i.e., $\lambda \approx 6$ or larger, with the flow remaining mostly attached over the rotor surface (Jamieson, 2018). The airfoil sections located farther from the hub have a clear advantage in producing power as the relative velocity is larger (using the approximation above) and the moment-arm, r, is larger. Furthermore, ϕ must be a moderate value below approximately twenty degrees or so (depending on the particular airfoil) to ensure the flow is attached and a useful lift force is being generated. Even if the value of C_d is relatively small, it can have a large effect on the power production due to the $\cos(\phi)$ term. As noted by Jamieson (2018), it is plausible from equation 1.28 that maximizing the lift to drag ratio will increase the power produced by each blade element. However, no restrictions have been placed on either the relative velocity nor ϕ to remain constant, both of which may also change as C_l/C_d is altered. The sectional contribution to the thrust force is solved in a similar way to find:

$$dF_n = \frac{1}{2}\rho N_b c U_{rel}^2 c \left[C_l \cos(\phi) + C_d \sin(\phi)\right] dr \tag{1.29}$$

This result indicates the axial thrust force would be much less sensitive to changes in the drag coefficient, again provided that the changes in U_{rel} and ϕ are relatively small. Finally it is noted that the main portion of the lift vector is contributing to the thrust force, in fact changes in the drag may not be observed when looking at measurements of the rotor thrust. Therefore, it could be expected that the power coefficient would be a much more sensitive metric to changes in drag, while the thrust coefficient makes it difficult to distinguish between lift and drag increases.

The basic blade element equations have led to relations between sectional performance and the mechanical loads produced by a rotor. Changes in C_l and C_d will cause the performance of the rotor to be altered, and estimates of these changes have been discussed with the assumption that the relative velocity and flow angle change only incrementally. This may not, in fact, be the case due to the large parameter space of varying rotor geometry, inflow, and operating conditions possible. With these caveats in mind, the following section discusses how lift and drag coefficients have been observed to behave with changes in the Reynolds number. The goal of this review is to gain some additional insight into the Reynolds number behavior which might be observed on a HAWT rotor, in light of the blade-element equations just discussed.

1.4.2 Reynolds Number Effects on 2-D Airfoil Performance

The effect of altering the Reynolds number has been studied in much more detail for sectional airfoil performance than for HAWT rotors. The two fields are closely related, and much of the available airfoil data has been put to use over the years in HAWT design. The early experimental work of Jacobs and Sherman (1937) was one of the first in-depth analyses of Reynolds number dependence for sectional airfoil characteristics with a parameter space from $Re_c = 40,000$ to 3.1×10^6 with later publications by co-workers pushing this envelope out to 25×10^6 (Loftin and Bursnall, 1948). Here the chord Reynolds number, Re_c, is distinct from that defined for a wind

turbine because the flow is nominally two-dimensional. The definition is made using the section chord and free-stream properties which are also used to normalize the lift and drag forces. Direct comparisons between Re_c of two-dimensional airfoils and three-dimensional rotor operation are not possible, but are typically described in the assumed framework of the blade element as discussed in section 1.4.1, where each radial section operates independently (i.e., as a two-dimensional strip). Major conclusions regarding Reynolds number trends were common among the early airfoil studies, and fall into three major categories:

(i) The lift curve slope in the linear region shows no dependence on Re_c above a cutoff Reynolds number (typically given as $Re_c \geq 800,000$).

(ii) The maximum lift and subsequent stall point increase steadily with Re_c for the range of Reynolds numbers tested.

(iii) The minimum drag initially decreases and then increases as the turbulent transition point moves towards the leading edge.

These points are illustrated in figures 1.3 (a) and (b) which are simulation results for a N.A.C.A. 63-218 airfoil section using the Xfoil tool (Drela, 1989). Item (i) is somewhat expected, with the cutoff Reynolds number for this behavior being of the same order of magnitude as what other works have found to characterize low-Reynolds number behavior (Miley, 1982; Mueller, 1985). Experiments and simulations performed below this threshold will most likely not adhere to the Reynolds number trends discussed in this section. The implied complications for HAWT experiments is discussed in greater detail in section 1.4.4.

When considering airfoils in the design stage, points (ii) and (iii) must be corrected for when using standard design airfoils where Re is fixed (Jacobs and Sherman, 1937). The maximum lift increase begins to occur at moderate Reynolds numbers, when the boundary layer becomes turbulent closer to the leading edge of the airfoil. This has

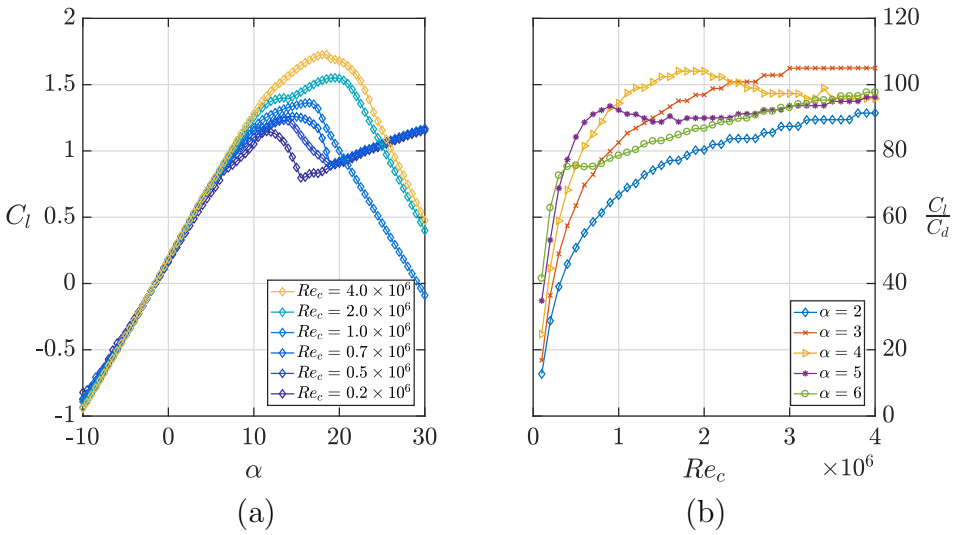

Figure 1.3: Numerically simulated lift and drag properties for a N.A.C.A. 63-214 airfoil. Plot (a) shows the lift as a function of angle of attack and blade Reynolds number to illustrate points (i) and (ii). The data of plot (b) shows the lift-to-drag ratio as a function of blade Re for several moderate α value to highlight the effects of point (iii).

the effect of increased resistance to separation due to the tendency of a turbulent boundary layer to mix in outer flow momentum near the surface and delay stall.

Point (iii) is the most subtle of the effects and implies that section drag can be lower at moderate as opposed to high Reynolds numbers, for a moderate angle of attack (typically α would range from two to seven, normally considered to be in the linear region). This effect is demonstrated in the simulation results of figure 1.3 (b) for which transition was not forced. The magnitude of this effect is very dependent on the specific airfoil geometry, angle of attack chosen, and inflow conditions, but also the airfoil thickness as discussed by Loftin and Bursnall (1948). In that work, thicker airfoils were seen to extend this effect out to higher Reynolds numbers due to their larger, negative pressure gradient on the suction side of the airfoil. If this trend continues at increased thicknesses, it is plausible that the operation of a wind turbine could be affected at what is considered relatively large values of the Reynolds number (i.e. well beyond the threshold for low Re behavior, as discussed above). Many of the airfoils studied in these works were primarily designed for aircraft use, with relatively

thin sections from 6% to 18%. Recent work has aimed to remedy this by focusing on wind turbine specific airfoils at high Reynolds numbers (Llorente et al., 2014; Pires et al., 2016; Somers and Tangler, 2000). This also indicates that nearly eight decades later, a more complete understanding of scale effects for sectional airfoil performance is still being sought. The most recent of these works by Pires et al. (2016) focused on a single, wind turbine specific airfoil geometry over a range of Re_c from 3×10^6 to 15×10^6 with both transition-free (smooth) and forced transition (trip devices) airfoils. For the smooth condition, the general trends with increasing Reynolds number aligned well with the previous work. While tripped airfoils followed trends (i) and (ii) but lost the effect of reduced drag in point (iii), suggesting that forcing transition and roughness effects disrupt this mechanism. With regard to the full-scale wind turbine, point (ii) implies that operating in stalled conditions will see some performance change with Reynolds number. Although for a turbine in normal operation, most of the outer rotor operates outside of stall, and it would be expected that turbine performance may not heavily depend on Reynolds number due to point (i). The first exception to this is the inboard airfoil sections on a rotor, which are much more likely to operate in stall because the relative velocity is composed of competing parts rotational and inflow components. Finally, a second caveat comes when considering point (iii) as it applies to the smooth-rotor case, which could still display a sensitivity to Re effects if α is relatively small.

1.4.3 Rotational Augmentation

The influence of rotation on airfoil performance has been studied extensively, and is typically characterized by a higher than predicted lift produced by the inboard sections of the rotor when they operate in or near stall. Although it is generally agreed that loads increase, the causes of this phenomenon are still debated (Guntur, 2013). Among the proposed rotationally-driven mechanisms for this load increase

are: a delay in stall by changing of the separation point, altering of the pressure distribution of an airfoil section by inducing radial flow in the separated portion of the blade, a combination of these two effects, and possibly a mechanism which changes the turbulent transition point. A more complete review of these mechanisms can be found in Hansen and Butterfield (1993), and Guntur (2013). The practical result is that BEM codes directly implementing sectional airfoil data tend to under-predict the rotor performance, particularly for stall-controlled wind turbine designs. Many authors have covered the topic of corrections for rotational augmentation, see for example Bak et al. (2006); Banks and Gadd (1963); Chaviaropoulos and Hansen (2000); Du and Selig (2000); Dumitrescu et al. (2007); Lindenburg (2004); Snel et al. (1994); Viterna and Janetzke (1982), yet significant uncertainty remains regarding the proper method of accounting for these effects. Work involving field tests concluded that rotation had little effect on 2-D airfoil performance, but did generate span-wise pressure gradients due to the radial flow which increased loads (Madsen and Christensen, 1990). That is to say a significant deviation from 2-D behavior was seen under the influence of rotation. However measurements of the lift and drag curves during rotation were only given at the rotor mid-span. Root section results, where rotation effects had been shown to dominate, are not reported. Another experiment which attempted to characterize these effects at high Reynolds number was the large-scale, National Renewable Energy Lab (NREL) Unsteady Aerodynamics Experiment (UAE), which gathered field as well as wind tunnel data (Robinson et al., 1999; Schreck and Robinson, 2004). The field tests showed a significant increase in the blade loads under rotation, pointing to rotational augmentation as the cause. Wind tunnel measurements found that rotational augmentation may occur independently of changes in the Reynolds number. In this case, the performance augmentation may be fully characterized by the non-dimensional rotation rate, λ, and chord length to radial location ratio, c/r, as some authors have suggested (Guntur, 2013). A

similar set of experiments known as the Model EXperiments in COntrolled conditions (MEXICO) also used a large model rotor tested in a very large wind tunnel. A paper is available which compares rotational augmentation effects of both the MEXICO and UAE experiments (Schreck et al., 2010). Axial forces are seen to increase in a similar way due to rotation, although some differences are noted in post-stall which is attributed to the difference in airfoils on each rotor. With the exception of these two works, relatively little rotor performance measurements over a broad range of Reynolds numbers is available to draw conclusions, indicating an additional need for these types of measurements.

1.4.4 HAWT Rotor Effects with Reynolds Number

Few laboratory experiments exist where the Reynolds number is high enough to be considered a field-scale value. For a typical wind tunnel, the length-scale ratio of the model must be reduced so as to physically fit inside the test-section and minimize flow blockage. An overview of previous HAWT experiments performed in the laboratory, along with a listing of the Reynolds numbers (when available), can be found in the review paper of Vermeer et al. (2003). Only two have achieved relatively large Reynolds numbers approaching full-scale, where the listed $Re_c \geq 500,000$ (Robinson et al., 1999; Schepers and Snel, 2007). As noted in section 1.4.2, airfoils exhibit markedly different behavior below a threshold near this value. Therefore, many low-Re experiments may display different Reynolds number dependencies than are present at high Re or in the field. The focus is then on the two high Reynolds number experiments, which were accomplished by using large models in very large facilities. The NREL UAE tests used a $D = 10$ (m) model (Robinson et al., 1999) while the MEXICO tests utilized a model of $D = 4.5$ (m) (Schepers and Snel, 2007). An estimate has been made of the operational Reynolds numbers of these two experi-

ments at two different inflow velocities and at standard atmospheric conditions[2] with the results given in table 1.4.4. Note that at the largest tested Re_D of the NREL data is only approaching the smaller field values found in section 1.3. Meanwhile the chord Reynolds number, Re_c, has been estimated using an approximation of the relative velocity at the tip, U_{rel} as discussed in section 1.4.1. Even at the higher free-stream velocity, the chord Reynolds number just approaches 10^6. As discussed in section 1.4.3, the NREL data showed clear signs of rotational augmentation when the rotor operated in or near regions of stall. However this behavior was found to not depend on the blade Reynolds number, but purely on rotational effects by comparison with data taken on the static rotor. This is a somewhat surprising result considering the discussion of airfoil section performance with Re of section 1.4.2. Ideally, the NREL tests would have also varied only the turbine Reynolds number and kept the rotational effects constant by maintaining a fixed λ value to test this conclusion. Another work which looked at Reynolds number effects on the rotor was a comparison made between the MEXICO results and those of a scaled-down model rotor of the same geometry, but with $D = 2$ (m) (Schepers et al., 2011). A scale effect was found which caused the smaller model to report lower values of the power coefficient. This was attributed to Reynolds-dependent changes in the sectional airfoil characteristics, in particular a drag increase at lower Re for the specific airfoils of those rotors. This is a plausible explanation given the discussion of section 1.4.1 and 1.4.2. From these works, it might be expected that Reynolds number has an effect on performance, but that it is limited to those due to sectional airfoil changes and not rotational effects.

The value of the threshold Reynolds number is therefore a source of great concern for experiments and numerical simulations. Earlier works have tried to quantify this value, with the review paper of de Vries (1983) citing a chord-Reynolds number of at least 300,000 to avoid Reynolds number effects. However, no convincing justification

[2]In this case constant-speed operation was assumed while $\mu = 18.29 \times 10^{-6}$ (Pa·s) and $\rho = 1.225$ (kg/m^3).

Table 1.1: Representative Reynolds number values for prior large-scale, laboratory experiments.

Experiment	$U = 10$ (m/s)		$U = 25$ (m/s)	
	Re_D	Re_c	Re_D	Re_c
NREL UAE Phase VI	6.8×10^6	$930,000$	17×10^6	1.1×10^6
MEXICO	3.0×10^6	$770,000$	7.5×10^6	$800,000$

is given for this value. The work of Chamorro et al. (2011) suggests a value of the Reynolds number based on rotor diameter and free-stream conditions of $Re_D \geq 93,000$ as the minimum for independence. Measurements were made in the far wake of a small model turbine and the first and second velocity moments showed less of a dependence on Re. However the highest Re_D tested in that study was $173,000$, which is at least an order of magnitude short of what could be considered a field-scale value. To date no set of experiments have covered a wide enough range from model to full-scale Reynolds numbers (however it is defined) for which definitive conclusions can be drawn about the scaling behavior.

It is plausible that Reynolds number has less of an effect on certain quantities than others. Previous sections discussed how C_p could be particularly susceptible to sectional airfoil characteristics, but other mean quantities in the flow may react in a different manner. For example, in high-Reynolds number submarine studies, it was found that the mean velocity profile in the wake collapsed at the lowest Reynolds numbers tested ($Re_D = 280,000$ based on free-stream conditions and the diameter of the model, Jiménez et al., 2010). In contrast, the turbulent fluctuations continued to evolve even at the highest Re_D tested of 17×10^6. The same may be true of wind turbine wakes, especially when considering the discussion of sections 1.4.1 and 1.4.2. For rotors operating in the power-producing range with the majority of the turbine rotor outside of stall, C_l over the rotor would be expected to remain relatively constant with changes in the Reynolds number. Therefore the axial thrust force could

remain constant, which has the largest effect on the axial momentum change over the rotor. The question of Reynolds number dependence therefore likely depends on what quantities are of interest. If it is only desired to match mean thrust coefficient and mean wake velocity, perhaps lower Re are acceptable. If complete similarity is sought, a much higher value of Re could be necessary before the equations of motion are sufficiently insensitive to additional increases in the Reynolds number.

1.5 Vertical Axis Wind Turbines

Vertical axis wind turbines experience large fluctuations in the velocity magnitude and direction during each rotation. This is illustrated graphically in figure 1.4, with flow from left to right along the x axis. The component U_a is the portion of the free-stream velocity seen at the rotor plane, this component decreases in magnitude as it passes from the front of the rotor to the back due to momentum extraction. The total wake velocity is thus a complicated function of energy removal by the front and rear halves of the rotor. When the axial component is summed with the rotational velocity, ωR, it produces the relative velocity seen by the blade, U_{rel}. The relative velocity thus constantly changes magnitude and angle of attack with respect to the airfoil chord while the turbine is in operation.

For a blade which is attached tangentially to the rotor circle (dashed gray line of the figure), the angle of attack is given as a function of the axial velocity component, θ and the angular velocity as:

$$\alpha(U_a, \theta, \lambda) = \arctan\left(\frac{U_a \cos(\theta)}{U_a \sin(\theta) + \omega R}\right) \tag{1.30}$$

where in general the axial velocity, U_a is a complicated function of θ and turbine operating conditions. Furthermore, if the airfoil performance can be characterized by 2-D sectional polars then the blade loads can be solved since $C_l(\alpha)$ and $C_d(\alpha)$, if U_a

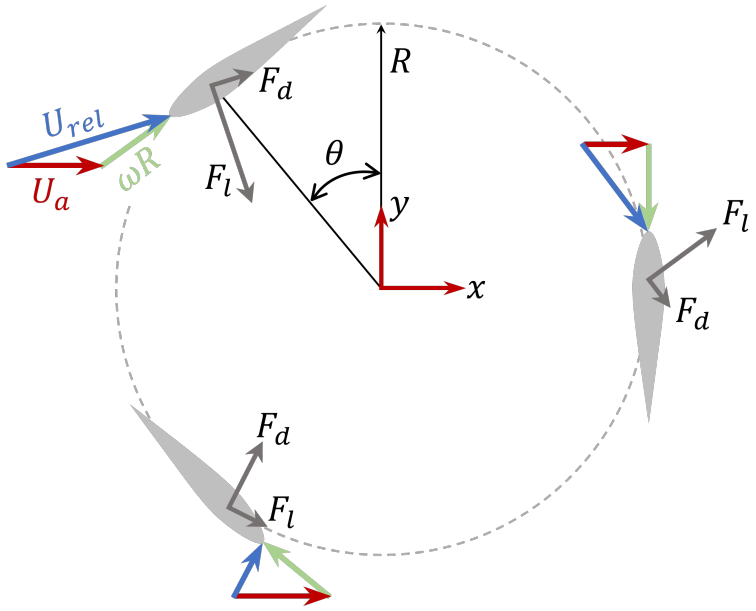

Figure 1.4: Blade geometry for the vertical axis wind turbine during a single rotational cycle.

is known. Because the value of U_a is related to the free-stream velocity, the tip speed ratio of a VAWT gives some indication of the relative magnitude of U_a and ωR and therefore α. For a turbine operating at large values of λ, the load fluctuations are less as U_{rel} is driven by the rotational component. This is easily seen if ωR is allowed to become large in equation 1.30. For low tip speeds near unity, the rotor blade is more likely to see loads which fluctuate more in θ as illustrated in figure 1.4 since the rotational component is nearly the same magnitude as the free-stream velocity. Thus it would seem that VAWTs operating at high tip speed ratios are desirable from a performance standpoint, and indeed early commercial designs operated in this regime (FloWind, 1996). From a mechanical point of view there are some benefits to operating at low tip speeds. Structural loading due to centrifugal forces can be considerable as it scales with ω^2, indicating that lower tip speeds are desirable.

A driving design question is then: how does the choice of wind turbine geometry affect the tip speed ratio and performance? The parameter which has been found to exert significant influence on the operation of a design is the turbine solidity:

$$\sigma = \frac{N_b c}{D} \tag{1.31}$$

with N_b the number of turbine blades. Early research suggested that a value of $\sigma = 0.3$ would produce the most efficient design (Strickland, 1975), while higher solidities (sometimes approaching unity) have been produced commercially (Miller et al., 2018), likely due in some part to the mechanical considerations discussed earlier. Considering the range of operational modes of the VAWT, a separate literature review is undertaken in the next few sections. First is the discussion of dynamic stall, which may occur when there are time-varying changes in α which is certainly the case with the VAWT. This is followed by a review of literature which has investigated the effects of Reynolds number on VAWT operation and performance.

1.5.1 Dynamic Stall

Due to the complicated operating nature of the VAWT, it is also subject to additional fluids-driven effects such as dynamic stall when compared to the HAWT, even when considering the most canonical case of uniform inflow. This is in contrast to HAWT operation under similar conditions where the blade loading remains relatively constant in time (neglecting tower and atmospheric boundary layer effects). Dynamic stall occurs when an airfoil is undergoing a pitching motion in time. It is of interest in insect and animal flight (low Re, low Ma) all the way to combat aircraft (where both Re and Ma are large). The flow physics driving dynamic stall can be much different between these two extremes. For the relatively low Mach number ($Ma \leq 0.3$), high Re operating regime, the primary characteristic of dynamic stall is to increase the peak lift coefficient beyond what would be expected from numerical simulations or wind tunnel experiments of static airfoils. This increase is time and pitch rate dependent, with an associated hysteresis loop that can also alter drag and pitching moment

coefficients of sectional airfoil data (Carr, 1988). The increase in performance is driven by a complicated process characterized in part by vorticity shedding near the leading edge for airfoils pitched at a constant rate (Carr, 1988; McCroskey, 1981). While a complete review of the phenomenon driving dynamic stall is outside the scope of this thesis, the scaling of dynamic stall effects with Reynolds number is of particular interest. It was recognized early on that dynamic stall effects would play an important part in the design of a mechanically robust VAWT (Carr, 1988; Laneville and Vittecoq, 1986), however due to the large velocities needed to achieve high Reynolds numbers in conventional wind tunnels, compressibility effects became a concern. Therefore the literature is limited where Reynolds number effects on dynamic stall are considered. Some early high Reynolds number work is available, but only with a fixed airfoil geometry (Lorber and Carta, 1988). The work of Akbari and Price (2003) compared numerical simulations of a pitching airfoil at various low blade-Reynolds numbers from $Re_c = 3,000$ to $100,000$ with previous simulations at 1×10^6. While the magnitude of the aerodynamic coefficients did increase with Re, as would be expected based on the discussion of section 1.4.2, the general shape of the hysteresis loop was the same for the airfoil geometry tested (N.A.C.A. 0012). Other minor differences were observed but the work concluded that any Reynolds number effects were secondary to dynamic stall phenomena, with Reynolds number changes effectively captured by static airfoil data. For this reason, most of the modeling efforts have elected to neglect Reynolds number effects in their formulations (Hansen et al., 2004; Larsen et al., 2007; Øye, 1991; Schepers, 2012).

1.5.2 VAWT Rotor Effects with Reynolds Number

As discussed in section 1.3, Reynolds numbers are typically large for field-scale VAWT units, making them equally as difficult to test in wind tunnels as HAWTs. Due to the increased cost and complexity of performing full-scale turbine tests, plus the lower

commercial interest in VAWTs, only a few studies have been performed at or near full-scale Re values. Furthermore, if the effect of changing the turbine solidity was also included for study, even less data is available. Recent numerical simulations on the H-rotor geometry using various solidity values have observed clear Reynolds number trends (Lohry and Martinelli, 2016). For each of the solidities tested ($\sigma = 0.13$, 0.25, 0.47, and 0.79), the power coefficient increased with Reynolds number for all values of λ. Furthermore, it was observed that while the specific value of maximum C_p did depend on σ, all cases displayed asymptotic behavior as Re was increased. This indicates that Reynolds number invariant behavior is possible for VAWT geometries.

On the experimental side, laboratory and field tests of VAWTs have been performed using large and full-scale models by Sandia National Labs (Blackwell et al., 1976; Sheldahl et al., 1980; Worstell, 1979). In all cases the general trends with Reynolds number compare well with the H-rotor simulations. Model performance in the form of power coefficient showed an increase with Reynolds number for the given range of λ and solidities tested ($\sigma \in [0.13, 0.3]$), despite the rotor geometry variations between studies. However, the clear plateau-like behavior was not observed for the two smaller-scale experiments (one wind tunnel, the other field of Blackwell et al. (1976); Sheldahl et al. (1980), respectively). It was not until field measurements were made on a much larger turbine that any plateau behavior was observed in C_p with Re, and only for the single tested low solidity value of $\sigma = 0.14$ (Worstell, 1979). The Reynolds number used to characterize the behavior was defined as a chord-based value, $Re_c = \frac{\rho c \omega R}{\mu}$ with invariance to this parameter being achieved at values larger than approximately 1.25×10^6. This indicates that a very large Reynolds number is potentially required for scale-independent behavior. A more recent set of experiments examined Reynolds number effects on high solidity turbines, $\sigma = 0.41$ and 0.44, with various blade configurations (Armstrong et al., 2012). In this work, a lower value of $Re_c \geq 400,000$ is cited as the minimum for invariant behavior with Reynolds number,

although the exact definition of Re_c is not given making it difficult to evaluate this limit. If defined the same as in the mentioned prior work, then there is still some uncertainty surrounding this value. It is possible that the threshold Re_c for invariant behavior in C_p is not a constant, but instead a function of turbine geometry, and possibly subject to solidity effects. There is currently not enough information to draw a definitive conclusion.

1.6 Motivation and Outline

From the preceding literature review of VAWT and HAWT effects with Reynolds number, it is clear that a need exists to experimentally quantify rotor performance changes over a range of Re which spans representative field-scale values. Prior work has been completed at large scale, but typically at singular values of Re, limiting investigations of scale effects. Furthermore it is desired to perform these experiments in a laboratory context without the added complexity and inflow uncertainty present in field experiments. This would allow for the Reynolds number scaling of the canonical case with laminar inflow to be studied in detail. A fundamental study of this type is crucial for understanding the basic flow physics surrounding rotating systems and could be used as a reference case for validation tests and model building. Laboratory studies are also advantageous in that relatively small models may be used so that cost and complexity are manageable. The following chapters of this thesis document the design and development of an experimental campaign specifically focused on high Reynolds number scale effects for both HAWTs and VAWTs. To accomplish this, the typical model scaling issues as discussed in section 1.3 for these types of experiments were bypassed by using highly compressed air as the working fluid. This allows for a reduction in the kinematic viscosity by over two orders of magnitude, enabling Reynolds numbers in excess of 200 times that available with the same

model in atmospheric air. Additionally, this method has the advantage of maintaining tip speed ratio and Mach number similarity. To accomplish this, a specialized, high static pressure wind tunnel known as the High Reynolds number Test Facility (HRTF) was utilized along with small-scale wind turbine models and measurement tools specifically designed to operate in this environment. The thesis is organized as follows:

Chapter 2 provides background and details on how the experimental setup was developed. Both the HAWT and VAWT models are described in detail, including all relevant geometry necessary to re-create these studies.

Chapter 3 investigates results from the horizontal axis wind turbine. First, a novel method of data validation is described followed by a discussion of the results. Specific focus is placed on power and thrust coefficient scaling with Reynolds number, and a definition of the Reynolds number which characterizes Re effects is shown to effectively capture the trends seen in the data sets. Following this is an investigation of transition effects by application of micro-dot tripping devices to the rotor surface. Results are compared to the smooth rotor and conclusions made as to the effectiveness of using transition to eliminate some of the scale effects observed.

Chapter 4 describes results from the vertical axis wind turbine experiments. Data validation is performed in a similar manner to the HAWT, followed by a detailed investigation of Reynolds number effects for a single solidity which is modeled on an existing, field-scale turbine. Next, the solidity is changed and the experiments repeated to observe changes in the power coefficient scaling with Re and σ. This gives a broad characterization of the operating space of this turbine geometry and insight into VAWT scaling behavior.

Concluding remarks are made in chapter 5 followed an appendix which gives additional detail regarding the tower and gearbox design used in the HAWT experiments (appendix A).

Chapter 2

Setup

In order to perform experiments in a highly-pressurized environment, special care must be given to the design and implementation of experimental models. At maximum static pressure of the wind tunnel used in this thesis, the fluid density can exceed 200 times that of atmospheric air, which has the direct effect of increasing the forces and moments on the model by 200 times. In addition the fluid velocities can reach 10 (m/s), further adding to the model loads. Therefore, a large amount of effort went into the design and manufacture of both the horizontal and vertical axis wind turbine models. In addition, a test rig was constructed external to the wind tunnel for bench testing the models and their drive-train components. This allowed for preliminary quantification of drive-train losses and mechanical natural frequencies as described in section 2.4.2. Due to the limited access of the test section while the HRTF facility is in operation, a complete measurement and control stack was also designed to quantify loads produced by the model plus provide reliable control of rotational speed via braking torque on the drive-shaft. The measurement stack, as it is known, serves the purpose of a lift/drag balance, torque and speed transducer, plus braking loads in a single, removable package which fits entirely inside the pressurized environment of the HRTF. The time-span to produce all of this equipment took the

better part of two and a half years to complete. This chapter of the thesis provides a detailed description of the design and manufacture of these elements, how they interface with the facility, and the main features of the data processing and uncertainty calculations used to quantify the results.

2.1 Introduction

The two dependent parameters of interest when considering the global performance of a wind turbine model are the power and thrust coefficient:

$$C_p = \frac{\tau\omega}{\frac{1}{2}\rho U^3 A} \qquad\qquad C_t = \frac{F_t}{\frac{1}{2}\rho U^2 A} \tag{2.1}$$

where A is the frontal area swept by the turbine, τ is the total aerodynamic torque on the central shaft, and F_t is the axial thrust force. All dependent, non-dimensional groups for this physical problem rely only upon the parameters set in equations 1.24 and the length-scales of the rotor geometry. This implies that different combinations of U, ρ, and ω can be used to vary the physical input loads but produce the same Re, λ, and Ma, thus the same values of C_p and C_t. Scaling relations such as these are exploited to validate experimental data in chapters 3 and 4. These relations also give the scaling of mechanical loads with rotor geometry, density, and velocity. The measurement stack used to quantify these loads while providing structural support to the wind turbine models is discussed in section 2.3. Sections 2.4 and 2.5 discuss in detail the design decisions for both horizontal and vertical axis wind turbine models, respectively. First is an overview of the high pressure wind tunnel facility used in these experiments.

2.2 The High Reynolds Number Test Facility

To achieve field-scale Reynolds numbers on both horizontal and vertical axis wind turbine models, a specialized, high static pressure wind tunnel was employed, known as the High Reynolds number Test Facility, and referred to as the HRTF for the remainder of this thesis. The wind tunnel is a closed-loop, recirculating type designed to operate at very high static pressures, but relatively low velocities using compressed, dry air as the working fluid. The HRTF can support static pressures up to 233 (bar), or in excess of $3,300$ (p.s.i.), and free-stream velocities up to 10 (m/s). The facility has been used in prior work for high Reynolds number studies of turbulent boundary layers (Vallikivi et al., 2015), submarine wakes (Ashok et al., 2015; Jiménez et al., 2000), and sectional airfoil measurements (Kiefer et al., 2016).

As can be seen by equations 2.1, both the power and thrust coefficient scale linearly with the fluid density. For a facility operating with compressed air as the working fluid, density is given by the real-gas relationship:

$$\rho = \frac{p_\mathrm{s}}{ZRT} \tag{2.2}$$

where R is the specific gas constant for air, T the tunnel temperature, p_s the static pressure, and Z the compressibility factor. For dry air, Z changes by only 10% for values of p_s over the range 0-233 (bar), meaning that for a constant temperature, density is nearly linearly related to pressure. This implies that a model operating near the maximum p_s, will see mechanical loads which are in excess of 200 times that seen by the same model operated at atmospheric pressure, as evident from equations of 2.1. For this reason, considerable care was given to the mechanical design of models, measurement equipment, and support structures as detailed in the sections that follow. The key to achieving dynamic similarity in this facility is not only the high static pressure, but also that dynamic viscosity and sound speed are a weak

function of p_s. The value of μ changes by 30% and a by 12% from their values at atmospheric to full tunnel pressure, in contrast with density which increases 21,900% (all determined using real-gas relationships). For all experimental results, the exact density and viscosity of the compressed air is found using real-gas relationships with measurements of p_s and T, as outlined in Zagarola (1996).

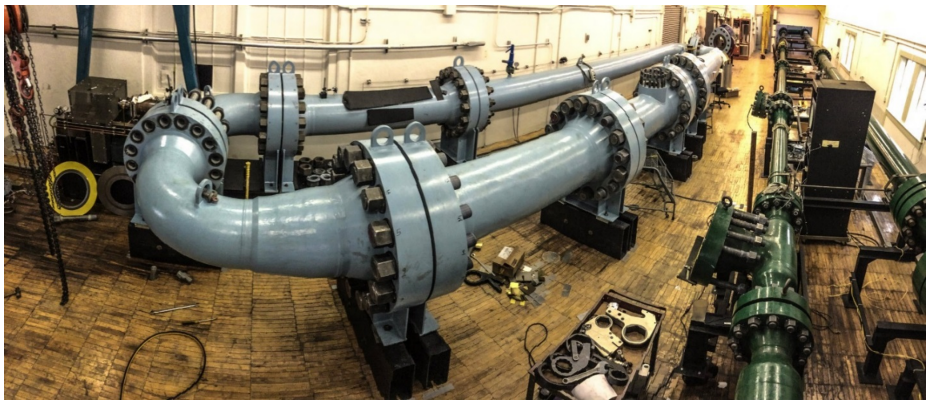

Figure 2.1: Photograph of the high-pressure wind tunnel known as the HRTF (in blue).

A schematic of the HRTF is shown in figure 2.2. The tunnel contains two test sections with a total length of 4.88 meters; each having a circular cross-section with an inside diameter of 0.49 meters. Models are installed via a single 0.254 (m) access port located on the top of the facility. The entire measurement-stack, as discussed in section 2.3, mounts inside this port via three weld-tabs with $\frac{1}{2}$-20 mounting studs. Only electronic signals passed into the sealed tunnel during operation by means of a high-pressure feed-through (Conax Technologies Inc.). Signals included control lines for the braking loads plus all voltage outputs from the various sensors. The test sections are preceded by a contraction with an area ratio of 2.2:1, in which are located a series of honeycomb flow straighteners and conditioning screens. These devices are configured to produce a laminar, slug-type flow inside the test sections with a measured turbulence level of 0.3% at the lowest tunnel Reynolds number and 1.1% at the highest (Jiménez et al., 2010). Thus operation of the facility is very

similar to a conventional, atmospheric wind tunnel designed for laminar test-section flow. The HRTF is not actively cooled, and does experience temperature increases in the working fluid if the run-time is sufficiently long, especially at high tunnel pressures and velocities. For the experiments in this thesis, the experimental run-times were kept short and tunnel heating minimized. In addition, any small temperature and static pressure changes during a run were measured and used to determine the true fluid properties using real-gas relationships.

The flow conditions in the tunnel were determined with a host of different sensors located inside the HRTF. The free-stream velocity is measured via a pitot-static tube (United Sensor model USNH-A-368) located upstream of the turbine model. This sensor was connected to a differential pressure transducer (Validyne DP-15) with a range of ± 13.79 (kPa), or ± 2 (p.s.i). Installation and calibration of this sensor was completed in-lab and is discussed in section 2.8. Fluid temperature was measured with a resistance temperature detector (RTD, by Omega Technologies Corporation). The RTD was located upstream of the flow-conditioning section via a small plug and connected to a digital temperature readout (Omega model 199) which outputs an analog voltage into the data acquisition system. Static tunnel pressure was measured via a transducer connected to a pressure port located upstream of the flow-conditioning section of the HRTF. The transducer had a range of 275.8 (bar), or $4,000$ (p.s.i.), (Omega model PX303) which was connected to a digital readout (model DP41-E, also from Omega). The readout produced an analog voltage which was subsequently fed into the data acquisition system. Finally, the data was acquired using two different data acquisition cards. The first was an eight-channel, simultaneous sample and hold P.C.I. card capable of sampling frequencies up to 500 (kHz.), (National Instruments model PCI-6123). This unit read in the voltages output by the temperature sensor, static pressure sensor, differential pitot-static transducer, torque transducer, and rotational speed encoder (the last two sensors are discussed in section 2.3). The second

data acquisition system was an eight-channel, multiplexed unit connected via universal serial bus with a maximum sampling rate of 400 (kHz.), (National Instruments model USB-6212). The purpose of this second data acquisition card was to sample all six channels of the load cell (also discussed in section 2.3). Both data acquisition systems had sixteen bits of analog resolution, and were synchronized to start acquiring data at the same time during a run. A detailed uncertainty analysis for each of these sensors can be found in section 2.8. Further details of the facility can be found in (Jiménez et al., 2000).

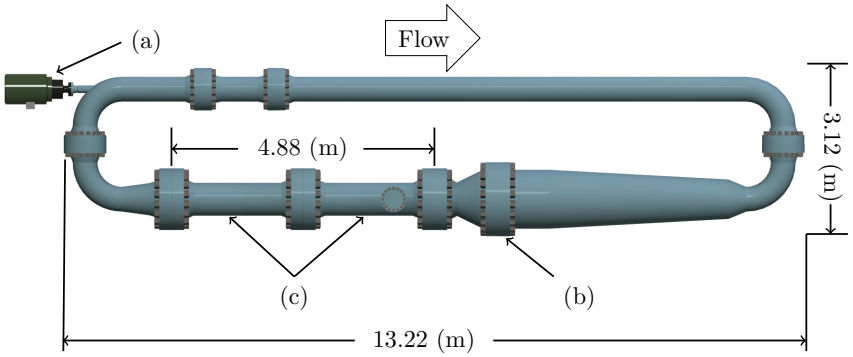

Figure 2.2: Schematic diagram of the HRTF as viewed from above the facility. The figure labels correspond to: the 150 kW pump motor in (a), the flow conditioning and contraction in (b), and the two test sections in (c).

2.3 Measurement Stack

A measurement stack was designed to interface with both wind turbine model geometries and accurately resolve the forces and moments generated during an experimental campaign. The entire assembly was located inside the pressurized environment of the HRTF with only an electrical feed-through to the atmospheric side. The fundamental components of the measurement stack are a load cell for measuring forces and moments, a torque transducer for shaft torque and rotational speed measurement, a

brake for speed control, and a machined aluminum structure which locates all components in the wind tunnel. The actual measurement stack is shown in the images of figure 2.3. Design and manufacture of the measurement stack was performed in-house with the assistance of Christy Elford (Elford, 2015).

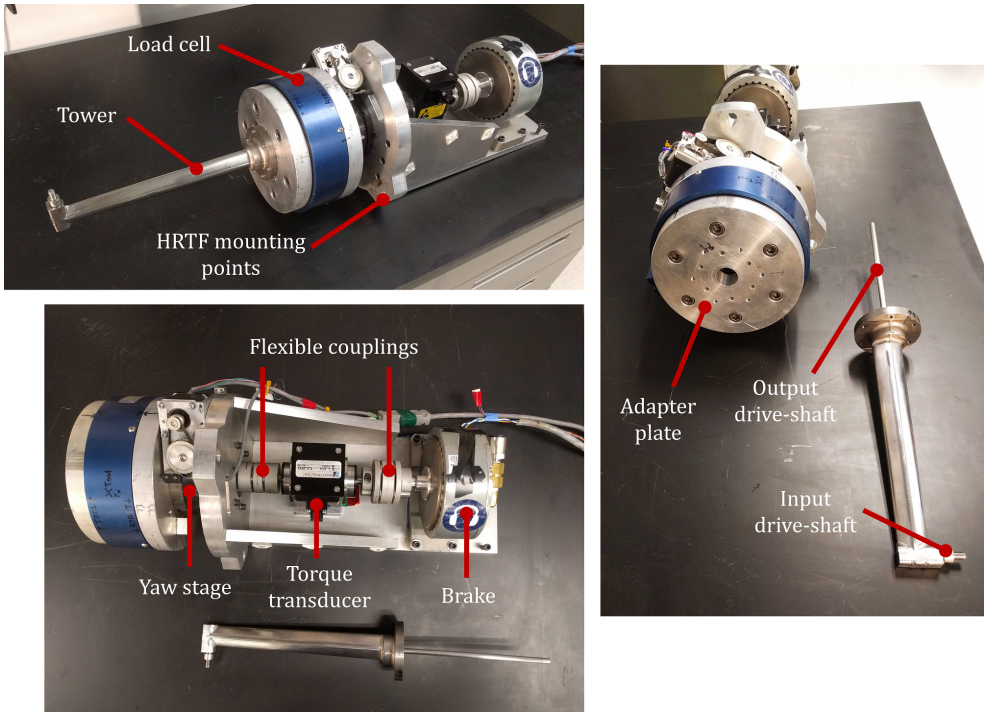

Figure 2.3: Composite picture of the completed measurement stack with HAWT tower for reference.

During an experiment, the hub of the rotor under test is located in the tunnel centerline and attached to the input drive shaft of the tower. This drive-shaft is different for both HAWT and VAWT models, as is the tower geometry, but the output shaft dimensions are the same and allow for interfacing with the measurement stack. The first element of the measurement stack is an adapter plate with a bolt pattern which adapts both HAWT and VAWT towers to the three-axis force/moment (six component) load cell (JR3 Incorporated model 75E20A4). A second adapter plate is fitted between the load-cell and the yaw table. Turbine yaw was nominally set to zero degrees for all experiments. However, future work may investigate the effects of yaw angle on rotor performance. The yaw table consisted of a four inch diameter

rotary table (Sherline Incorporated) driven with a stepper motor connected via a belt drive. This configuration was chosen due to the limited mounting space available in the access port of the test section. The yaw table was then bolted to the tunnel adapter plate which has three outer tabs for locating the entire measurement stack on matching welded tabs with threaded studs inside the HRTF. The tunnel adapter plate is critical in locating the model in the tunnel and transferring all reaction forces and moments generated to the tunnel wall. Following the adapter plate is a boxed-in aluminum section with a plate for mounting both a torque transducer and the brake unit. Shaft power is transferred from the tower along an extended output shaft, which passes through the three adapter plates, load cell, and yaw table via a centrally located hollow section. The shaft is then connected via a flexible coupling (Zero-Max Incorporated, double-flex SC series) to a torque transducer (Magtrol Incorporated model TM-305 with a dynamic torque range of ± 2 Nm). This unit is also equipped with an optical encoder on an internal shaft and allows for resolution of the rotational speed at sixty instances per rotation. Rotor speed is controlled with a magnetic hysteresis brake (Magtrol model AHB-3), located directly after the torque transducer and connected via a second flexible coupling.

The combination measurement stack and wind turbine tower/model is assembled as a single unit. This was a necessity as the configuration of the HRTF during these experiments had only a single access port available for inserting the model into the tunnel. This is convenient for bench testing of the setup outside of the wind tunnel, as was necessary for determination of the HAWT gearbox efficiency (as discussed in section 2.4.2).

2.4 Horizontal Axis Wind Turbine Models

One of the central challenges of testing in a pressurized environment are the large forces and torques present, which if unaccounted for can cause unacceptable model deflections and possibly failure. Therefore, careful consideration was given to model design and construction so as to minimize rotor deflections during even the most extreme of operating conditions. This section gives an overview of the design methodology for the horizontal axis wind turbine rotor as well as the tower/gearbox used to locate the rotor inside the test section and transfer power/forces outside for measurement.

2.4.1 Model Design and Geometry

Initial rotor design began by choosing an appropriate rotor diameter which would give acceptably low blockage in the tunnel and still provide high Reynolds numbers on the order of field-scale units. For the HAWT model, diameter was set to $D = 20$ (cm) which gives a blockage of 16.7% using the rotor swept area and a maximum Reynolds numbers of $Re_D \approx 20 \times 10^6$ in the HRTF. The operational map for the HRTF when using this model is given by the contour plot of figure 2.4. In general, experiments at maximum tunnel pressure and velocity are difficult to achieve due to rapid heating of the HRTF. The turbine gearbox is mechanically limited to $\tau \leq 1.2$ (Nm), as discussed in section 2.4.2. These factors combine to limit the practical Reynolds numbers possible to $Re_D < 15 \times 10^6$.

Initial rotor geometries were inspired by the Vestas V27 wind turbine (Vestas Corporation, 1994), which has a diameter of $D = 27$ (m), because this turbine has a comparable Re_D range to that achievable in the HRTF. Given field conditions of $\rho = 1.225$ (kg/m^3) and $\mu = 18.26 \times 10^{-6}$ (Pa·s), this unit achieves $Re_D = 16 \times 10^6$ at $U = 8.83$ (m/s). Implying that a model can be used to simulate large-scale field

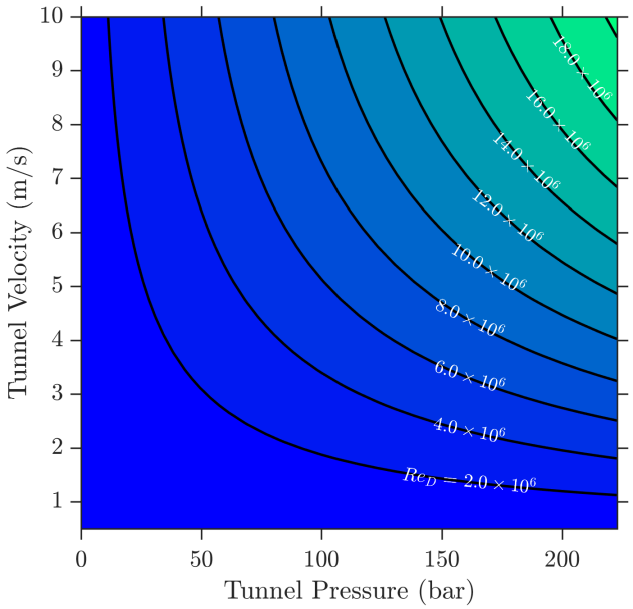

Figure 2.4: Contour map of Re_D with a $D = 20$ (cm) model for given HRTF tunnel conditions.

conditions in the HRTF, with the caveat that the experiment inflow is completely laminar. There is a significant advantage in studying a model with reduced inflow complexity, namely the fundamental flow physics of a model are made more evident when the initial condition complexity has been reduced. This allows for careful study the HAWT operation in what could be considered the canonical case. Chapter 3 contains additional discussion regarding the implications on dynamic similarity.

Prototype development and testing was performed by Arthur Phidd (Phidd, 2015) using a preliminary test blade geometry which was a scaled-down version of the V27 rotor to 1:135 the size. That work concluded with an experiment where loads were applied to the test blade which were in excess of those expected during operation in the HRTF. No failure of the blade was observed. The final rotor geometry was modified from the full-scale geometry by increasing the chord length across the entire rotor by a factor of three. It is therefore not a geometrically similar model to the V27. This was done to increase the blade Re and definitively avoid any low Reynolds number airfoil behavior as described in section 1.4.2. This decision was justified

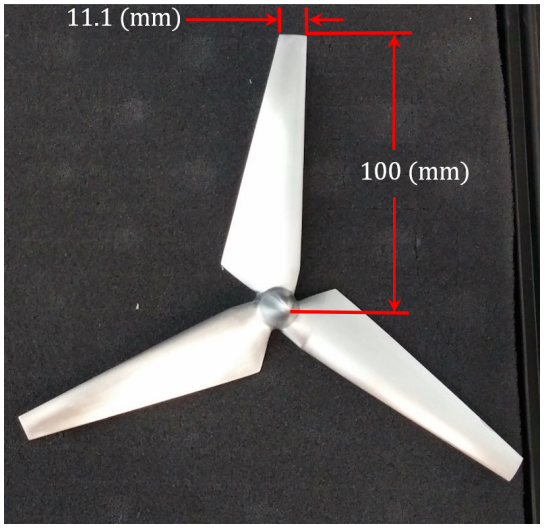

Figure 2.5: Horizontal axis wind turbine model.

Table 2.1: Model HAWT rotor geometry given as a function of radial section.

Section	Radius (mm)	Chord (mm)	Twist (degrees)	Airfoil
1	3.704	11.11	13	Circular
2	14.815	28.89	13	NACA 63-235
3	100	11.11	0	NACA 63-214

for two further reasons; firstly the HRTF does not currently permit matching of the inflow conditions present at the field site and secondly no reliable source of field power measurements for the V27 is currently available. The final model rotor is shown in figure 2.5 and details of the driving airfoil sections as a function of radial position are given in table 2.1.

The airfoil thickness, chord, and twist distribution as a function of radial location is only given for three sections in the original Vestas specification as shown in table 2.1. Therefore, between these sections the geometry was not strictly defined and thus was a free-parameter. In an effort to make the model easy to replicate with a high level of accuracy, the following describes in detail the final geometry used in the experiments of this thesis.

$$\text{Thickness } (\%) = \begin{cases} 100, & \text{if } r = 0 \\ 585.01\left(\frac{R-r}{R}\right) - 463.34, & \text{if } 0 < \frac{r}{R} \leq \frac{4}{27} \\ 27.42\left(\frac{R-r}{R}\right)^3 - 61.41\left(\frac{R-r}{R}\right)^2 + 57.07\left(\frac{R-r}{R}\right) + 14, & \text{otherwise} \end{cases} \tag{2.3}$$

$$\text{Twist } (^\circ) = \begin{cases} 13, & \text{if } \frac{r}{R} \leq \frac{4}{27} \\ 18.148\left(\frac{R-r}{R}\right)^3 - 7.698\left(\frac{R-r}{R}\right)^2 + 8.504\left(\frac{R-r}{R}\right), & \text{otherwise} \end{cases} \tag{2.4}$$

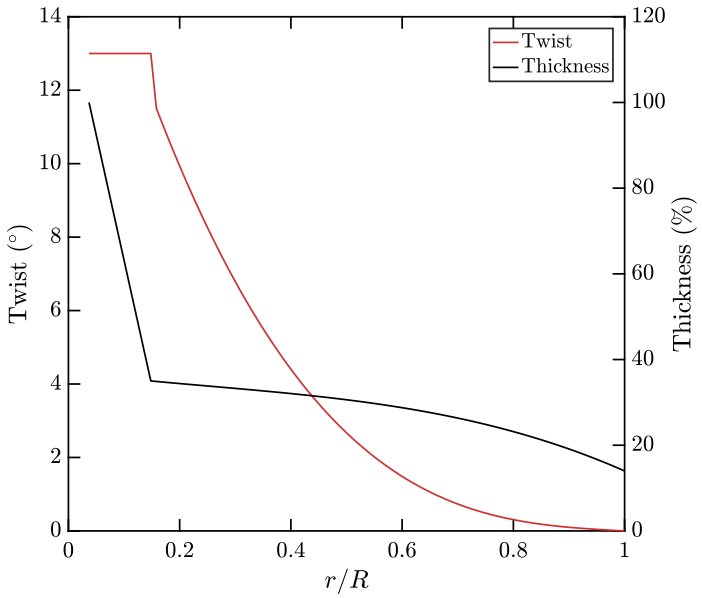

Figure 2.6: Thickness and twist distributions of HAWT model rotor as a function of non-dimensional radius.

For the airfoil thickness, the model has a linear distribution between sections 1 and 2, but is nonlinear between 2 and 3, as given by equation 2.3. In a similar manner, twist is defined as nonlinear between sections 2 and 3, however it is a constant 13° between 1 and 2 as given by equation 2.4. The distribution of both the twist and thickness schedules is shown graphically in figure 2.6. The chord schedule was also

not strictly specified except at the three stations. For the model, chord between sections 1 and 2 is purely linear while the same is also true between sections 2 and 3 of table 2.1 (with different slopes and intercepts as determined by the sections). The rotor pitch remains fixed at $+5^\circ$ for the model, where pitch is defined as positive into the flow from the rotor plane. The normal of this rotor plane is aligned with the axis of rotation, which in turn is aligned with the incoming flow for all experiments. Therefore the yaw, cone, and teeter angle have all been set to 0°. The model hub is defined by a spinner cone on the side facing the flow, and a flat surface on the back-side with a central mounting hole tapped to M7 $\times$ 1 so the model can be attached to the tower. The spinner geometry was taken directly from Reynolds (1953), and consists of a N.A.C.A. 1 series spinner. The outer diameter of the hub is scaled to overlap with the section 1 of table 2.1 so that the final spinner diameter was $D = 16$ (mm).

Due to the small feature size and strict tolerance on surface requirements, the final rotors were milled from solid blocks of 6061 Aluminum using a computer numerical control machine with five axes. Surface roughness was carefully measured using an Olympus LEXT OLS4000 confocal microscope and the area-averaged, root-mean-square roughness height was found to be:

$$S_q = \left(\frac{1}{A} \iint_A Z^2(x, y)\, dx\, dy \right)^{\frac{1}{2}} \leq 0.8 \pm 0.25 \ (\mu\text{m}) \tag{2.5}$$

where Z is the measured surface data with total area of A (Keyence Corporation, 2018). The value of $S_q \leq 0.8$ (μm) was found to be consistent among all three blades.

2.4.2 Tower Design and Gearbox Correction Methodology

The wind turbine tower used in these experiments was completely designed and manufactured by the author. The primary functions of the tower were to: accurately locate the model in the tunnel, minimize deflection even at the highest rotor loading

cases, minimize interference with the flow, and transfer the loads generated by the rotor outside of the test section. The last of these requirements necessitated a method of turning shaft torque from the axis of turbine rotation to the axis aligned with the measurement stack; located at right angles to each other. This required the development of a compact gearbox assembly which could fit inside the turbine tower and withstand the shaft torque produced by the model. The following sections describe the development of this tower and the internal gearbox. Furthermore, due to the presence of the gears, a method was developed to measure the inherent losses by using a test rig constructed for the purpose and then develop a correction methodology to recover the true aerodynamic input power.

Figure 2.7: Computer rendering of the HAWT tower assembly with prototype rotor geometry for reference. Cut-away detail shows the internal gearbox geometry.

The tower was custom designed, which had several advantages when compared to purchasing an off the shelf unit. Operating conditions inside the HRTF were considered from the outset, with the large fluid densities driving the majority of load cases. Commercial gearbox units which could handle these loads were unnecessarily bulky and would have severely disrupted the flow behind the model (and possibly affected upstream performance as well). In addition, it would have been necessary

to employ a series of separate drive-shafts in order to transfer power out of the test section, an unnecessary complexity. Therefore a custom tower/gearbox combination was designed by the author to accommodate the special operating conditions of HRTF experiments. The design methodology is described in appendix A for the range of loading cases expected in the HRTF from the model of section 2.4.1. The finished unit consists of what would conventionally be considered both the tower and nacelle of a wind turbine. Inside the tower is a compact, right-angle gearbox with a $1:1$ ratio plus the supporting bearings and space for lubricant. Power is transmitted from the rotor to the input shaft, through the gearbox, and onto the output shaft where it is then fed into the measurement stack. The tower housing was machined using computer numerical control from a solid bar of 17-4 PH high-strength steel. Outer tower geometry was optimized using the finite element solver available in Pro-Engineer/Creo to minimize deflections and frontal area while allowing enough internal volume to accommodate the model gearbox and drive-shafts. The final tower design can withstand up to 3 (Nm) of shaft torque and over 300 (N) of axial thrust loading while minimizing the largest deflections to less than 400 microns (Miller et al., 2016). A computer rendering of the tower with a cut-away of the internal gearbox is shown in figure 2.7.

Due to the presence of a gearbox in the tower assembly, the measured shaft power needs to be corrected for any internal losses so that the true, aerodynamic power may be recovered. This is the power produced by the rotor upon interacting with the flow, and is the parameter of interest when making comparisons against models and numerical simulations. A correction methodology was adopted to directly measure the efficiency of each gearbox using a separate test rig as shown in figure 2.8. The test rig was also designed in-house with the goal of replicating the aerodynamic shaft power levels that a gearbox would experience while undergoing an experiment in the HRTF with the model rotor. The test rig did not replicate the thrust loading from

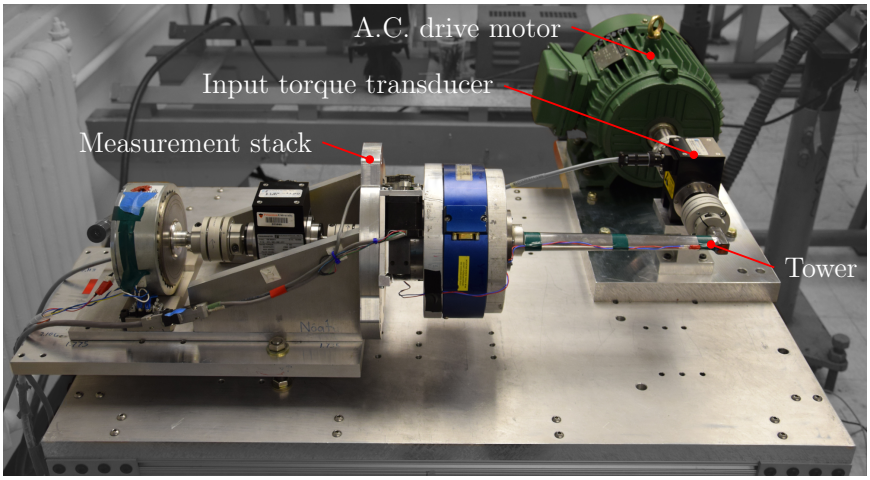

Figure 2.8: Test rig shown with measurement stack loaded for efficiency tests.

the HAWT rotor, but this appeared to have no effect on the efficiency correction as shown by the validation data of section 3.1. The base of the test rig is a 50 (mm) thick section of ground aluminum fixture plate measuring 0.61×0.91 (m) . A series of locating holes were machined into the plate which allow for mounting of the entire measurement-stack and tower used in the HRTF experiments. The exact same drive-train used during an experiment can then be be completely characterized external to the HRTF. Also mounted to the test rig was a 2.24 (kW), or 3 (h.p.), variable-frequency, alternating current motor connected to a torque transducer via a flexible coupling. The motor provided input power (in lieu of the rotor) for a given range of set-speeds using a variable frequency drive. Input power was measured by the torque transducer before entering the tower via a second flexible coupling (taking the place of the rotor). Power out is measured in the same way as during an experiment: by the output-shaft torque transducer. Power is removed by the brake. Control of the test rig is fully automated with National Instruments Labview for a range of set speeds and brake loads which are representative of those generated by a model rotor operating in the HRTF.

Three different gearboxes were used for the HAWT data of chapter 3, named gearbox 1, 2, and 3. Losses within the gearboxes mainly stem from the constant

meshing of gear teeth inside the turbine tower, but can also be attributed to frictional losses in the bearings and lubricant. To capture these effects, a bulk efficiency is defined as the ratio of output to input power. The most general, functional form of the gearbox correction was:

$$\varepsilon = \frac{[\tau\omega|_{\text{output}}}{[\tau\omega|_{\text{input}}} \tag{2.6}$$

where ε is the measured efficiency and the subscripts "input" and "output" refer to the measurement location with reference to the gearbox. During post-processing of experimental HRTF data acquired with a particular rotor, the aerodynamic input power is recovered with the use of measured test rig data. This is accomplished by parameterizing test rig data using a curve fitting routine. The coefficients of the curve fit are specific to each gearbox and are typically generated using 150 different operating points (torque and speed settings) to ensure an accurate fit.

The mapping of ε was accomplished in several steps. Shown in figure 2.9 are the measured efficiency data points as a function of the output torque and speed. These points are fitted with a linear surface interpolant for visualization purposes in the figure. In general, the test points spanned the following ranges:

$$\tau \in [0.1, 1.2] \text{ (Nm)} \tag{2.7}$$

$$\omega \in [105, 566] \text{ (rad/s)} \tag{2.8}$$

Data points at lower values of τ occasionally exhibited large fluctuations in ε. Placing a basic filter on the data for fitting such that the standard deviation of the torque must be less than half the mean value (i.e., $\sigma_\tau/\tau \leq 0.5$) effectively filtered out these points. Erroneous values of the drive-train efficiency also occurred at low operating speeds, below $\omega \approx 126$ (rad/s) or $1,200$ (r.p.m.), which is attributed to

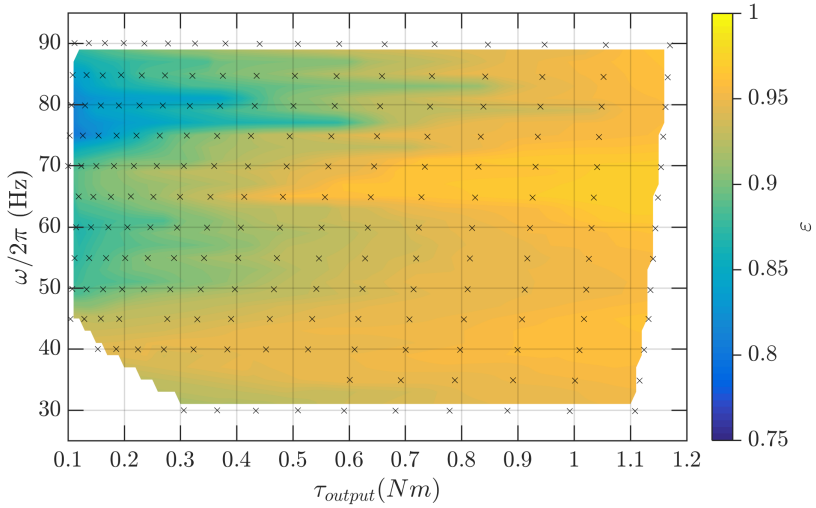

Figure 2.9: Measured drive-train efficiency as a function of output speed and torque for a single gearbox. Black markers denote measured test points while the color-contour is a linearly interpolated surface for visualization.

drive-train harmonics. This presented less of an issue for the experimental data where operational speeds in the HRTF were typically much higher than this value. Measured data which fell outside the fitted range given by 2.7 and 2.8 was not included in post-processed results.

A functional and repeatable methodology was desired to simplify the mapping of measured power to the true aerodynamic power. Given the results of figure 2.9, the measured efficiencies have very little dependence on rotational speed and therefore a fit of the form $\varepsilon = f(\tau)$ was sought. A power-law relationship was found to capture the changes in efficiency with torque:

$$\varepsilon = a(\tau_{\text{output}})^b + c \tag{2.9}$$

where a, b, and c are adjustable constants determined by a best fit of the measured efficiency from test rig data. Since the dependency on ω has been eliminated, data was bin-averaged by τ across all speeds in steps of $\Delta\tau = 0.05$ (Nm) over the range given in equation 2.7. The standard deviation of all data points from their bin-

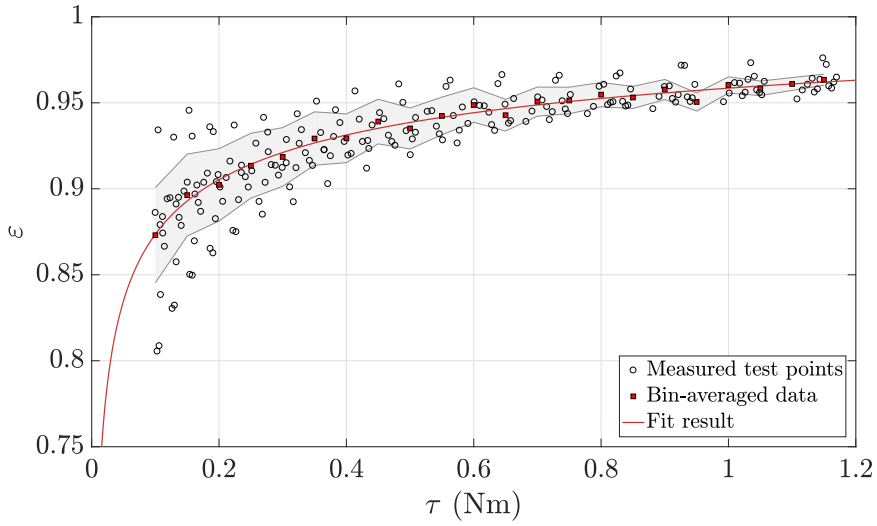

Figure 2.10: One-dimensional drive-train efficiency shown as a function of input torque for gearbox 2. Note that data is identical to that shown in figure 2.9.

Table 2.2: Values of the coefficients used in the efficiency correction for each of the three gearboxes.

Gearbox	a	b	c
1	-4.425	-0.007	5.383
2	-0.090	-0.228	1.049
3	-0.780	-0.036	1.727

averaged value gives an estimate of the uncertainty associated with neglecting any dependency on rotational speed. Results of this method are shown in figure 2.10 for gearbox 2. Note that although some scatter is present in the data sets, the trend of the bin-averaged data points is well captured by the curve fit routine. The resulting curve fit parameters are given in table 2.2 while the plots of figure 2.11 show these curves compared against one another. Validation of this methodology using various experimental data sets is discussed in section 3.1.

2.4.3 Final HAWT Model and Measurement Stack

The resulting tower and HAWT model is shown as a computer rendering in figure 2.12. The view of the test section has been flipped upside down for clarity, in reality the access port for mounting the model is located on the top of the HRTF and the model

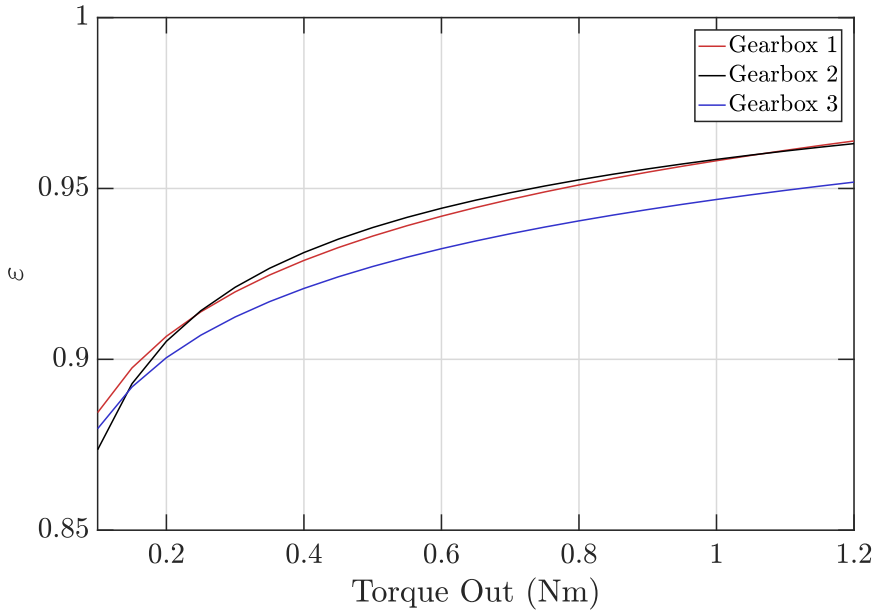

Figure 2.11: Comparison of drive-train efficiency fits for the three different gearboxes used to correct the HAWT data of chapter 3.

hangs down into the test section. The completed measurement stack has also been included in the figure to show the packaging constraints on the system. The blue section is a cut-away of the HRTF's 250 (mm) access port and test section. Note that a spool piece was added to extend the pressurized volume of the access port and is where the bulk of the measurement stack resides. Two small, removable curved plates maintain the tunnel wall profile near the model, and are put into place after a model is fixed in the wind tunnel. There is no pressure-sealing across these curved plates. The entire volume of the tunnel and spool piece are pressurized at the same time with the only connections to outside the pressurized environment being the electrical feed-through. Reliability of the system was tantamount as no optical access is available, and the de-pressurizing routine is lengthy meaning access is severely restricted should something fail to function.

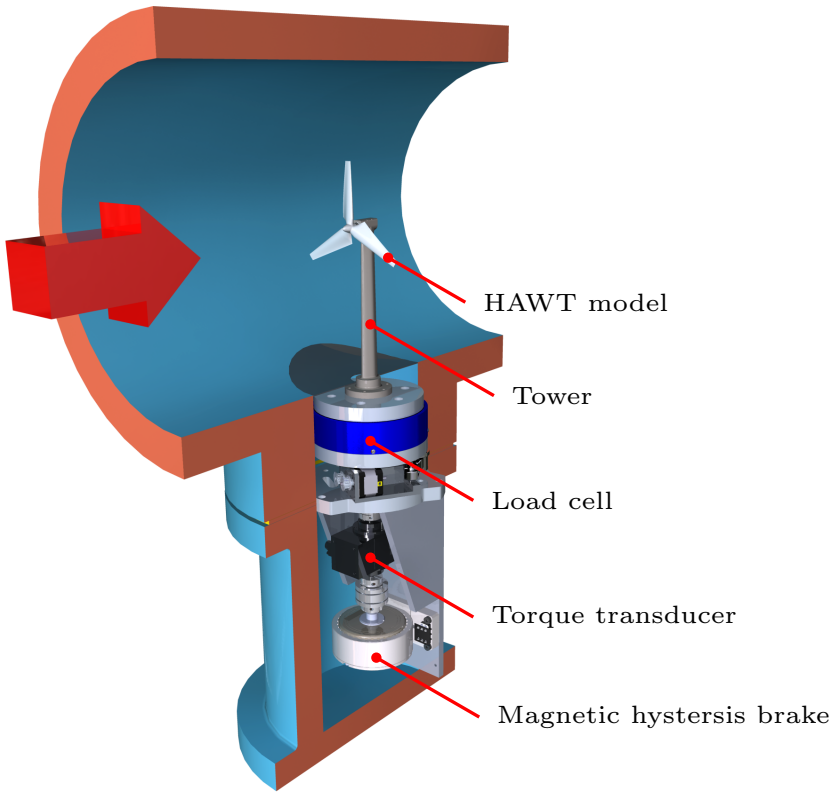

Figure 2.12: Computer rendering of the HAWT model, tower, and measurement stack inside a cut-away of the HRTF test section. Flow direction is given by the red arrow.

2.5 Vertical Axis Wind Turbine Model

The vertical axis wind turbine model utilized the geometry of a commercially available design (produced by Wing Power Energy) with a scale reduction of 1:22.5. Results from this model and comparisons to field experiment data were first made in Miller et al. (2018). Details of the model are given in table 2.3 with the main geometric features of the full-scale retained on the model. Small changes were made to the model hub and support tower to accommodate the increased mechanical loads present. In addition, the full-scale unit uses a modified N.A.C.A. 0021 airfoil where a section near the trailing edge is removed to aid in self-starting. This detail was not replicated on the model as it was expected to have a limited effect on steady-state operation and the model had no self-starting issues.

The scale reduction chosen for the model allowed for a relatively small blockage ratio of 8.36%, and the resulting data was not corrected for blockage effects. The reason for this decision is that the thrust coefficient values were often in excess of unity, which can cause failure of the quasi-one dimensional assumptions used when deriving the classical correction based on the work of Glauert (1935), but discussed in many other works (see e.g., Bahaj et al. (2007); Chen and Liou (2011); Mikkelsen (2004)).

Table 2.3: Vertical axis wind turbine model geometry with details given for the five-blade configuration.

Number of Blades	$N_b = 5$
Diameter (mm)	$D = 96.60$
Total Span (mm)	$S = 162.58$
Chord (mm)	$c = 21.63$
Scale Ratio	$22.5 : 1$
Blockage Ratio	$(SD)/A_{tunnel} = 8.36\%$
Solidity	$N_b c/D = 1.12$
Roughness (μm)	$S_q = 0.5 \pm 0.25$

The mechanical design of the VAWT model was performed in two stages. The tower was originally designed in collaboration with Marcus Lee (Lee, 2015) for a different rotor geometry, but was utilized with the current model when load cases were deemed conservative. The tower itself consists of an outer steel housing with a mounting base at the bottom for connection to the measurement stack. Inside the housing is the central drive-shaft which is located axially by a ball-bearing at the base and a needle bearing near the rotor hub. The hub holds the rotor-blades in place and is press-fit onto the drive-shaft, then pinned in place. Unlike the HAWT tower, no gearbox is necessary for the VAWT and hence no corrections are applied for losses in the tower. The external rotor geometry was set by the commercial unit, but the mechanical load estimation and subsequent analysis was performed by Lucy Tang and Soumya Sudhakar (Tang, 2017). Further details of the design can be found in that work. The final rotor is shown in the computer rendering of figure 2.13.

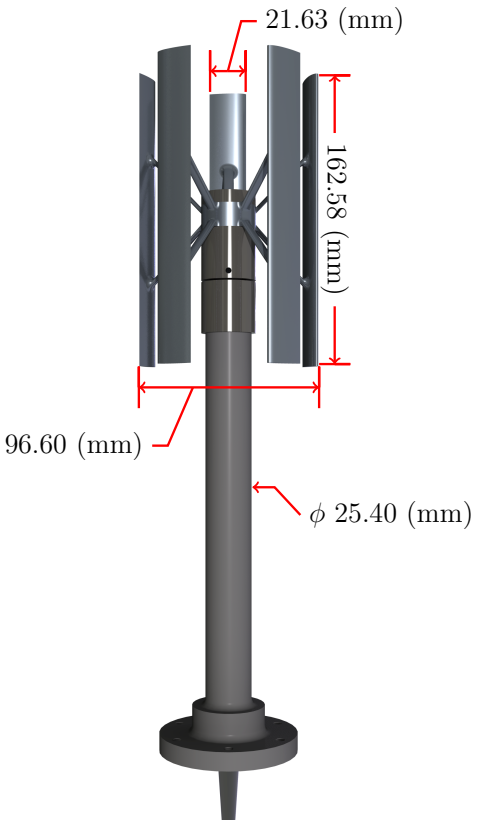

Figure 2.13: Computer rendering of the five blade VAWT model with dimensions.

Manufacturing was again performed using C.N.C. processes and the blades were machined from solid blocks of 7075 aluminum alloy. The area-averaged root-mean-square roughness height (as defined in equation 2.5) of the model airfoil was measured with a confocal laser microscope (Olympus LEXT OLS4000) and was found to be $S_q = 0.5 \pm 0.25$ microns.

Preliminary bench testing was performed external to the HRTF using the variable frequency motor on the test rig (described in section 2.4.2) to spin the turbine model and manually check for any mechanical vibrations. These were noted and subsequently avoided during testing of the model in the HRTF. This is reflected as gaps in tip speed ratio for specific data sets and model combinations. Often, the missing λ values were subsequently captured with a different p_s and U combination which achieved the same Reynolds number but at the desired tip speeds (by avoiding the

ω values which were known to cause issues). The process of repeating data sets at various pressure and velocity combinations to achieve the same Reynolds number as a data validation tool is detailed in chapter 4. The complete experiment setup is shown in figure 2.14.

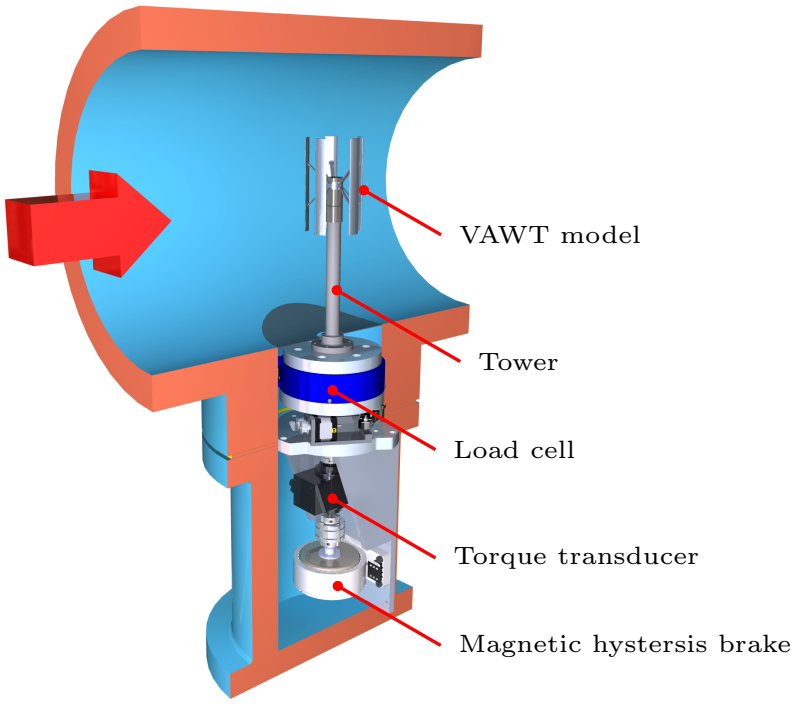

Figure 2.14: Computer rendering of the $N_b = 5$ blade model, tower, and measurement stack inside a cut-away of the HRTF test section. Flow direction is given by the red arrow.

In an effort to expand the experimental scope beyond the fixed 5-blade rotor case, several interchangeable hubs were produced such that the number of blades could be reduced to 4, 3, or 2. This allowed for quick variation of the turbine solidity. The different configurations are shown in figure 2.15. Similar to the 5 blade model, these reduced-solidity models were run on the test rig prior to insertion into the HRTF so as to characterize any drive-train frequencies which should be avoided during an experiment.

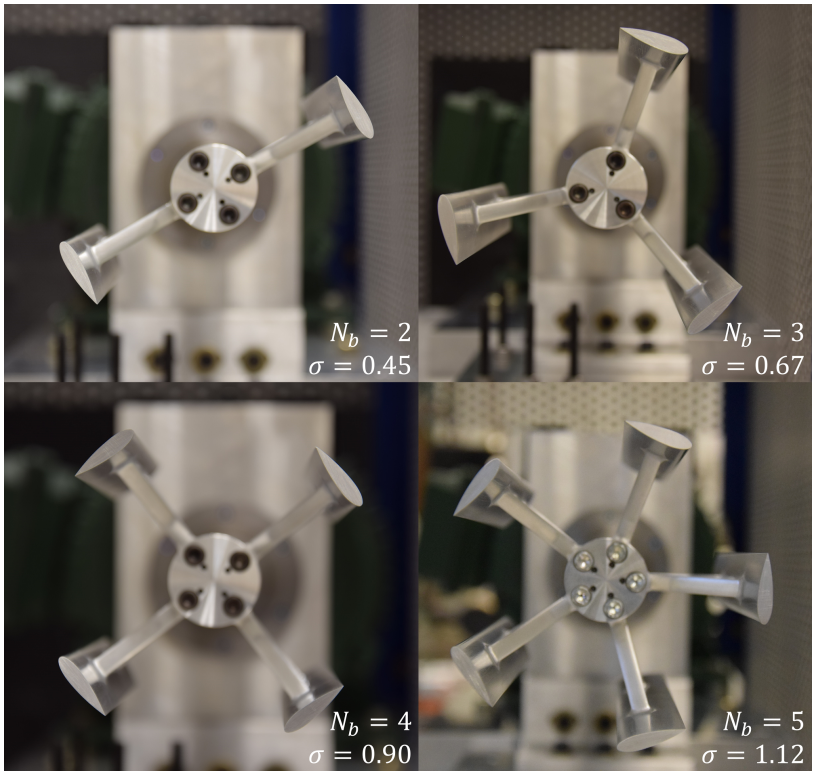

Figure 2.15: Various hub configurations for the VAWT which allowed for altering the solidity by using 2, 3, 4, or 5 blades.

2.6 Measurement Procedure

The experimental methodology was the same for both the VAWT and HAWT models in the HRTF. A value of the Reynolds number based on the diameter, Re_D, was chosen and a range of static pressure and velocity combinations calculated which would produce this value. Depending on the goal of the experiment, a single p_s would be chosen as the target pressure. The process to pressurize the HRTF would then begin, which takes several hours due to the large volume and high pressure air required. Once the target pressure was achieved, the HRTF was allowed to stabilize for approximately thirty minutes and come to an internal equilibrium temperature. Then the value of p_s was measured and the tunnel velocity calculated which would produce the originally desired Re_D. Slight differences in the target versus final tunnel pressure were accounted for by small changes in the run velocity to most closely match

the target Re_D. The first step of the experiment was a test run, performed at the set velocity to determine model behavior. Free-stream velocity was slowly increased and the model (either HAWT or VAWT) was allowed to self-start, completely unassisted, and reach the maximum rotational speed (free-spin condition). A range of braking loads were then applied to control model rotational speed (i.e., the tip speed ratio) and recorded for use during the actual experiment. Before and after a run, zero-measurements of the all instrumentation were made and used in post-processing to reduce measurement uncertainty. The data acquisition phase could then begin where the tunnel velocity was set and the range of previously acquired braking loads were applied in succession to generate an entire power curve. Data was acquired for a fixed number of rotations, instead of a fixed time-frame, because the turbine operation is a stationary, periodic process. Post-processing involved the use of 300 rotations for determination of all calculated values. Corrections were also applied to the HAWT in post-processing which included accounting for the gearbox efficiency using the method of section 2.4.2 and a correction for blockage using the method outlined by Bahaj et al. (2007). Operation of the model turbine was different than how field-scale wind turbines are controlled. In the field, rotation rate is nominally fixed and Re_D varies due to changes in the inflow conditions. This has the unfortunate consequence of changing both λ and Re_D simultaneously. For these experiments the model was operated at constant Re_D for an entire test, while ω, and hence λ, were varied.

2.7 Tower Drag Effects

The axial thrust force is measured at the base of the turbine and therefore the reported thrust coefficient values include the axial force of the turbine plus drag due to the tower assembly. The magnitude of this effect can be observed by assuming the thrust

force due to the turbine and the drag force from the tower are linear so that $F_t = F_{\text{turbine}} + F_{\text{tower}}$, then the measured thrust force can be written:

$$C_t = \frac{F_{\text{turbine}} + F_{\text{tower}}}{\frac{1}{2}\rho U^2 A_{\text{rotor}}} = C_{t,\text{turbine}} + C_{d,\text{tower}} \frac{A_{\text{tower}}}{A_{\text{turbine}}} \tag{2.10}$$

where $C_{d,\text{tower}}$ is the drag coefficient of the tower geometry and A_{tower} is the respective frontal area of the tower which characterizes this drag. For a cylinder at moderate Reynolds numbers, the value of the tower drag coefficient could be as high as 0.5, but will decrease as Re of the tower increases as is the case for the circular VAWT tower geometry. The drag coefficient may be much lower for a tower with a more aerodynamic profile, such as that used for the HAWT. For these experiments the drag coefficient as a function of Reynolds number was not measured directly for either tower geometry, but estimates of their effect can be made using equation 2.10 and assumed values for C_d. For the total tower frontal area of each turbine:

$$\left.\frac{A_{\text{tower}}}{A_{\text{turbine}}}\right|_{\text{V.A.W.T.}} = 0.414 \tag{2.11}$$

$$\left.\frac{A_{\text{tower}}}{A_{\text{turbine}}}\right|_{\text{H.A.W.T.}} = 0.161 \tag{2.12}$$

$$\tag{2.13}$$

If a worst-case value of $C_{d,\text{tower}}|_{\text{V.A.W.T.}} = 0.5$ is assumed for the vertical axis wind turbine tower then the additional increase in the measured drag coefficient is 0.207. For the horizontal axis model, the case is a bit better because a lower value of $C_{d,tower}|_{\text{H.A.W.T.}} = 0.1$ could be used which gives a relatively small increase of 0.0161 to the drag coefficient. In either case, a correction for tower drag was not made to any the reported thrust coefficient values for several reasons. The first is that the specific value of $C_{d,\text{tower}}$ is in reality very difficult to separate from $C_{t,\text{turbine}}$ because

the two interact in a complicated fashion. The above discussion assumed a single velocity scale could be used to find the drag for the tower, but a significant portion of the tower is inside the wake of the rotor (for both HAWT and VAWT), meaning that the resulting drag force could be much less than expected. Therefore any corrections applied to the thrust coefficient would need to make a number of assumptions about the way drag varies across the tower and also with Reynolds number. Ideally, wake measurements or an alternate method of measuring the thrust force closer to the turbine could be employed, but these are not feasible with the current setup.

2.8 Measurement Uncertainty Analysis

The following details the uncertainty analysis of each sensor used in the measurement process and propagates the uncertainty through to the final measurements of interest, namely λ, Re, C_p, and C_t. Errors can enter the measured data points via two distinct sources, the first of which is the so-called zero reading. These measurements are performed prior to an experimental run and consist of reading the voltage of each sensor with nominally zero external excitation. In a typical fluid mechanics experiment, the velocity is set to zero and the system is allowed to settle into an equilibrium state. Each sensor has some offset voltage from reference ground (where the calibration was performed), and these voltage values are then recorded for use in post-processing. Uncertainties associated with these offsets (although typically very small) are included in the following analysis. The second source of errors are the measurements made during the experiment, and the associated uncertainties are straightforward to calculate.

In the case of wind turbine models, it is expected that during an experiment the sensor readings will fluctuate in time due to the unsteady operation of the model. These forces and moments are periodic with the rotation rate and therefore will con-

verge to a mean value given sufficient sampling throughout an individual rotation and the acquisition of a sufficient number of rotations. In these experiments, it was made standard practice to average over 300 rotations so as to converge the means and higher-order moments of interest. For the uncertainty analysis, error sources primarily arise from both systematic and random sources. Systematic error sources may be quantified by either careful calibration of the sensor or by using the manufacturer provided data sheets. Random sources are typically more subjective and may be caused by several factors which can be captured in a bulk measurement such as the standard deviation of a signal. For these measurements, random error sources were not included in the uncertainty analysis. During a wind turbine experiment, using either HAWT or VAWT geometries, the input signal is not purely statistically stationary but is instead a stationary, periodic signal. Therefore a simple standard deviation calculated from the time series would not accurately capture only the random fluctuations in the measurement signal. Much of the fluctuation around the mean is therefore actual wind turbine loading, and not random at all. Furthermore the exact shape of this signal is not known a-priori to performing an experiment, so a phase-averaged method whereby the "true" signal is subtracted at each phase angle to determine the random fluctuations is also not feasible. As shown in the data validation of sections 3.1, 3.3.2, and 4.1; not including random uncertainties still resulted in conservative error bars as excellent collapse is seen for all experimental data sets.

2.8.1 Methodology

The systematic uncertainties are first listed for each source and then combined in a root-mean-square sense as the total uncertainty for each measured variable.

$$B_{x_i} = \sqrt{(B_1)_{x_i}^2 + (B_2)_{x_i}^2 + ... + (B_N)_{x_i}^2} \tag{2.14}$$

where the x_i indicates the individual sources for each sensor from 1 to N. If the uncertainty of a single sensor is desired, the analysis is complete. However, it is often the case that individual sensors act only as inputs to the parameter of interest. Therefore the individual uncertainties must be propagated to a result-level uncertainty, u_R, which may be found by taking the total uncertainty (also known as the sensitivity) for each input variable and using the following:

$$u_R = \left(\sum_{i=1}^{L} \left[\frac{\partial R}{\partial x_i} B_{x_i} \right]^2 \right)^{1/2} \tag{2.15}$$

where L is the number of elemental uncertainties (x_i's) and cross-correlations have been assumed negligible in this analysis. The final u_R is known as the result-level uncertainty for a particular measurement. Determination of the individual $(B_N)_{x_i}$ terms used in equation 2.14 are described in the following along with how these sensitivities propagate to the result-level uncertainty via equation 2.15.

2.8.2 Sensor Uncertainty Quantification

This section covers the various sensors used in both the HAWT and VAWT measurement campaigns.

Data Acquisition System

Small measurement uncertainties exist when converting analog voltages to digital signals. These are captured by the quantization error and are applied to each sensor uncertainty individually. Both data acquisition cards used for these experiments are $M = 16$ bit units, meaning that a range of $2^{16} = 66,536$ bit values are available to represent a given voltage range. Most sensors operated at full-scale voltages of $V_{\text{full-scale voltage}} = \pm 10$ or ± 5 (Volts) and these ranges are taken into account when determining the quantization error, which is typically small, around 150 micro-Volts.

Table 2.4: Systematic uncertainty source for the data acquisition system

Source	Symbol	Value
Quantization error	$(B_1)_{\text{D.A.Q.}}$	$V_{\text{full-scale voltage}}/2^M$

Torque Measurement

The Magtrol TM-308 (20 Nm) and TM-305 (2 Nm) torque transducers used in these experiments have the following manufacturer-listed uncertainties as given in table 2.5.

Table 2.5: Systematic uncertainty sources for torque transducers

Source	Symbol	Value
Linearity and Hysteresis	$(B_1)_T$	$\pm 0.1\%$ of rated torque
Temperature influence on zero	$(B_2)_Z$	$\pm 0.1\%$ of rated torque / (10 Kelvin)
Speed influence on zero	$(B_3)_Z$	$\pm 0.01\%$ of rated torque / (1000 r.p.m.)

Torque measurements are made with reference to a zeroed mean value, which accounts for any slight voltage offsets in the sensor by measuring the output with zero input loading (this measurement is denoted as τ_0). Then the mean value measured during an experiment ($\overline{\tau}$) subtracts this to find the true value:

$$\tau = \overline{\tau} - \tau_0 \tag{2.16}$$

Zeroing out a sensor in this fashion is commonly done to eliminate any systematic uncertainty from so-called "zero drift". Manufacturers vary as to whether they account for this in the supplied calibration or data sheet. Due to this, it has been included here so as to provide a conservative yet realistic estimate of the uncertainties. Factory calibration for the two torque sensors is for ranges of 20 (Nm) and 2 (Nm), each over a 5 (V) span. The 2 (Nm) sensor is mounted on the measurement stack and acquired the actual experimental data, while the second transducer was mounted to the test rig. The ranges are used to find the variable uncertainty, B_{x_i} using equation 2.14 along with the values in table 2.5. The form of equation 2.16 means that

the result-level uncertainty for the torque measurement is very straightforward using equation 2.15 so that the final uncertainty becomes (with all terms written out):

$$u_\tau = \left[\left(\frac{\partial\tau}{\partial\overline{\tau}}B_{\overline{\tau}}\right)^2 + \left(\frac{\partial\tau}{\partial\tau_0}B_{\tau_0}\right)^2\right]^{\frac{1}{2}} \tag{2.17}$$

$$= \left[((B_1)_{D.A.Q.})_T^2 + (B_1)_T^2 + ((B_1)_{D.A.Q.})_Z^2 + (B_2)_Z^2 + (B_3)_Z^2\right]^{\frac{1}{2}} \tag{2.18}$$

where the subscript T indicates the mean data point of interest and Z is the zero reading. This form is common for any data which is digitized by the D.A.Q. and has a zero-value which is subtracted from the mean in post-processing. For the remainder of this analysis in this section, only the B_{x_i} terms are given, and a digitization uncertainty is always assumed present.

Speed Measurement

The Magtrol TM-305/308 torque transducers are equipped with an optical encoder output for determination of the rotational speed. It consists of 60 evenly-spaced holes on an optical encoder wheel attached to the spinning shaft and located inside the sensor. A square wave pulse-train is the output which can be simply converted to rotations per minute via:

$$\frac{1 \text{ pulse}}{(\Delta t)_{\text{rising edges}} \text{ (seconds)}} \times \frac{1 \text{ rotation}}{60 \text{ pulses}} \times \frac{60 \text{ (seconds)}}{1 \text{ minute}} = X\frac{\text{rotations}}{\text{minute}} \tag{2.19}$$

requiring only the time-step between subsequent pulses, as Δt, to determine the X number of rotations per minute. Since the fastest the setup can currently operate is 6,000 (r.p.m.), this gives a maximum frequency of rotation of 628 (Hz.), which means a pulse frequency of $37,680$ (Hz.). By the Nyquist theorem, the minimum acquisition

frequency is twice this value to accurately measure the frequency of the square waves (where $\Delta t = 1/f$) without aliasing the signal. All acquisitions were done at 80 (kHz.) or at least twice the highest pulse frequency via an analog input and the data was post-processed to determine the rotational speed for each data point. Therefore only a small error is expected with the rotational measurements as given in the following table:

Table 2.6: Systematic uncertainty source for the rotational speed encoder

Source	Symbol	Value
Rotational encoder	$(B_1)_{\text{speed}}$	± 1 (r.p.m.)

Density and Viscosity Measurement

The air density and viscosity inside the HRTF were determined by the methods outlined by Zagarola (1996). Density was calculated using real-gas relationships (see equation 2.2) while the dynamic viscosity of air was found via a combination of empirical curve fits. The current setup to measure T_a and P_a is nearly identical to the one used by Zagarola (1996), and therefore the uncertainty in both ρ and μ is the same as those experiments and is given in table 2.7. Also included are the uncertainty values given for temperature and static pressure measurements .

Table 2.7: Result-level uncertainties for fluid properties

Quantity	Symbol	Value
Temperature	u_T	± 0.15 (K)
Static Pressure	u_{p_s}	$\pm 1.0\%$
Density	u_ρ	$\pm 0.36\%$
Dynamic viscosity	u_μ	$\pm 0.8\%$

Velocity Measurement

Mean velocities are measured in the HRTF via a Pitot-static tube connected to a differential pressure sensor located inside the wind tunnel. The range of the differen-

tial input Validyne DP-15 pressure transducers is ±13.79 (kPa) or ±2 (p.s.i.). This sensor has a replaceable sensing diaphragm which requires calibration before being used in the wind tunnel. This was performed with a dead-weight tester (Ametek model number RK-300SS) which has a stated accuracy of ±0.025% of the reading. The procedure for calibrating the sensors involved taking 18 readings of sensor output while increasing the applied differential pressure to the sensor, followed by 10 readings taken while decreasing the applied pressure. The slope was calculated for decreasing and increasing applied pressures, in units of output volts per applied p.s.i., and then compared as an estimate of the linearity and hysteresis of the sensor. It was always the case that this value was larger than the Ametek calibrator accuracy, so it was taken as the primary uncertainty source for the differential pressure sensors. The final uncertainty value found via this calibration procedure is given in table 2.8. This value is lower than the standard, manufacturer listed value for the differential pressure sensors of $(B_1)_{ps} = \pm 0.25\%$, probably owing to a conservative approach by Validyne.

Table 2.8: Systematic uncertainty source found via calibration for the free-stream differential pressure sensor.

Source	Symbol	Value
Linearity/hysteresis/repeatability	$(B_1)_{ps}$	$\pm 0.1843\% FS$

Due to the differential nature of the measurements, notation of the pressure transducers is given as Δp. In the same way as the torque sensors, the pressure transducers must be zeroed before each measurement, by subtracting the zero reading (p_0) from the mean ($\overline{p}$).

$$\Delta p = \Delta \overline{p} - \Delta p_0 \tag{2.20}$$

For both the traverse and free-stream velocity measurements, the pitot-tube was well-aligned with the incoming flow at ±1° (Jiménez et al., 2000), and therefore did

not contribute significantly to the measurement error. Dynamic pressure as measured by a Pitot-static tube is converted to velocity via:

$$U = \left(\frac{2\Delta p}{\rho}\right)^{\frac{1}{2}} \tag{2.21}$$

and the final uncertainty in the measured velocity values is then:

$$u_U = \pm \left[\frac{1}{2\rho\Delta p} u_{\Delta p}^2 + \frac{\Delta p}{2\rho^3} u_\rho^2\right]^{\frac{1}{2}} \tag{2.22}$$

Force and Moment Measurements

The forces generated are measured using a load cell manufactured by JR3 Incorporated (model number 75E20A4) with a nominal ±1000 (N) range for F_x and F_y while the range in F_z is slightly higher at ±2000 (N). The sensor also measures all three moments M_x, M_y, and M_z within a range of ±200 (Nm). System accuracies as given by the manufacturer are shown in table 2.9. Note that a decoupling matrix is used to separate the output voltages from the sensor into six components. The way the sensor is manufactured, all the channels are mechanically coupled inside the sensor body, which results in a cross-correlation factor between channels. The sensor is designed in a clever way such that the decoupling matrix turns out to be diagonally dominant, with at least an order of magnitude separating the diagonal terms from other terms in the same row. Therefore cross-correlations can safely be assumed negligible for the uncertainty analysis. A final note, although the nominal sensor accuracy is listed at ±2.5 (N) for F_x and F_y, it has generally been found to be much more accurate, possibly below ±0.5 (N), although this cannot be verified since an in-situ calibration system is not available in the lab. For these reasons, the manufacturer supplied accuracies are used in the following analysis.

Similar to other measurements, the force sensor is zeroed before each experimental run so that only the applied aerodynamic loads are recorded. The resulting values may

Table 2.9: Systematic uncertainty sources for forces and moments

Quantity	Symbol	Value
Nominal accuracy in x and y	$(B_1)_{F_{x,y}}$	$\pm$2.5 (N)
Nom. accuracy in z	$(B_1)_{F_z}$	$\pm$5.0 (N)
Nom. moment accuracy (x, y, and z)	$(B_1)_{M_{x,y,z}}$	$\pm$0.5 (Nm)

be used as input to equation 2.14 to find the result-level uncertainty (equation 2.15) in the force measurement.

2.8.3 Propagation of Sensor Uncertainties

This section covers the propagation of uncertainties from the various sensors to the final, result-level uncertainties of the measured quantities of interest.

Gearbox Efficiency Uncertainty

The measurement of the gearbox efficiency as performed with the test rig is given by equation 2.6. The second torque transducer used to measure input power has the effect of increasing the overall measurement uncertainty. Although this effect is still much smaller than simply not knowing the power lost in the gearbox. For brevity, the values measured before entering the gearbox are denoted with a subscript "in" while output values are denoted with "out". The final gearbox efficiency uncertainty value is given by:

$$u_\varepsilon = \left[\left(\frac{(\tau\omega)_{\text{out}}}{(\tau^2\omega)_{\text{in}}} u_{\tau_{\text{in}}} \right)^2 + \left(\frac{(\tau\omega)_{\text{out}}}{(\tau\omega^2)_{\text{in}}} u_{\omega_{\text{in}}} \right)^2 + \left(\frac{\omega_{\text{out}}}{(\tau\omega)_{\text{in}}} u_{\tau_{\text{out}}} \right)^2 + \left(\frac{\tau_{\text{out}}}{(\tau\omega)_{\text{in}}} u_{\omega_{\text{out}}} \right)^2 \right]^{\frac{1}{2}} \quad (2.23)$$

Tip Speed Ratio Uncertainty

The tip speed ratio is a function of several variables, and thus the uncertainty analysis must follow the form of equation 2.15. The simplicity of this method is that it can be repeated a number of times where the uncertainty of a new parameter is calculated using information from known constituent values. The tip speed ratio makes use of the previously calculated uncertainties in free-stream velocity and angular rotation rate.

$$u_\lambda = \left[\left(\frac{\omega R}{U^2} u_U \right)^2 + \left(\frac{R}{U} u_\omega \right)^2 \right]^{\frac{1}{2}} \tag{2.24}$$

Reynolds Number Uncertainty

In a similar fashion to the tip speed ratio, the uncertainty associated with the Reynolds number based on rotor diameter is straightforward to calculate:

$$u_{Re_D} = \left[\left(\frac{\rho D}{\mu} u_U \right)^2 + \left(\frac{DU}{\mu} u_\rho \right)^2 + \left(\frac{\rho DU}{\mu^2} u_\mu \right)^2 \right]^{\frac{1}{2}} \tag{2.25}$$

Power Coefficient Uncertainty

The power coefficient is defined by:

$$C_p = \frac{P_{\text{in}}}{\frac{1}{2}\rho U^3 A} = \frac{\varepsilon(\tau\omega)_{\text{out}}}{\frac{1}{2}\rho U^3 A} \tag{2.26}$$

where A is the rotor swept area. As with the previous analysis, the uncertainty in C_p is found by propagating the errors of each individual variable.

$$u_{C_p} = \pm \left[\left(\frac{\partial C_p}{\partial \tau_{\text{in}}} u_{\tau_{\text{in}}} \right)^2 + \left(\frac{\partial C_p}{\partial \omega_{\text{in}}} u_{\omega_{\text{in}}} \right)^2 + \left(\frac{\partial C_p}{\partial \varepsilon} u_{\varepsilon} \right)^2 + \left(\frac{\partial C_p}{\partial \rho} u_{\rho} \right)^2 + \left(\frac{\partial C_p}{\partial U} u_U \right)^2 \right]^{\frac{1}{2}} \quad (2.27)$$

and the sensitivity for each variable is found as:

$$\frac{\partial C_p}{\partial \tau_{\text{in}}} = \frac{2\varepsilon\omega_{\text{out}}}{\rho U^3 A} \quad (2.28)$$

$$\frac{\partial C_p}{\partial \omega_{\text{in}}} = \frac{2\varepsilon\tau_{\text{out}}}{\rho U^3 A} \quad (2.29)$$

$$\frac{\partial C_p}{\partial \varepsilon} = \frac{2(\tau\omega)_{\text{out}}}{\rho U^3 A} \quad (2.30)$$

$$\frac{\partial C_p}{\partial \rho} = \frac{-2\varepsilon(\tau\omega)_{\text{out}}}{\rho^2 U^3 A} \quad (2.31)$$

$$\frac{\partial C_p}{\partial U_\infty} = \frac{-6\varepsilon(\tau\omega)_{\text{out}}}{\rho U^4 A} \quad (2.32)$$

The velocity cubed in the denominator of C_p causes the final uncertainty to be relatively sensitive to velocity errors, particularly at low velocity values, as denoted by the factor of 6 which pops out of the partial derivative. However, the uncertainty could also be written in terms of the dynamic pressure and density instead using equation 2.21 where the sensitivity term then only relies on measured pressure to the 5/2 power and the coefficient is near unity:

$$\frac{\partial C_p}{\partial(\Delta p)} = \frac{-3}{2\sqrt{2}} \frac{\varepsilon(\tau\omega)_{\text{out}}\sqrt{\rho}}{A(\Delta p)^{5/2}} \quad (2.33)$$

In this case the sensitivity to density errors would also need to be re-calculated.

Thrust Coefficient Uncertainty

In a similar manner to the power coefficient, the uncertainty can be propagated through the thrust coefficient. For the current setup, the sensor x axis is aligned with the stream-wise direction and thus reports the thrust force, F_t. The sensitivities are as follows:

$$\frac{\partial C_t}{\partial F_t} = \frac{2}{\rho U^2 A} \tag{2.34}$$

$$\frac{\partial C_t}{\partial \rho} = \frac{-2F_t}{\rho^2 U^2 A} \tag{2.35}$$

$$\frac{\partial C_t}{\partial U} = \frac{-4F_t}{\rho U^3 A} \tag{2.36}$$

Again, inserting these into equation 2.15 gives the final uncertainty in the thrust measurements.

$$u_{C_t} = \pm \left[\left(\frac{\partial C_t}{\partial F_t} u_{F_t} \right)^2 + \left(\frac{\partial C_t}{\partial \rho} u_\rho \right)^2 + \left(\frac{\partial C_t}{\partial U} u_U \right)^2 \right]^{\frac{1}{2}} \tag{2.37}$$

Chapter 3

Horizontal Axis Wind Turbine Model at High Reynolds Number

In this chapter Reynolds number effects on the performance of a HAWT model are explored in depth. The experiments in this section are the first of their kind in which a small-scale model is tested with Reynolds number, tip speed ratio, and Mach numbers matched to full-scale values. Inflow has been restricted to the canonical case, which is laminar (with a relatively low turbulence level, as noted in chapter 2). This differentiates these experiments from field measurements where effects such as turbulence and sheared inflow as found in the atmospheric boundary layer are typically present. Studying the canonical case enables deduction of the underlying flow physics and makes replicating these experiments for both experimental and numerical simulation much more straightforward.

3.1 Experimental Data Validation

Using a pressurized wind tunnel gives the unique ability of matching the non-dimensional parameters in multiple ways. Tunnel pressure becomes an independent parameter, or extra knob, available to the experimentalist. Thus the velocity and

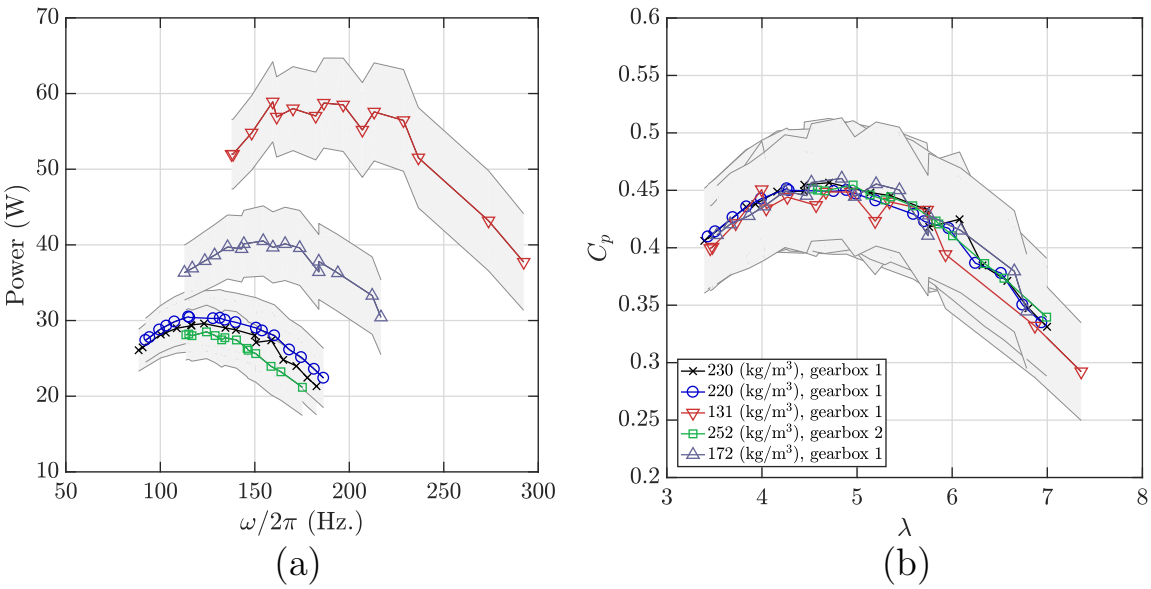

Figure 3.1: Dimensional plots in (a) show measured power versus the rotational frequency at a matched Reynolds number of $Re_D = 5.1 \times 10^6 \pm 34,000$. The plot to the right in (b) shows the same data non-dimensionalized by the free-stream conditions. Legend applies to both plots.

flow density can be set independently from one another, allowing a single Reynolds number to be achieved with various combinations of physical variables. Utilizing this capability means that a data set acquired at some Re_D value can be repeated at a different combination of ρ and U (but the same Reynolds number) in order to validate the data set. Model rotation rate is also altered via the velocity term in λ, this being another advantage when certain rotational rates are to be avoided. This was used extensively with the VAWT data of chapter 4, but drive-train frequencies were less of an issue for the HAWT model. An example of using multiple tunnel conditions to achieve a single Re_D value is given in figure 3.1 for $Re_D = 5.1 \times 10^6 \pm 32,310$. Here the bounds indicate the maximum deviation from the mean Reynolds number of any data set (due to slight variations in tunnel conditions from run-to-run, Re_D cannot be specified exactly). Corrections have been applied to all HAWT data sets for both gearbox losses and blockage effects (see section 2.4.2 for details of the gearbox correction and the work of Bahaj et al. (2007) for the blockage correction methodology) with the measurement uncertainty given by the shaded bars. The

uncertainty values have been calculated using the methodology of section 2.8. The plots of figure 3.1 (a) show a range of tunnel densities and data sets acquired with two different gearboxes. Figure 3.1 (b) shows the exact same data, but recast into the non-dimensional forms of power coefficient versus the tip speed ratio. Despite the differences in density, free-stream velocity, measured power, rotational speed, and even the gearbox used; the curves all collapse well within the experimental uncertainty. Between the highest density case (252 kg/m^3) and the lowest density case (131 kg/m^3) the input power level has doubled, yet collapse in C_p is clearly evident. Furthermore, rotational speeds are also quite disparate between these two data sets. Comparing the cases acquired with gearbox 1 to the data set of gearbox 2, no discernible difference is observed in the collapse region lending direct support to the gearbox correction methodology of section 2.4.2. The efficiencies for gearbox 1 and 2 were measured in separate sets of test rig measurements and new fitting parameters for ε were found. Despite these changes, the collapse is not disrupted. These plots highlight the utility of having an extra experimental "knob" available, and can drastically increase the confidence level for a given data set.

To ensure all experimental data was well-validated, this methodology was applied to a number of different Reynolds numbers: $Re_D = 7 \times 10^6$, 10×10^6, and 12×10^6. Separate gearboxes were used when feasible to provide additional confidence in the correction methodology. Since gearboxes have a finite life-span, it was not possible to test every combination of Reynolds number, tunnel condition, and gearbox. The resulting non-dimensional power and thrust coefficients are shown in figure 3.2.

The left column of the figure gives the power coefficient and excellent collapse is seen across all Re_D for all tunnel conditions and gearbox combinations. In some cases small deviations in the curve are seen, but these are well within the calculated uncertainties. The reduction in overall error-bar size between the lowest and highest Re_D cases is due to the increased mechanical loads being measured, effectively in-

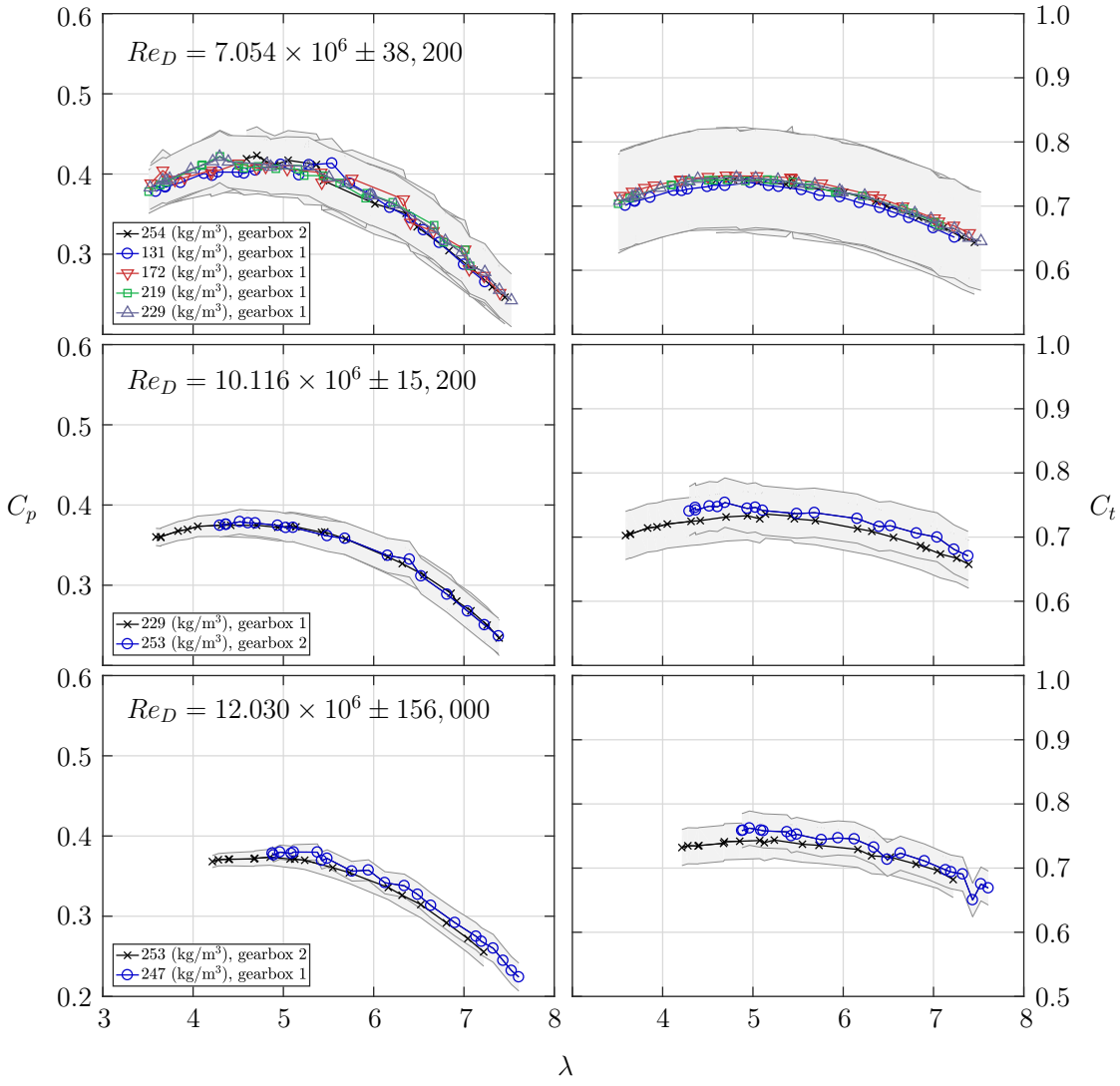

Figure 3.2: Power and thrust coefficient data validation for three different Reynolds numbers. Labels for the Reynolds number and the legends apply to each pair of horizontal plots.

creasing the signal to noise ratio of the data set. This means that experiments can be tailored to maximize the measurement equipment sensitivity by using large velocities at low densities. Another note regarding the gearbox correction is that no attempt was made to account for the axial thrust force imposed by the rotor during HRTF experiments as there was no means of applying this load to the gearbox while on the test rig. Despite this, the collapse for each power coefficient curve appears excellent, lending an additional level of confidence to the correction methodology since F_t also varies between these data sets. The right-most column of figure 3.2 gives the thrust coefficient as a function of tip speed ratio, which displays more scatter than the associated power coefficient. This is especially evident at higher Re_D values of 10×10^6 and 12×10^6 and is primarily due to the larger uncertainty associated with the load cell used in axial force measurements (details can be found in section 2.8). Note that the relative magnitude of the error bars for the thrust coefficient are higher than for the power coefficient at the same Re_D values.

3.2 Rotor Performance with Reynolds Number

The power and thrust coefficients for the smooth wind turbine model are shown in figure 3.3 (a) and (b) for a select range of Re_D values from 4 to 14 million. No clear trend with Reynolds number is evident in the thrust coefficients. There are two potential explanations for this result, the Re_D trend in C_t is small and apparently masked by the experimental uncertainty or there is no significant trend in Reynolds number. Further measurements with a higher resolution force sensor are necessary for additional insight. There is apparently a small dependence on the tip speed ratio for C_t, with this trend remaining more or less present for all Re_D values. In contrast, a clear Reynolds number dependency exists in the power coefficient results. Only a few power curves are shown for clarity (with the overall trend confirmed via a series of

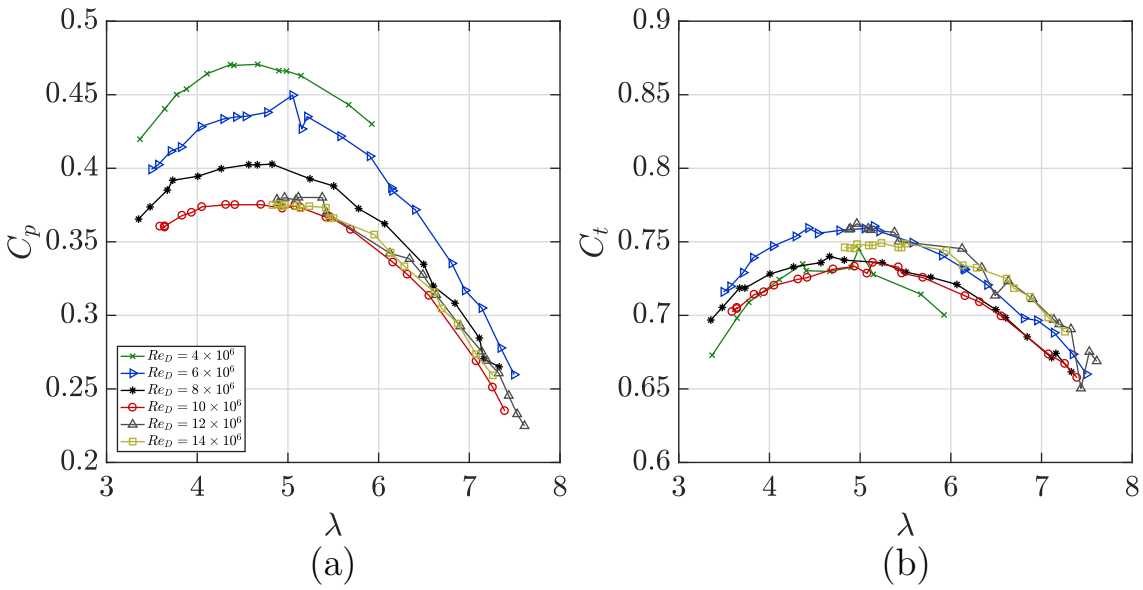

Figure 3.3: Trends for the HAWT model with scale effect for both the power coefficient in (a) and thrust coefficient in (b).

validation experiments as shown in section 3.1) for a number of Re_D values between 4 and 14 million. Surprisingly C_p is inversely related to Re_D, with a very strong dependence at the lower Reynolds number cases. As Re_D approaches 10 million, all Reynolds number dependence ceases and the curves begin to collapse. Power coefficients measured at larger values of λ appear to show Re invariance sooner than data acquired at lower tip speeds. This is evident when observing data at $\lambda = 7$ versus $\lambda = 5$, particularly for the $Re_D = 6 \times 10^6$ and 8×10^6 cases. This suggests that another non-dimensional parameter may better capture these trends. A combined parameter is proposed that represents a blade-level Reynolds number:

$$Re_c = \frac{\rho c \sqrt{U^2 + (\omega R)^2}}{\mu} = Re_D \frac{c}{D} \sqrt{1 + \lambda^2} \tag{3.1}$$

which combines outer flow variables with those most relevant to the near-blade physics. This definition uses an estimate of the velocity at the tip, $U_{rel} = \sqrt{U^2 + (\omega R)^2}$, to define the relevant velocity scale, while the length-scale chosen is the blade chord at the tip. The way in which Re_c is defined means it is the

maximum possible Reynolds number which could be encountered on the rotor. It is also conveniently found if λ, Re_D, and the tip chord to diameter ratio are known, making it possible to estimate for other experiments and field-scale turbines without resorting to simulations or models.

To evaluate the effectiveness of using equation 3.1 to capture Reynolds number trends, the experimental data was linearly interpolated to a specified grid of λ values. In general, data was not acquired at fixed values of the tip speed ratio, instead braking loads were specified which returned a range of λ, with twelve or more tip speeds typically acquired for each power curve (fixed Re_D value). Interpolation to a fixed grid allows us to keep one parameter constant when determining Re_c and evaluate the effect, otherwise only a disparate cloud of points will be returned due the spread of λ values. The power coefficient as a function of Re_c at fixed tip speeds is denoted by $C_p|_\lambda$ and is shown in figure 3.4 (a). This plot is equivalent to traveling vertically downward along the power curves of figure 3.3 (a) with λ fixed. There is apparently an initial decrease in C_p with Re_c followed by behavior which is invariant with additional Re_c increases. Note that no extrapolation was allowed outside the range of measured λ values and thus C_p is not available for all possible combinations of λ and Re_D. There are two reasons a turbine would not operate at some combinations of tip speed and Reynolds number. The first is related to the aerodynamics of the model. Since the rotor is completely driven by the flow, there are certain tip speeds which are not available for a given Re_D. For instance, if very low λ were requested the turbine would stall and come to a stop. At large λ the turbine is typically spinning with a very light load and any further decrease in the brake load would result in the free-spin condition which produces no measurable power. The second reason a given Re_c may be unavailable is due to mechanical limitations of the drive-train which did not permit the very high loadings present at large Reynolds numbers.

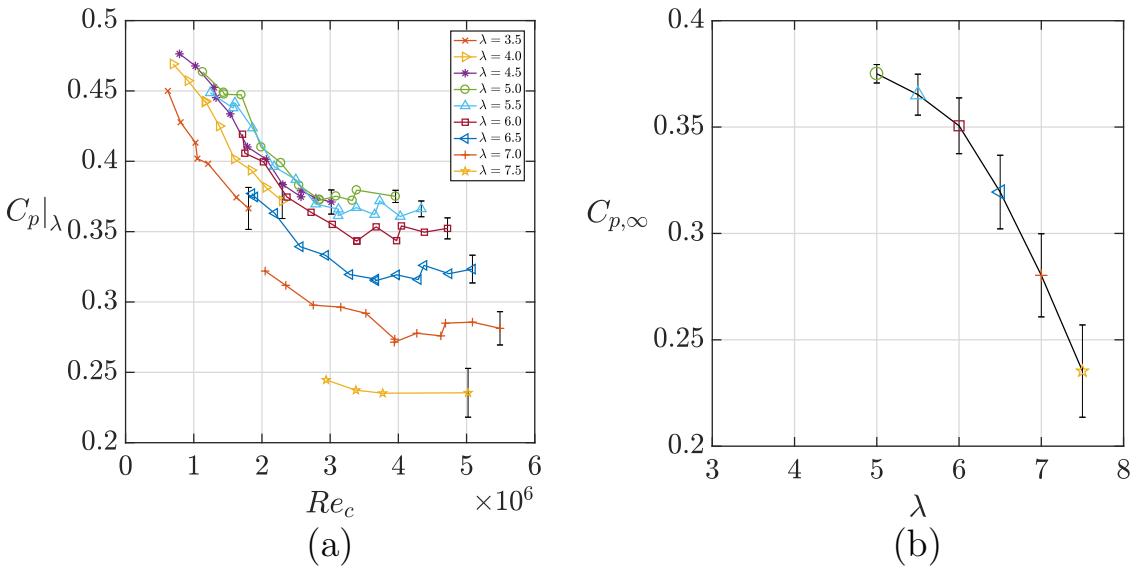

Figure 3.4: HAWT power coefficient as a function of the blade Reynolds number for a variety of tip speed ratios is shown in (a). The second plot in (b) gives the Reynolds invariant power curve, which is the mean value of C_p from (a) for all cases where $Re_c \geq 3.5 \times 10^6$. Representative error bars are shown at the highest Re_c value for each λ.

Using the data of figure 3.4 (a) as a guide, a threshold value of Re_c can be selected to define the invariant behavior. From inspection, a value of $Re_c \geq 3.5 \times 10^6$ has been chosen, making it straightforward to determine the value of the Reynolds invariant power coefficient, denoted as $C_{p,\infty}$. This quantity is defined as the arithmetic mean of all $C_p|_\lambda$ values for which $Re_c \geq 3.5 \times 10^6$, which was done to smooth some of the scatter present in the experimental data set.

Defining the Reynolds invariant power coefficient in this way allowed for determination of the invariant power curve as a function of tip speed ratio. The resulting curve is shown in figure 3.4 (b). This curve represents the power coefficient of any turbine operating under dynamic similarity to the one in these experiments for which $Re_c \geq 3.5 \times 10^6$. Observing that not all tip speeds are available, it cannot be definitively determined if $\lambda = 5.0$ is the peak in $C_{p,\infty}$. However, from inspection of the trends in figure 3.3 (b) the lower $\lambda = 4.5$, 4.0, and 3.5 appear unlikely to eclipse 5.0 as the optimal operating point. The main advantage of the invariant behavior is that

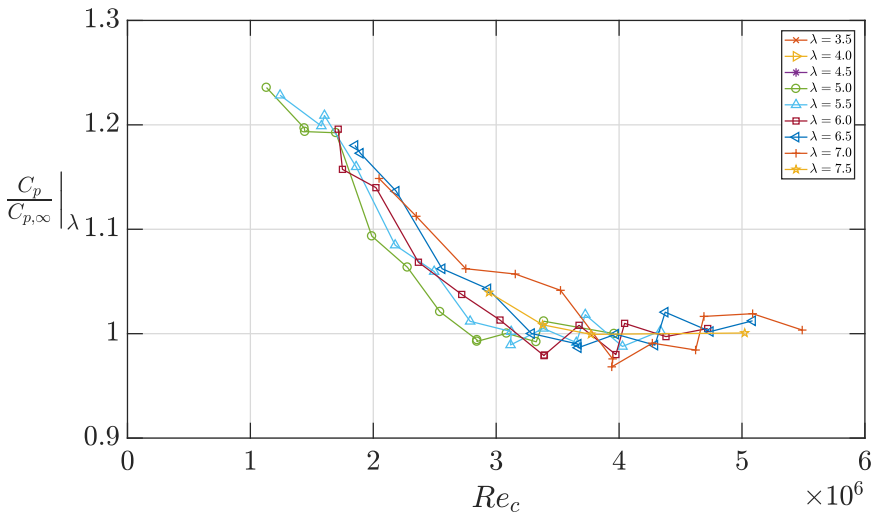

Figure 3.5: Power coefficient values at specified tip speed ratios normalized by their respective Reynolds invariant value (when $Re_c \geq 3.5 \times 10^6$).

these results can be extended to turbines of any size, provided the cutoff Re_c value is met or exceeded. Reynolds invariant behavior of this type for such a wide range of Re values has never before been shown for horizontal axis wind turbines. Full-scale units may operate at larger Re_c values, but for a relatively fixed rotational speed and with limited knowledge of the inflow properties. Thus an entire power curve as in figure 3.3 (b) is much more difficult to generate at the same confidence level or with well-controlled laminar inflow.

Further insight can be gained into the behavior of the power coefficient as it approaches the high Reynolds number limit by combining the results of figure 3.4 (a) and (b). For each tip speed, the curves of figure 3.4 (a) are normalized by the relevant $C_{p,\infty}|_\lambda$ value of figure 3.4 (b). The resulting plot is shown in figure 3.5. If the cutoff Re_c value has been chosen correctly, all curves will trend to unity with a minimum of over- or under-shooting behavior. Some scatter is expected due to the experimental uncertainty inherent to the measurements. In general, excellent collapse is seen across the various tip speed ratios. In particular, the behavior of the normalized curves when $Re_c < 3.5 \times 10^6$ gives a very similar shape. Implying that the rate of change of C_p at fixed λ only scales with the magnitude of the respective $C_{p,\infty}|_\lambda$ value. Thus if the

invariant power curve for a rotor is known, only a few additional, lower Re_c operating points are required to completely establish the rotor behavior with Reynolds number for all λ and Re_D conditions. This conclusion has powerful implications for modeling Reynolds number effects on horizontal axis wind turbines. It is expected that the shape of this curve will vary from turbine-to-turbine due to geometrical differences and the Reynolds number behavior of the specific airfoils. However, these experiments are the first to span a five-fold increase in Re_c values with matched λ and Ma. This method can straightforwardly characterize the Reynolds behavior of an entire wind turbine rotor, no matter the geometry, and even use it to correct data taken at lower Re to the invariant state.

3.3 Effects of Transition

During normal operation, a wind turbine in the field is likely to accumulate some form of surface roughness on the rotor blade. Surface irregularities can come from many sources such as sand, dust, insect debris, salt spray, ice, bio-fouling, manufacturing defects, and surface erosion. Turbine performance is directly impacted in a negative way, as recently discussed by Ehrmann et al. (2017). A significant performance degradation was observed for insect debris which caused up to a 25% loss in energy production and blade erosion a 20% loss while accounting for 6% of all wind turbine repairs. Thus increasing the current knowledge base of roughness effects on wind turbine operation could have direct impact on the current state of the art.

The elements making up the roughness are most densely located near the leading edge, since that is the primary point of contact for particles carried by the incoming wind. Furthermore, the roughness may be much larger than that required to transition the flow and therefore may affect the sectional airfoil performance in a different way than pure tripping devices as are typically applied to two-dimensional airfoil

sections. One of the most difficult aspects of turbine roughness studies is replicating the specific geometry causing the observed effects. To limit the scope, some authors have focused on one source of roughness such as insect debris as in Ramsay et al. (1996). In that work a mold was made of insect residue found on a field turbine and then used as the basis for a distributed roughness geometry which could be replicated on models. Even with the careful consideration given in this work, the model still only represents the particular roughness that was present on the field rotor that day. Extensive quantification of roughness using a large sample of actual turbine blades has not been undertaken, probably due to the extremely wide operating space of in-service units coupled with the difficultly of accessing the blade surface.

Given the high level of interest in roughness/transition effects, coupled with the complexity of matching field-scale roughness geometry, it was elected to pursue an airfoil-style, transition device on the HAWT model instead of replicating field-measured roughness. This allowed for studies focused on transition effects, a subset of roughness effects, and also required matching a much more narrow range of geometric details. The main effects of forcing transition on sectional airfoil performance is to reduce the lift slope and maximum C_l point while increasing drag (Braslow and Knox, 1958). The discussion of section 1.4.1 then leads us to surmise that the effect of forced transition is an overall decrease in performance of the wind turbine rotor. Furthermore, there has been some discussion in the literature about what the effect of transition is on the flow mechanics of the HAWT, specifically in reference to rotational augmentation. In section 1.4.3, the thesis of Guntur (2013) was mentioned as it describes the current range of hypotheses concerning the cause of rotational augmentation, with some authors positing that it is related to transition. This was another motivating reason to study transition-type as opposed to field-measured roughness as a way of gaining insight into the fundamental operation of the HAWT.

The following sections detail the addition of tripping devices to the HAWT model of section 2.4.1. The very high Reynolds numbers and small size of the model created a particular challenge in this regard, and a number of methods were experimented with before finding a workable solution for applying tripping devices in a repeatable manner. A number of experiments were performed with the tripped rotor, and comparisons are made with the smooth rotor power and thrust measurements. This is viewed as a first step into further investigations of transition effects on HAWT performance under the conditions of dynamic similarity with the full-scale.

3.3.1 Trip Geometry

Trip geometry can be specified in a number of ways, although the roughness height is generally considered to be the driving geometric feature which affects transition. Any method of trip geometry specification can only realistically be considered a first approximation, especially since the method of application may vary across different sources. The decision was made to employ the method of Braslow and Knox (1958) which allows for direct determination of the roughness height, k, via use of the critical roughness Reynolds number, Re_k, which is defined as the value directly above the roughness elements. Tripping devices were added to the suction and pressure side of all three rotor blades of the HAWT model with the goal of fixing the transition location on the airfoil sections. The critical trip height, k_{cr} as defined in Braslow and Knox (1958), was utilized to determine the geometric requirements on the roughness geometry. A roughness Reynolds number of $Re_k = 600$ was set as the minimum value, using the external velocity estimated along the rotor span via $U_{ext} = \sqrt{U^2 + (\omega r)^2}$ where U is the free-stream velocity and r the local radius for a given section. Determination of k_{cr} was performed at a fixed external tip speed of $\lambda = 5.0$ for simplicity and due to the fact that the maximum power coefficient of the smooth rotor resides around this value for most Reynolds numbers (see figure 3.3). Additionally, it was assumed

that the trips would be applied near 5% of the chord from the leading edge. The value of k_{cr} as determined by the method of Braslow and Knox (1958) as a function of radial location is given for a variety of representative Re_D values in figure 3.6.

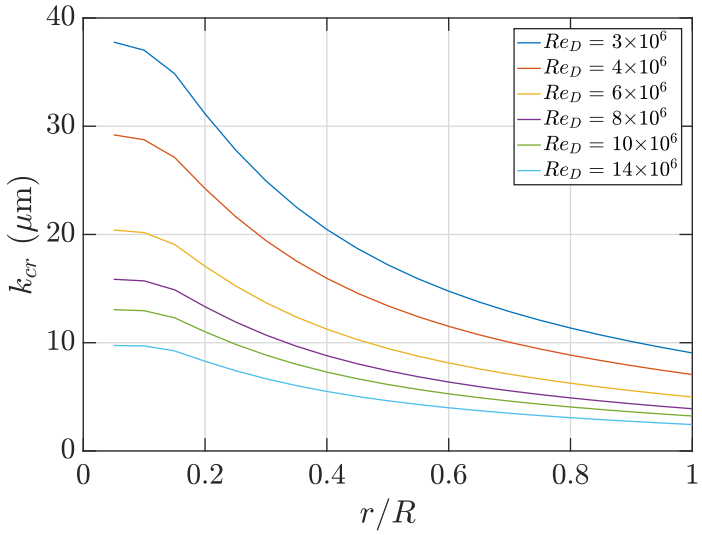

Figure 3.6: Critical roughness height on the HAWT model for $Re_k = 600$ as a function of radial location for various free-stream Reynolds numbers. Note that the external tip speed was fixed at $\lambda = 5.0$.

From this figure, it is clear that the ideal distribution of roughness element height would vary not only with radial location but also with the Reynolds number. Since this would create an impractical number of experiments, it was elected to choose a single target roughness height of $k_{cr} = 8$ to 10 (microns). This would allow for sufficient transition of the rotor at most of the moderate to high Re_D values, which are of most interest for scaling behavior.

Various methods were attempted to produce a reliable and repeatable tripping geometry of the scale desired. Traditional devices such as sand-grain grit, zig-zag tape, and trip wires could not be applied at sufficiently small scale to satisfy the requirements on k_{cr}. Some methods attempted were masked lines of paint along the rotor, silver-epoxy dots applied by hand, 10 micron diameter glass spheres applied to an adhesive-soaked rotor, and a variety of smeared epoxies using various individual brush bristles. Each of these methods was attempted on glass slides and imaged us-

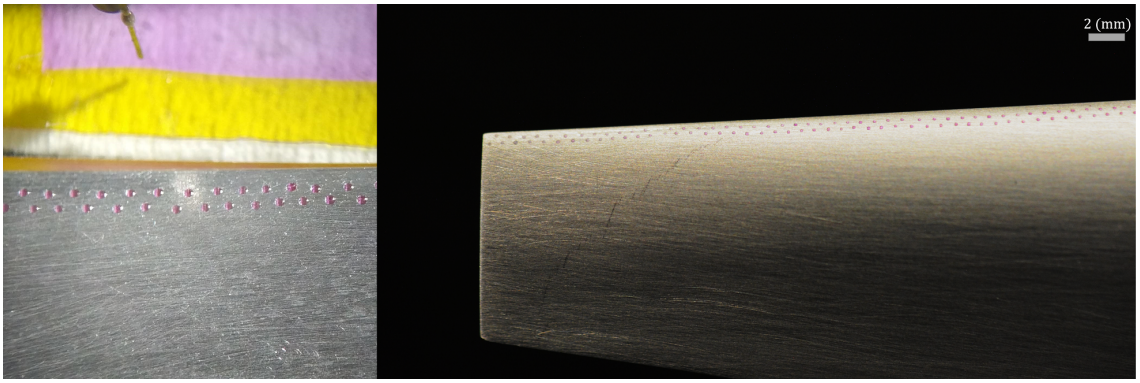

Figure 3.7: Left photograph shows application of tripping devices near the rotor leading edge. Epoxy reservoir is shown in top of frame as purple rectangle. Applicator needle is also shown in the top left. Right photograph shows finished rotor blade with trips applied.

ing a confocal microscope to determine the repeatability of the method and to asses how well the measured heights conformed to the desired value. The final methodology selected used an epoxy-bonding tool (West-Bond Incorporated model 7200A) to manually apply ultra-violet cured epoxy dots to the surface of the rotor. To create a reproducible dot size, a small section of wire with outside diameter of 180 (microns) was mounted inside a needle on the epoxy bonding tool and then dipped into a reservoir of U.V. cure epoxy (Norland Electronics Adhesive part number 123SBL). The reservoir of epoxy was created by removing a small square section of 25.4 micron thick Kapton tape with a razor blade, filling it with epoxy, and scraping the excess off the tape with the razor to create a constant-depth well. A micro-photograph of the dots as applied to the rotor is shown in figure 3.7.

Tripping devices were applied to both the suction and pressure side for all three blades of the rotor near the leading edge in two staggered rows. Due to the manual application process of the dots to a complex, three-dimensional rotor surface, the precise chord-wise location was subject to some variability but is estimated to be between 3% and 12% of the leading edge. The final trip geometry was carefully measured with a confocal microscope (Leica DCM 3D micro-optical system) at various

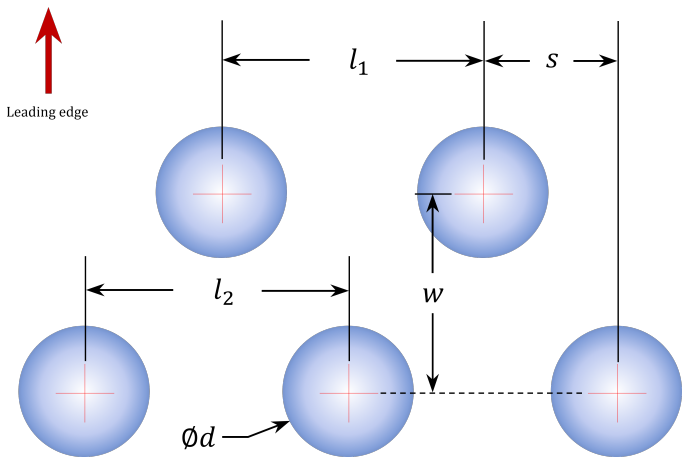

Figure 3.8: Schematic with labels showing measured dimensions for the applied micro-dot tripping devices. The highest point of each dot was taken as the center, denoted with a red cross.

Table 3.1: Measured roughness parameters for the applied tripping devices on the HAWT model rotor.

	Mean (μm)	Standard deviation (μm)
h_1	8.82	3.95
h_2	10.86	4.11
d	183.7	36.2
l_1	669.6	85.6
l_2	703.1	143.1
w	331.1	64.05
s	319.8	115.4

locations along the span and for both the pressure and suction side of several blades. The notation used for the measurements is represented schematically in figure 3.8, and the dot heights are given for row one and two as h_1 and h_2, respectively.

A number of parameters were measured using the confocal microscope so as to completely characterize the roughness parameters. Measurements were made on the pressure side of two blades (i.e. the sections facing into the oncoming free-stream flow) and the suction side of one blade. These results were combined to produce the statistics of table 3.1 and histograms of the height in figure 3.9 and the diameter in figure 3.10.

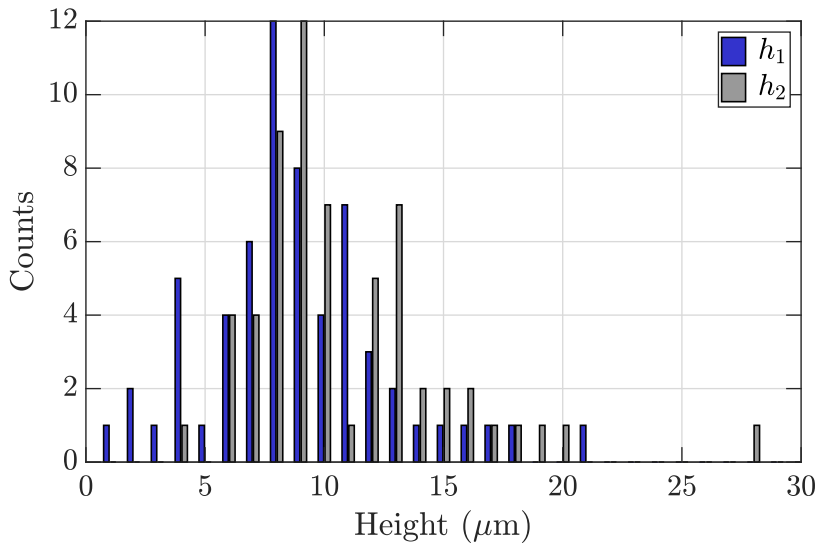

Figure 3.9: Histogram of measured trip device heights for the first and second row of the HAWT model, denoted l_1 and l_2.

The data of table 3.1 show that the dot size remained relatively consistent between rows, and the standard deviation indicates a fairly repeatable trip size given the manual application method. Perhaps most surprising is that the dot spacing, l_1 and l_2, remained relatively constant as this parameter was completely judged by eye. Note that the final dots have a large diameter to height aspect ratio meaning they are quite wide and flat. This varies significantly from the trip geometry of Braslow and Knox (1958) where sand-grain type roughness geometries were used. In that work the desired features were also much larger, making application and control of grain size relatively much easier.

The two histograms give an idea of the distribution of the heights and diameters of the dots. A good grouping is seen around 9 microns for both row 1 and 2 in figure 3.9, although the second row tends to skew toward taller dots. The dot diameter distribution of figure 3.10 gives a much larger range of possibilities. The mean value falls near 180 microns, but there is apparently something in the process which causes a large range of diameters, but a fairly consistent height. Since diameter is of secondary

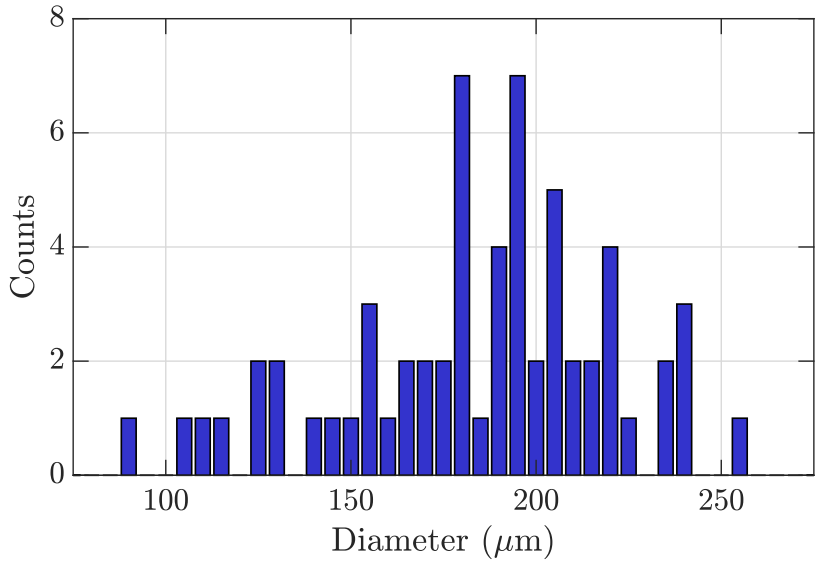

Figure 3.10: Histogram of the measured HAWT model trip device diameter, d. No distinction is made between different rows.

importance to the height where transition is concerned, it is expected that this will have little effect on the results.

3.3.2 Tripped Rotor Experimental Data Validation

Similar to the procedure outlined in section 3.1, the following details several validation test cases for the tripped rotor. Two Reynolds numbers were chosen of $Re_D = 5 \times 10^6$ and 7×10^6 at two tunnel pressures and with two different gearboxes. The results are shown in figure 3.11 for the power and thrust coefficients as a function of tip speed ratio. In general excellent collapse is seen across both metrics, increasing confidence in the results. Note that in a similar manner to the smooth case, the collapse is well within the error bars which indicates that the measurement uncertainty listed for the sensors may be conservative.

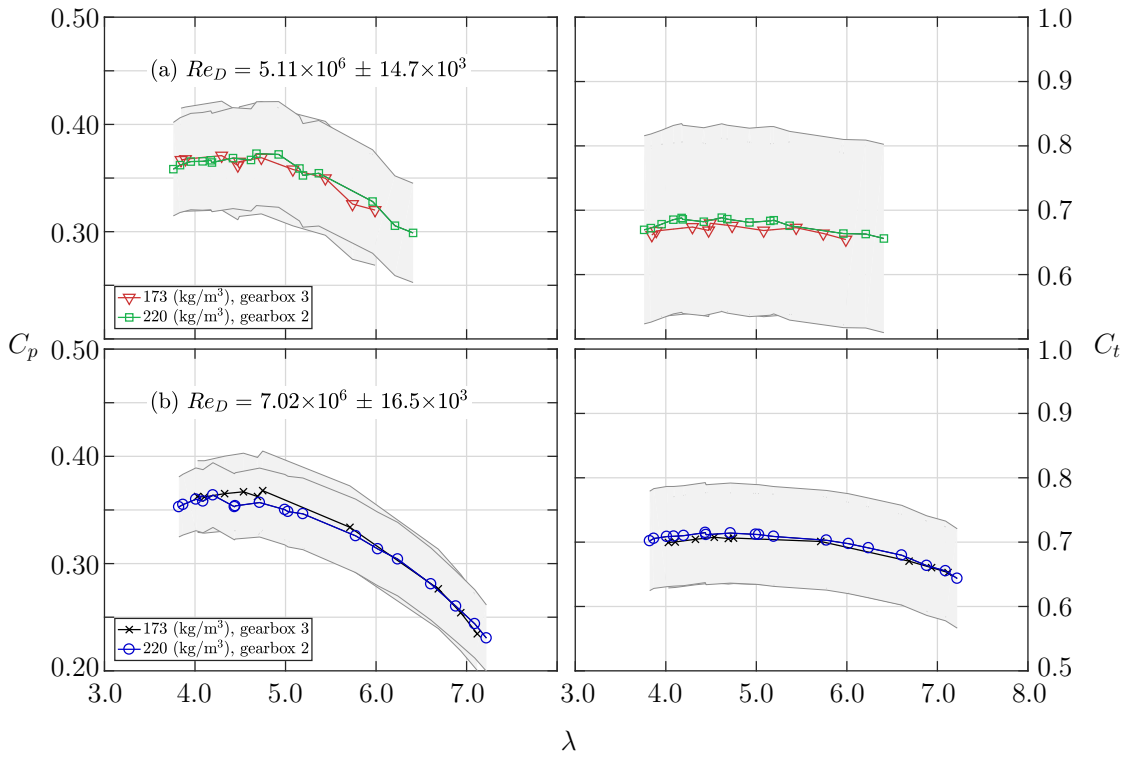

Figure 3.11: Validation cases for the model HAWT rotor with tripping devices. Legend applies to pairs of horizontal plots.

3.3.3 Tripped Rotor Performance

Plots of power and thrust coefficient for the tripped rotor are given in figure 3.12. Smooth rotor data from figures 3.3 (a) and (b) is shown for comparison at matched Reynolds numbers as gray symbols. For the power coefficient, invariance to the Reynolds number appears much sooner, with only small sections of the lowest Re_D case of 6×10^6 deviating slightly at the lowest values of λ. This result implies that whatever mechanism is causing the increased performance at lower Reynolds numbers is affected by transition. At this juncture, the conclusion only applies to this specific rotor geometry, it would be of great interest to see if the trend continues with other rotor geometries and at even lower values of Re_D which may be explored in future work.

Interestingly, a Reynolds number trend may also be observed in plots of the thrust coefficient, with higher Re_D corresponding to a larger C_t. This result is taken with

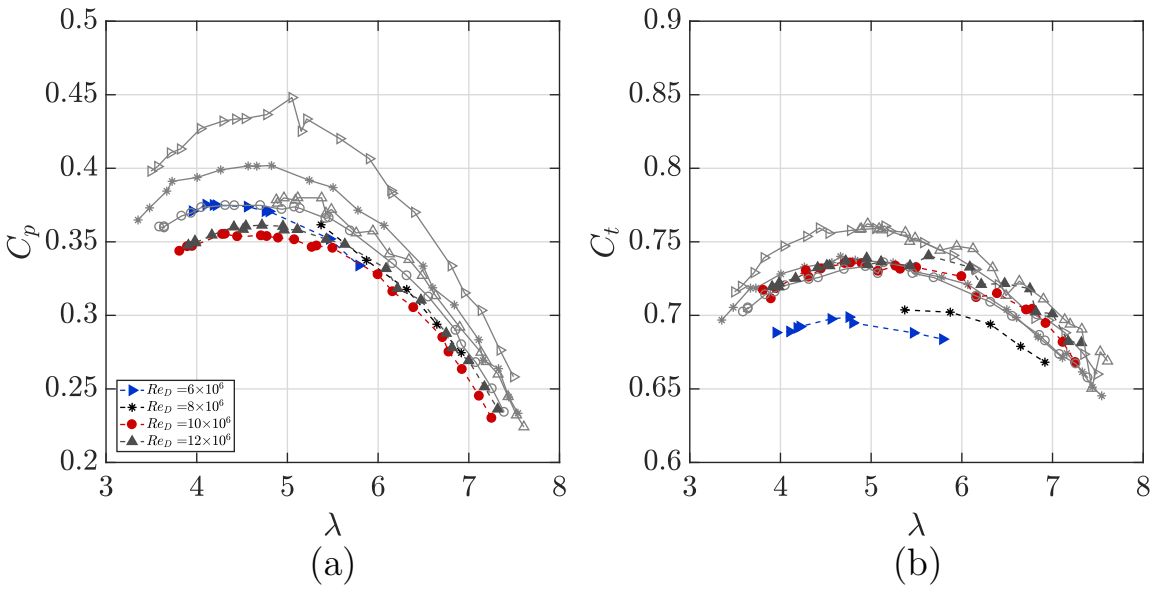

Figure 3.12: Reynolds number trends of the tripped HAWT rotor for power (a) and thrust (b) coefficients. Data of figure 3.3 is shown in gray with open symbols for reference. Legend applies to both plots (a) and (b).

some caution, due to the larger uncertainty of measurements from the load cell. It is hypothesized that an increase in blade Reynolds number would cause a larger drag on the airfoil due to the presence of the trips. Essentially the trip height becomes too large (i.e., $Re_k \geq 600$) with the overall effect being an increase in the total rotor thrust.

In a similar fashion to the smooth-rotor case, the data for the tripped rotor has been interpolated to a fixed λ grid to determine the Re_c trends. This is shown in figure 3.13 (a). Very little dependence is seen for any given tip speed ratio as Re_c is increased, suggesting that the trips effectively suppress the low Re behavior across all λ values. A slight overall decrease in the invariant power curve is seen in figure 3.13 (b). This would suggest that sectional drag has indeed increased along the rotor span without drastically altering the global flow phenomena at high Reynolds number. Further measurements would be required to confirm this hypothesis. Perhaps the most important conclusion of these two figures is that Reynolds number invariant behavior is achieved at much lower Re_c values than the smooth case. For

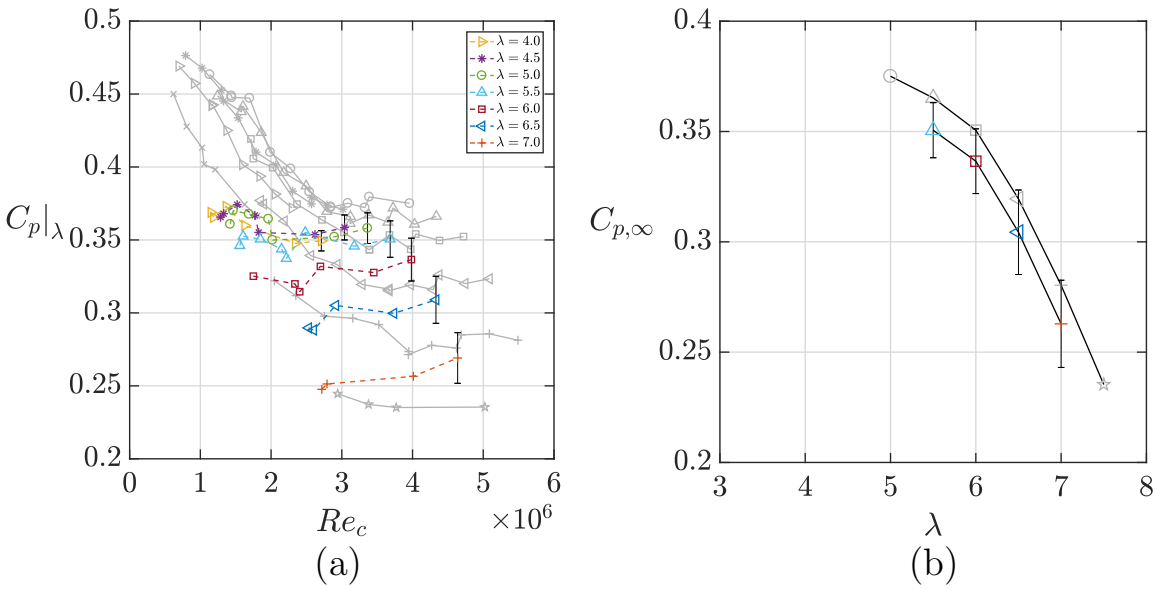

Figure 3.13: Power coefficient as a function of the local blade Reynolds number in (a) for a variety of fixed tip speed ratios, similar to figure 3.4. Figure (b) shows the Reynolds number invariant power curve for the model turbine geometry used under laminar inflow conditions. Smooth rotor data points are shown as gray symbols in both plots for reference.

the lower tip speed ratios of figure 3.13 (a), a cutoff value of $Re_c \geq 1.25 \times 10^6$ would be sufficient using available data points. It is possible this number could be significantly lower, but additional experiments are needed to confirm this trend

Finally, the invariant power curve of figure 3.13 (b) can be used to normalize the data of figure 3.13 (a) to evaluate the cutoff Reynolds number as shown in figure 3.14. The data exhibit good collapse at high Reynolds numbers, although some scatter is seen for C_p values which are below the cutoff Re. These points considered, the collapse is within 8% of the final value. Indicating that for the range of Re_c tested, invariant behavior is achieved almost immediately for the tripped rotor case. This confirms two conclusions made earlier, the first of which relates to experiments performed at lower Reynolds numbers (i.e., in traditional wind tunnels). These types of experiments may be able to attain an operating state which closely approximates the high-Re rotor by using properly sized tripping devices. The second conclusion is important with regard to the effect of performance enhancement at low-Re. Additional measurements would

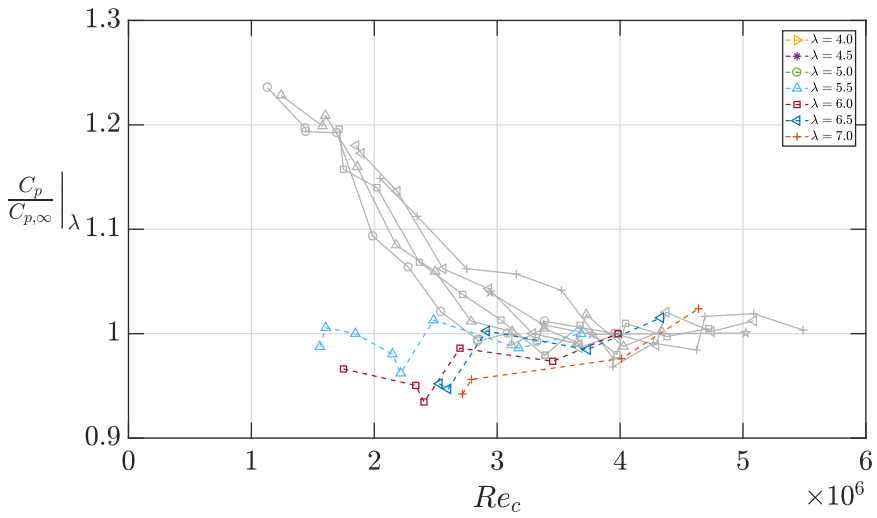

Figure 3.14: Power coefficient normalized by $C_{p,\infty}$ for the tripped HAWT rotor (color markers with dashed lines) compared with smooth rotor case (gray markers and solid lines).

need to be made on the rotor surface or in the wake to gain insight into which of the many mechanisms are causing the augmentation, but these experiments have shown that they are effectively disrupted by forcing transition on the rotor surface.

Chapter 4

Vertical Axis Wind Turbine Model at High Reynolds Numbers

While horizontal axis wind turbines have seen commercial success and continuous research support since the early days of wind energy, vertical axis wind turbines have been given much less attention. As discussed in the introduction of chapter 1 and section 1.5.2, significant work was completed in the area of VAWT aerodynamics, primarily by Sandia National Labs, during the 1980's. Some commercial units were even produced (FloWind, 1996), which saw moderate success in the United States, but then fell out of favor as the industry shifted to primarily focus on HAWT units. More recently, there has been renewed interest in VAWT aerodynamics (see e.g., Bhutta et al. (2012); Dabiri (2011); Lohry and Martinelli (2016); Miller et al. (2018)) as they may have the potential to fulfill niche markets not served by commercially available HAWTs. One of the primary reasons that VAWT designs have not had additional success in the marketplace is the increased difficulty associated with modeling these units. Even with steady inflow conditions, each blade undergoes highly unsteady processes within a single rotation. Due to the large changes in the local angle of attack on a given blade, stall often occurs even under ideal operating conditions.

Several researchers have produced BEM-type models which are adequate at giving shaft loadings but are generally only valid for low solidity turbines operating at high tip speeds (Islam et al., 2008; Paraschivoiu, 1981). What is lacking are additional reference cases with a variety of well-characterized inflow and operating conditions which can be used for developing new models and gaining understanding about VAWT operation. In addition, for these new experiments to be relevant to field-scale units, dynamic similarity remains a critical requirement. The purpose of this chapter is to address these shortcomings and provide additional insight into the behavior and performance of a VAWT turbine with changes in Reynolds number. The VAWT geometry used for these experiments is described in section 2.5 and is based on a commercially available unit with $N_b = 5$. The Reynolds number performance is discussed in detail for both power and thrust coefficients. These trends are found to scale well with a blade-based Reynolds number, which can be used to characterize the Re invariant behavior. The second part of this chapter deals with performance changes as the turbine solidity is altered by changing N_b, the blade number, and trends discussed.

4.1 Experimental Data Validation

In a similar approach to that of section 3.1, the VAWT experiments were validated by altering the tunnel pressure and free-stream velocity independently to achieve the same Reynolds number based on diameter, Re_D. This use of dynamic similarity allowed for completely different mechanical loads on the rotor and measurement stack, but should give collapse when plotted as non-dimensional power and thrust coefficient versus tip speed ratio. The plots (a) to (f) of figure 4.1 show the power coefficient for several Re_D values at different tunnel conditions and fixed $\sigma = 1.12$ ($N_b = 5$). Error bars in gray give the measurement uncertainty as outlined in section 2.8. Excellent

collapse is seen across all Reynolds numbers, reflecting the high degree of accuracy in the experimental results. The reduction in error-bar magnitude as Re_D increases is due to larger physical loads applied to the measurement stack, this has the effect of increasing the signal to noise ratio and results in higher accuracy as Reynolds number is increased.

Results for the thrust coefficient show a decidedly different trend. For the data shown in figure 4.8, very little collapse is observed. This is due to the large relative uncertainty of the thrust measurements in relation to shaft power. The only case which exhibits good collapse is the highest Reynolds number of figure 4.8 (f). This is in contrast to the results of the HAWT in figure 3.2 for C_t because the axial thrust force magnitude is lower for the VAWT due to the smaller frontal area (half of the HAWT). Thus the relative uncertainty is larger for this turbine, and is particularly evident at low Re_D values. These results make it difficult to draw conclusions for thrust coefficient trends with the Reynolds number.

4.2 Performance Scaling with Reynolds Number for the Five Blade Rotor

An extensive study of performance changes with Reynolds number was made for the $\sigma = 1.12$ ($N_b = 5$) rotor case as this geometry was a scaled model of a commercial field unit (Miller et al., 2018). The Reynolds number range was nominally: $5.80 \times 10^5 \leq Re_D \leq 5 \times 10^6$ for the experiments which overlapped with the field-turbine range of $7.44 \times 10^5 \leq Re_D \leq 2.44 \times 10^6$. The HRTF model of section 4.1, figure 4.7, show a strong Reynolds number dependence even when the value of Re_D is more than twice the maximum of the field unit. The point at which the power coefficient ceases to depend on the Reynolds number is of particular interest to wind turbine designers and manufacturers because it is directly linked to the potential profit a design will

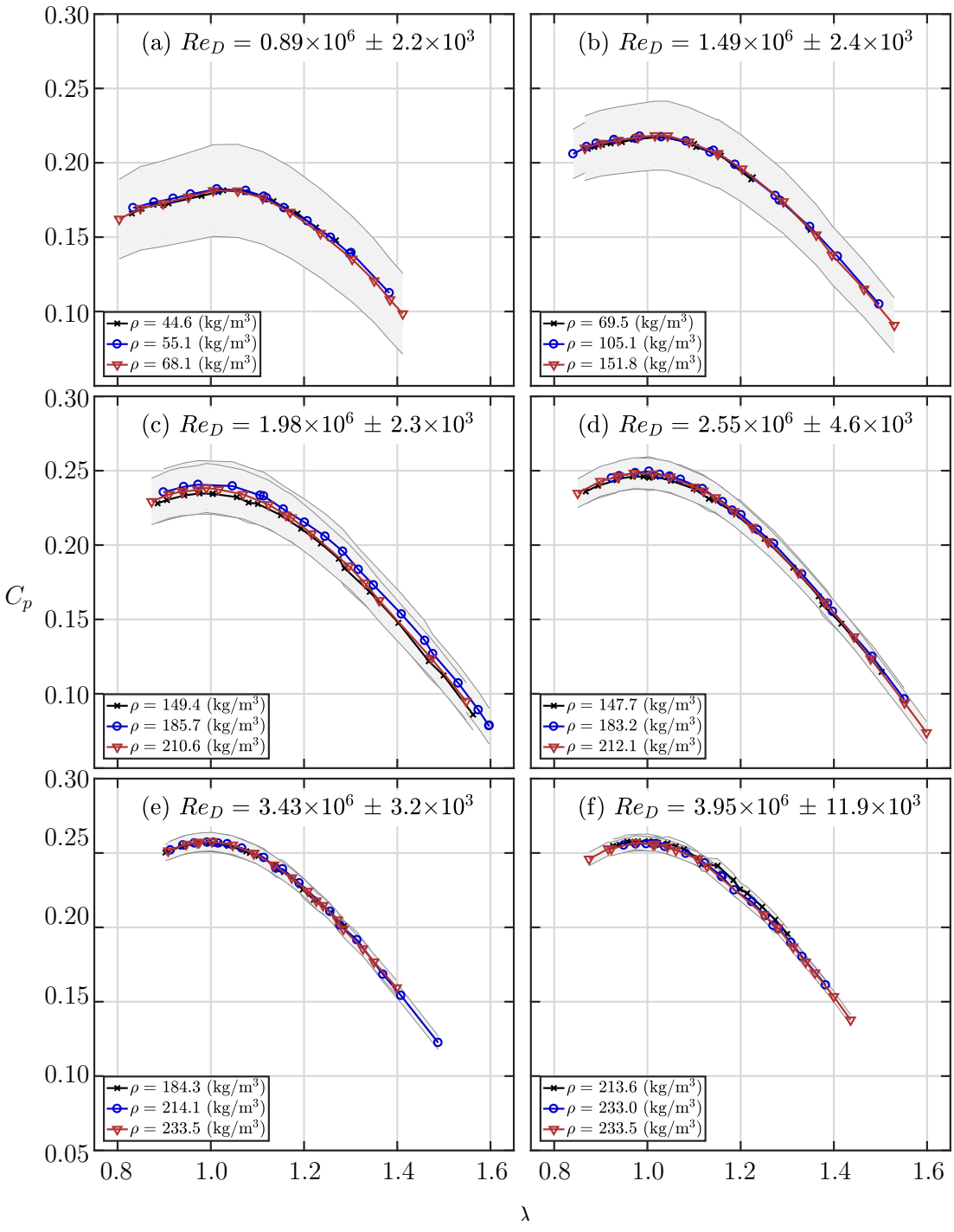

Figure 4.1: Data validation for the five blade VAWT model power coefficient as Reynolds number increases (from (a) to (f)). Data is shown referenced to the measured tunnel density.

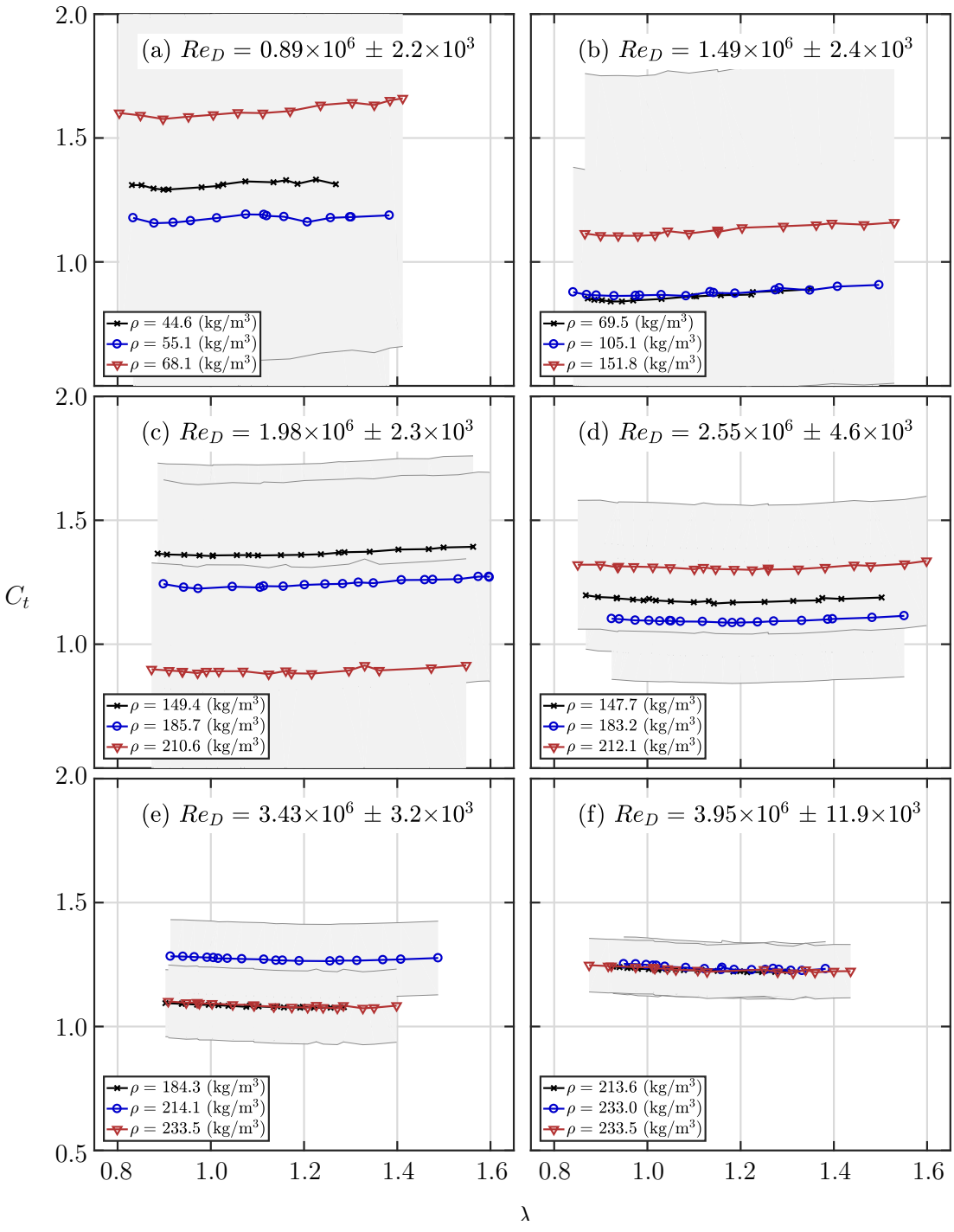

Figure 4.2: Data validation for the five blade VAWT model thrust coefficient as Reynolds number increases (from (a) to (f)). Data is shown referenced to the measured tunnel density.

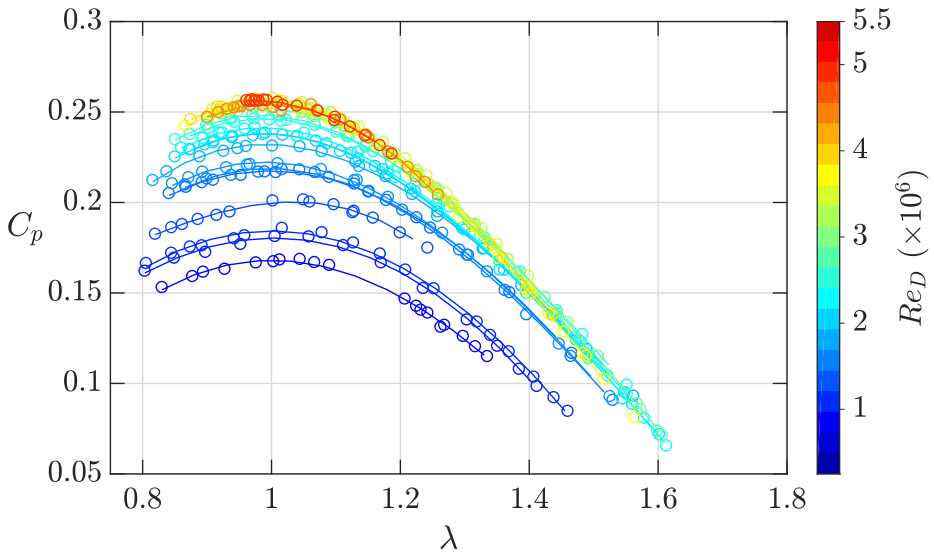

Figure 4.3: Reynolds number trends for the five blade VAWT model power coefficient as a function of tip speed ratio. Individual power curves are color-mapped to their respective mean Re_D, with the color-bar at right giving those values.

produce. For instance, when choosing the final size of a VAWT, increasing diameter slightly could net a bonus in C_p due to the larger Re with only a small penalty in increased cost.

This section describes in detail the variation of the power coefficient with Reynolds number. Similar to the HAWT results of section 3.2, support is found for using a Reynolds number based on local blade conditions (instead of free-stream values) in order to characterize the observed changes.

The power coefficient as a function of the tip speed ratio and Re_D is shown in figure 4.3. To better visualize trends, third-order polynomials have been fitted to the data and are shown as solid lines. A clear plateau behavior is seen when $Re_D \geq 3\times10^6$ for the peak C_p value near $\lambda \approx 1$. However, collapse appears to begin at a much lower value of Re_D for the high tip-speed ratio case as evidenced by the tight grouping of the curves at high λ. This is particularly evident for the light-blue case of $Re_D = 2.85\times10^6$ where collapse is clearly shown at $\lambda \geq 1.4$, but a dependence still exists near the peak in C_p at $\lambda = 1$. A two-parameter dependence indicates that a single non-dimensional

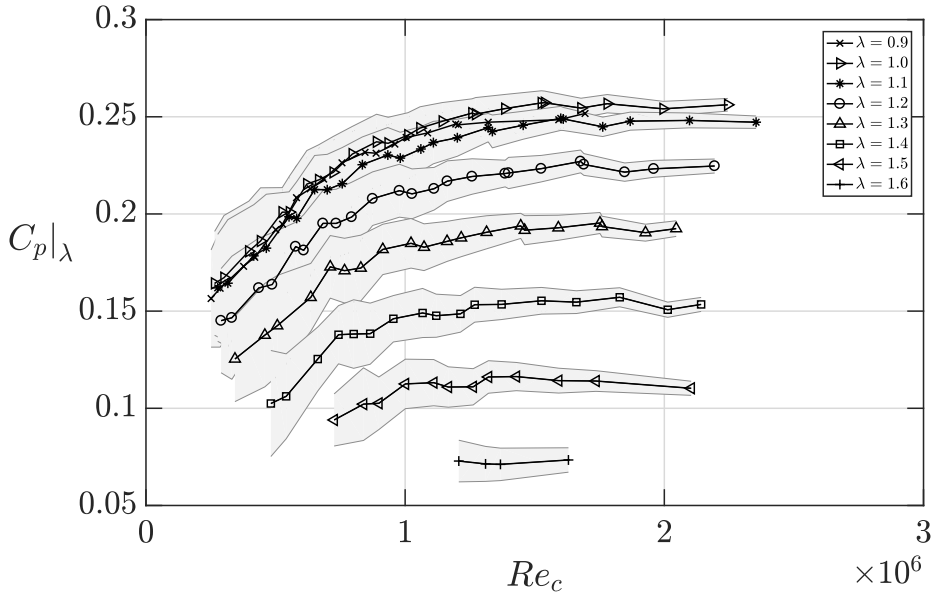

Figure 4.4: Power coefficient as a function of the blade Reynolds number as defined in equation 4.1 for the five blade VAWT model at various tip speed ratios.

group may better capture the behavior of C_p. For VAWT operation, a chord-based Reynolds number is defined as:

$$Re_c = \frac{\rho c(U + \omega R)}{\mu} = Re_D \frac{c}{D}(1 + \lambda) \tag{4.1}$$

which is distinct from the definition of Re_c used for the HAWT in equation 3.1. When computed, the value of Re_c given by equation 4.1 is the maximum blade Reynolds number a given VAWT blade could experience throughout a rotational cycle for a certain geometry and inflow condition. This definition has the benefit of also being convenient to calculate since measurements of the relative velocity are not possible with the current setup.

To investigate whether a single non-dimensional parameter can characterize the observed trends, the data of figure 4.3 have been interpolated to a fixed grid of λ values. The parameter Re_c can then be straightforwardly computed for various Re_D cases and the changes tracked via tip speed ratio. The resulting data points are shown in figure 4.4. A smooth transition is clearly evident from behavior where

$C_p|_\lambda$ depends on the blade Reynolds number; to an invariant state where additional increases in Re_c have no effect on the power coefficient. This invariant value of C_p can be denoted as $C_{p,\infty}$, where the subscript "∞" denotes that additional increases in Re_c will have no effect on the power coefficient magnitude. Reynolds number invariance is assumed after this point due to the very smooth plateau behavior of the power curves and large Reynolds numbers achieved (up to twice the field-scale unit). If a threshold is set on Re_c, the invariant behavior can then be quantified. From figure 4.4, this threshold was determined to be $Re_c \geq 1.5 \times 10^6$. The value of $C_{p,\infty}|_\lambda$ is then determined by averaging all values of $C_p|_\lambda$ above this threshold to reduce the small amount of scatter present in the experimental data sets. This gives the invariant power curve as a function of tip speed ratio, shown in figure 4.5. Any experiment or simulation with dynamic similarity to this one will return this power curve if $Re_c \geq 1.5 \times 10^6$, making it a powerful tool for comparison and validation. The benefit of defining Reynolds number invariance in this way is that power curves are objectively given by their Re_c value only, and not visual inspection (using, for example, figure 4.3). Furthermore, the limiting Reynolds number can be validated by normalizing the curves of figure 4.4 with their respective $C_{p,\infty}|_\lambda$ values. The resulting plot should give curves that approach unity. Incorrect choice for Re_c will cause under or overshooting as the limit is approached.

The resulting normalized curves are shown in figure 4.6 for all tip speed ratios. The cutoff $Re_c \geq 1.5 \times 10^6$ appears to capture the invariant behavior well, and a sharp knee is seen as the curves approach a value of one. It is not immediately apparent why this particular value of Re_c would be required for invariance but is likely related to the Reynolds number behavior of the airfoil chosen for this turbine. A surprising result of this figure is the change in $C_p|_\lambda$ per increment of Re_c does not depend on the tip speed ratio. The primary function of λ seems to be in determining the actual values of $C_{p,\infty}$, and hence the shape of the Reynolds invariant power curve. It

does not control the normalized slope of $C_p|_\lambda$ curves directly when $Re_c < 1.5 \times 10^6$, as clearly demonstrated in figure 4.6. The gradient with respect to λ in this intermediate region, where $251,200 \leq Re_c < 1.5 \times 10^6$, is apparently a constant for the five-blade configuration. The shape of this curve is well-captured by the curve fit (shown as a dashed gray line in figure 4.6):

$$\left.\frac{C_p}{C_{p,\infty}}\right|_\lambda = 0.3 \; erf\left(\frac{1.627 Re_c}{10^6} - 0.6443\right) + 0.7 \tag{4.2}$$

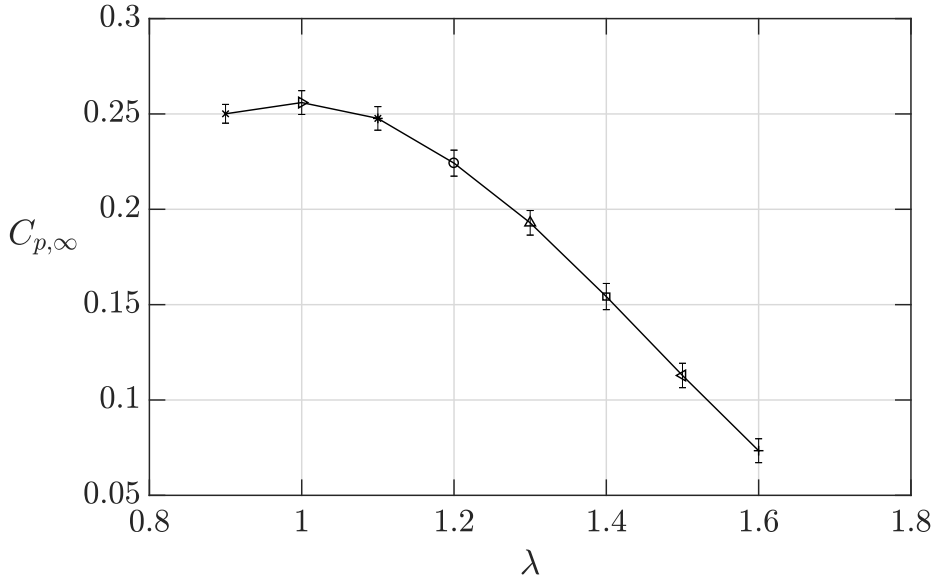

Figure 4.5: Reynolds invariant power curve as a function of tip speed ratio for the five blade VAWT rotor.

where erf indicates the error function. It may be possible to use this function as a correction for experiments and simulations performed at reduced Reynolds numbers. However, the lowest experimentally gathered Reynolds number falls at $Re_c = 251.2 \times 10^3$, below which the curve fit may not be valid. The shape of this curve is most likely a result of the rotor chosen, and is not necessarily universal to all VAWT geometries. The implications of this curve are still relevant to other cases, as it indicates that a single Reynolds invariant power curve and a few lower Re_c tests may be enough to completely characterize the scaling behavior of a VAWT turbine, at least under

conditions of laminar inflow. Section 4.3 continues this discussion by exploring the effect of changing solidity in the same context of Reynolds number invariance.

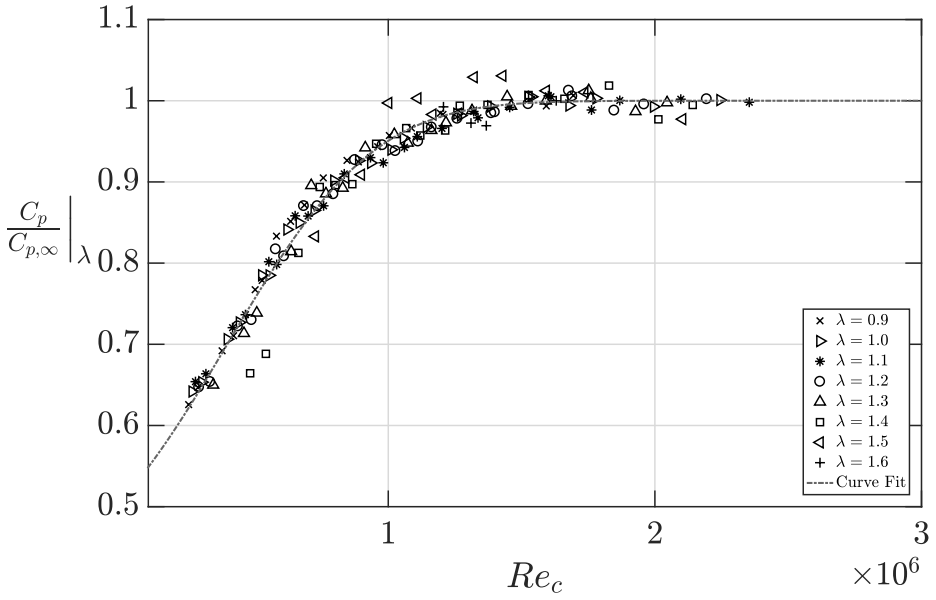

Figure 4.6: Power curves of figure 4.4 for the five blade VAWT model normalized by the invariant power coefficient for respective λ values.

4.3 Solidity Effects on Performance

Data sets for the $N_b = 2$, 3, and 4 blade case are compared as a function of Reynolds number in figure 4.7 and the data of figure 4.3 for the $N_b = 5$ blade rotor is shown for reference. The $N_b = 4$ case shows a higher maximum power coefficient accompanied by a slight shift to $\lambda = 1.1$ at this operating point. The trend continues for the $N_b = 3$ case as well, with max C_p typically occurring near $\lambda = 1.3$. The 2 blade behavior is not immediately clear, but C_p may be decreasing slightly with Re_D. The reason for this result may be the very large fluctuating loads present during nearly all two-blade rotor tests; in many cases the standard deviation of the shaft torque exceeded 50% of the mean. This became especially evident at the larger Reynolds numbers where shaft loading is large. The thrust coefficient for each turbine solidity at the same Re_D values is shown in figure 4.8. In general the value of C_t was large, often exceeding

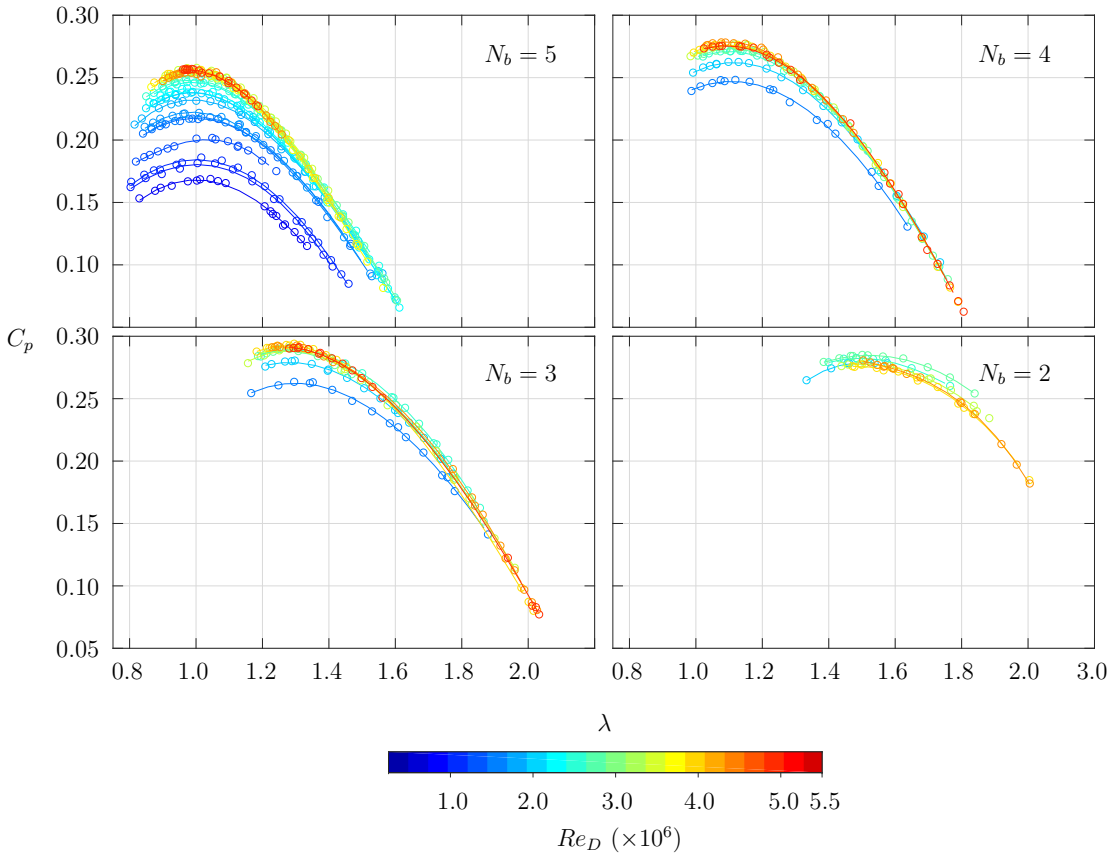

Figure 4.7: Power coefficient as a function of tip speed ratio for four different VAWT rotor solidities. Color gives the mean Re_D value for each power curve.

unity for most operating points. No discernible Reynolds number trend is evident for any solidity. The $N_b = 2$ rotor does report a much lower thrust coefficient value than any other solidity. This is in contrast to the trend between the $N_b = 5$, 4 and 3 blade rotor where a fairly constant $C_t \approx 1.2$ is observed. An interesting tightening of trends with Re_D appears to occur between these three solidities, the cause of which is currently unknown.

In an effort to more fully quantify Reynolds number changes with C_p for all rotor solidities, plots of the type shown in figure 4.4 have been generated for the various σ values. These employ the definition of Re_c given by equation 4.1, which does not directly take into account the turbine solidity changes caused by altering N_b. Error

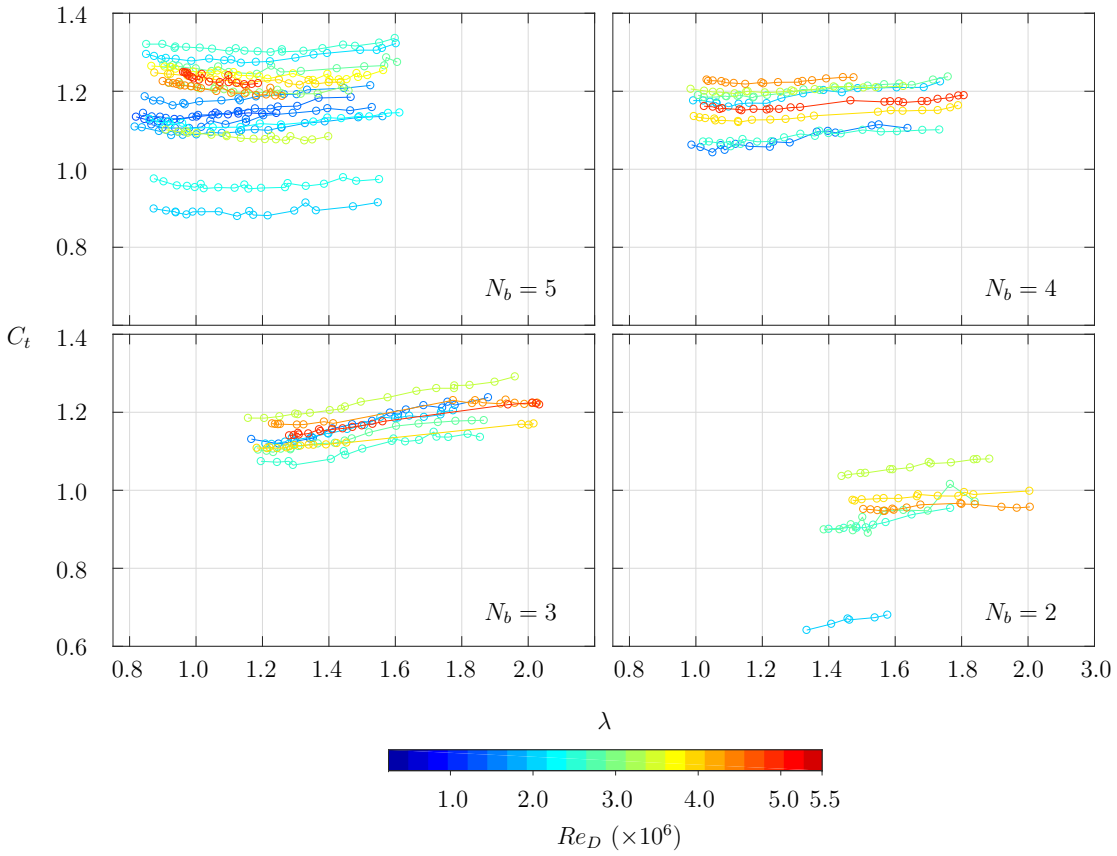

Figure 4.8: Thrust coefficient as a function of tip speed ratio for four different rotor solidities. Color gives the mean Re_D value for each power curve.

bars representing the measurement uncertainty have also been included. These results are shown in figure 4.9.

Determining the location of optimal turbine operation is then very straightforward. As mentioned for the 5 blade case, this typically occurs near $\lambda = 1$ for all Reynolds numbers, although there is some overlap at lower values of Re_c. The 4 blade case clearly prefers to operate at slightly higher tip speed ratios, with data below λ of unity not present as the rotor would typically come to rest if this operating point was requested. Peak power resides at $\lambda = 1.1$ for all Re_c values, as noted previously. Additional high Reynolds number data is available for the 3 blade case due to several data sets acquired at two higher Re_D values of 5.94×10^6 and 7.160×10^6. These were not shown in figure 4.7 as they displayed good collapse with the $Re_D = 5 \times 10^6$ case,

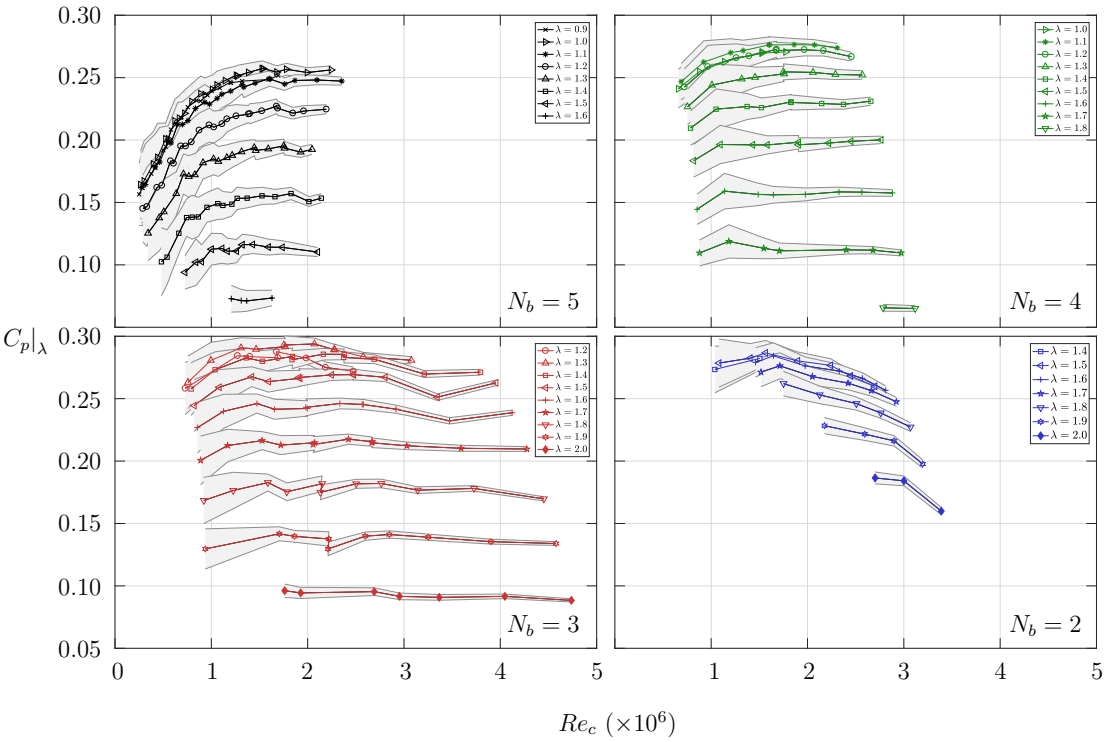

Figure 4.9: Power coefficient for the VAWT model at various solidities as a function of blade Reynolds number. Symbol indicates the tip speed ratio.

but are given here as further evidence of Re_c independence. These three solidities then clearly display Re_c invariant behavior which is well captured by the threshold $Re_c = 1.5 \times 10^6$ chosen earlier for the 5 blade rotor. This might be somewhat surprising since N_b is not an input to Re_c, however it enters indirectly as the solidity has an effect on the operational λ range. Results from the 2 blade rotor are less clear, as already noted. Figure 4.9 shows a different trend for this solidity with the value of C_p decreasing as Re_c increases for all tip speed ratios. It may be that this lower solidity requires higher Re_c values to show invariance or that the highly fluctuating loads are causing errors in determining the mean quantities. During the 2 blade experiments, a failure occurred on the model which caused a rotor blade to break, highlighting the large mechanical loads which often exceeded the original design space of the model.

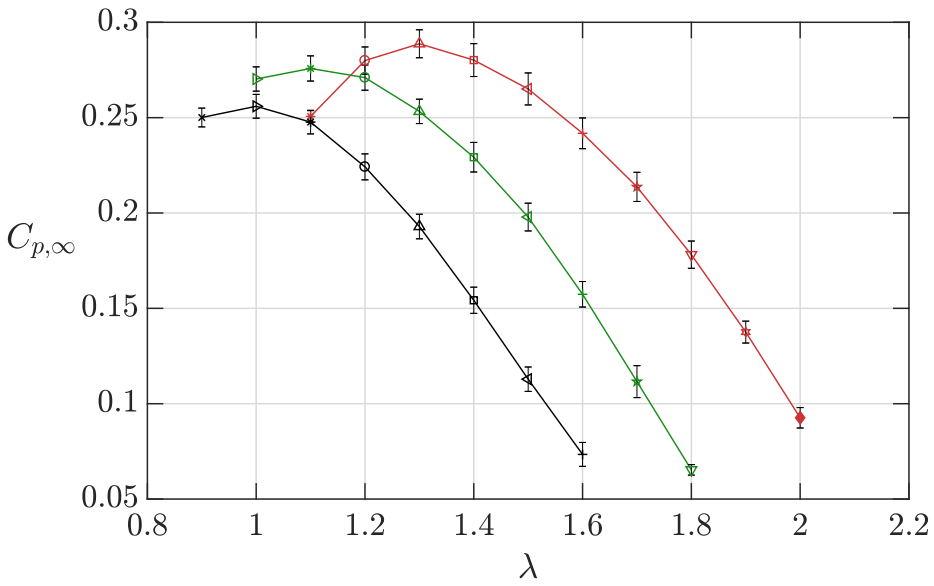

Figure 4.10: Reynolds invariant power coefficient as a function of tip speed ratio for varying solidity. Color indicates solidity/blade number: $\sigma = 1.12$ ($N_b = 5$) are black; $\sigma = 0.9$ ($N_b = 4$) are green; $\sigma = 0.67$ ($N_b = 3$) are red.

Results from other works can also be evaluated using the Re_c criterion. Lohry and Martinelli (2016) defined Re_c in the same manner as (but independently of) this work. The data presented in figure 16 of that work shows the peak C_p for various solidities as a function Re_c. The authors do not give a specific value for which invariance should be observed, as a small increasing trend is still seen even at the highest Re_c tested which approached 100×10^6. However some plateau-like behavior is observed to occur as soon as $Re_c = 2 \times 10^6$ for the $\sigma = 0.25$ case, with larger solidities possibly needing a slightly higher Re_c value for invariance. Where field data is concerned, the work of Worstell (1979) gives the power coefficient as a function of blade Reynolds number, although a slightly different definition of Re_c is used. When converted to the value of Re_c used in this thesis, figure 14 of that work shows invariant behavior in $C_{p,\max}$ when $Re_c = 1.45 \times 10^6$. This is a surprising result as the turbine geometry is very different and the solidity is low at $\sigma = 0.14$. Combined with the results presented here, all of these works indicate that the current definition of Re_c may well characterize Reynolds number dependence for a number of VAWT geometries and solidities.

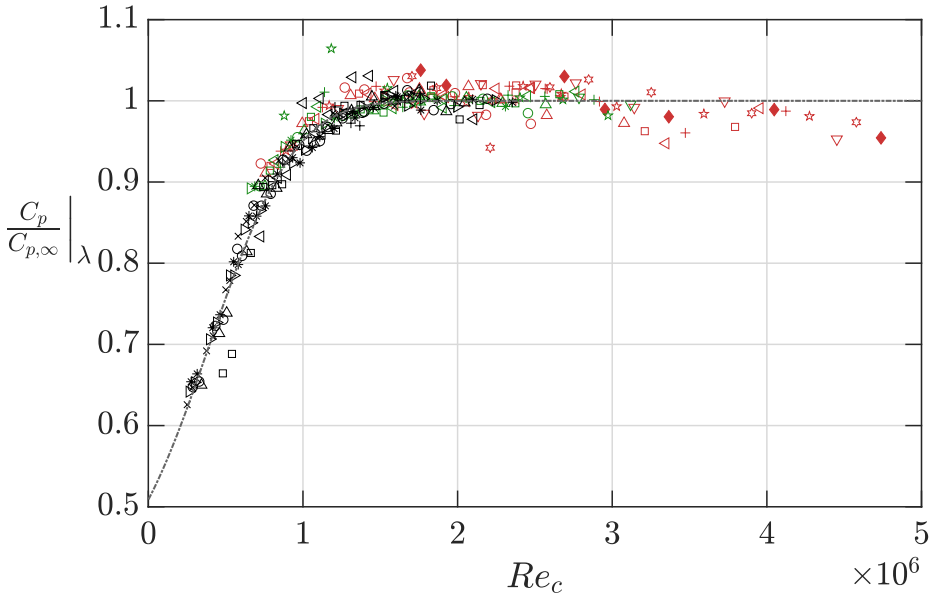

Figure 4.11: Power coefficient normalized by the Reynolds invariant value for three different VAWT rotor solidities. Symbol indicates λ, as in figures 4.9 and 4.5. Color indicates solidity/blade number: $\sigma = 1.12$ ($N_b = 5$) are black; $\sigma = 0.9$ ($N_b = 4$) are green; $\sigma = 0.67$ ($N_b = 3$) are red. Dashed gray line is the curve fit from equation 4.1.

The invariant power curves derived using the same threshold of $Re_c \geq 1.5 \times 10^6$ as figure 4.5 are shown for the various solidities in figure 4.10. The $N_b = 2$ blade data was not included because invariant behavior was not observed in figure 4.9. These are the power curves which will be returned by a VAWT of any size which has dynamic similarity with these experiments provided the Reynolds number is high enough. The increase in performance and tip speed ratio is clearly evident as σ is reduced.

Finally, the data of figure 4.9 was normalized with the invariant power coefficients of figure 4.10 by tip speed ratio. The result is shown in figure 4.11 for the three solidities $\sigma = 1.12$ ($N_b = 5$), $\sigma = 0.9$ ($N_b = 4$), and $\sigma = 0.67$ ($N_b = 3$) along with the curve fit given by equation 4.2. In general, excellent collapse is seen for the 4 and 5 blade data to a single curve all the way out to the highest tested Re_c values of 3 million. The 3 blade data also collapses well in this region, with a possible slight decrease noticed for the $Re_c > 3 \times 10^6$, with the largest deviating point still remaining within 5.5% of the invariant $C_{p,\infty}$ value.

The results of this section have shown that achieving Reynolds number invariance is possible in the laboratory setting for the VAWT. A large number of data sets at various Re_D values were acquired and validated by using the unique capabilities of the HRTF. An objective measure of Reynolds invariant behavior was determined by defining a blade Reynolds number specific to the VAWT operation which allows for comparison between data sets acquired at different combinations of Re_D and λ. A threshold was determined by inspection at $Re_c \geq 1.5 \times 10^6$, above which the mean value of $C_p|_\lambda$ gives the invariant power coefficient. This is the C_p value returned by a turbine operating in dynamic similarity (exactly scaled geometry and laminar inflow conditions) with the models tested in these experiments. Furthermore, some support was found in the literature for using the definition of Re_c to characterize invariance to Reynolds number. Finally the invariant power coefficient was used to normalize the curves of $C_p|_\lambda$; which consistently returned the same gradient change with Re_c for the three different solidities $\sigma = 1.12$, 0.9, and 0.67.

Chapter 5

Conclusions

A specialized, high pressure wind tunnel was employed to quantify the effect of altering the Reynolds number on both horizontal and vertical axis wind turbine models. An unprecedented range of Reynolds numbers were achieved using the unique capabilities of the facility, adding to and expanding upon the very small number of previous laboratory works performed at these Re values. Furthermore, the data sets acquired could specifically focus on Reynolds number effects as tip speed ratio can be completely decoupled from the free-stream Re_D value. This has never before been accomplished for wind turbine studies. The ability to adjust fluid density independent of the velocity also permitted extensive experimental data validation in a manner not possible with unpressurized facilities.

Performing these experiments did come with the additional challenge of very large model loads. This necessitated the design and manufacture of numerous parts with specific attention given to the loading conditions and forces encountered in the wind tunnel. Among the equipment produced in the course of this thesis was a complete tower and gearbox assembly for the HAWT, a bespoke measurement stack and mounting system for the tunnel, a fully-instrumented test rig located outside of the tunnel for gearbox efficiency quantification, plus two complete wind turbine models

for horizontal and vertical axis studies. Developing the HAWT tower and gearbox combination encompassed the span of one and a half years of work alone. The final product is an assembly which survives many high-speed, high-torque rotor experiments with no observed degradation in quality or performance. The test rig was a key component of the drive-train development, and allowed for precise quantification of the power lost inside the gearbox. The result of this large investment of time and energy was that trends in the power coefficient could be assessed to a very high level of confidence not possible in any other HAWT experiment.

The horizontal axis model was tested over a broad range of Reynolds number values, from $4 \times 10^6 \leq Re_D \leq 14 \times 10^6$ or in terms of the chord-Reynolds number $620,000 \leq Re_c \leq 5.5 \times 10^6$ at tip speed ratios from $3.5 \leq \lambda \leq 7.5$. The chord-based Reynolds number was found to best characterize changes in performance with Reynolds number, with invariant behavior clearly evident for $Re_c \geq 3.5 \times 10^6$. Using this threshold value, the invariant power curve was found which is the curve any dynamically similar experiment using this rotor geometry will return if Re_c is above this threshold value. Results indicated that the slope of C_p with Re_c as this limit is approached was constant, independent of the specific Re_D and λ chosen to achieve a particular Re_c. This lead to the hypothesis that the tip speed ratio had the effect of determining the numeric value of $C_{p,\infty}$, but not how this limit was approached. In addition, it indicated that once the invariant C_p curve is known, only a few additional low Reynolds number experiments are needed to quantify the Re behavior. This has direct implications for modeling, numerical simulations, and future experiments.

The smooth HAWT rotor was also tested with tripping devices attached to the leading edge of the rotor. The goal was to further understanding of surface roughness effects on turbine performance when the full-scale non-dimensional parameters are matched. The geometry of these trips was specified so as to cause the flow to transition while avoiding excessive drag. Due to the high Reynolds numbers and small size of

the rotor, a number of different approaches were evaluated for applying the micron-scale trips. The final method involved careful placement of epoxy micro-dots in two staggered rows near the rotor leading edge on both the pressure and suction side of the rotor. The trip geometry was well characterized, with numerous measurements of the applied trips made with confocal microscopy so that replicating these details is straightforward. The effect of tripping the rotor was to hasten the transition to high Re_c behavior, at least where the power coefficient was concerned. This can also be considered a lowering of the threshold Reynolds number needed for invariance of C_p with Re. The direct implication is that a tripped rotor operating at lower Reynolds number can approximate the performance of a smooth turbine at much larger Re values. The invariant power curve showed a slight overall decrease with respect to the smooth rotor, which is to be expected due to the presence of the trips. The major conclusion from the tripped rotor experiments was that whatever mechanism is behind the low Reynolds number performance enhancement of the smooth rotor is apparently in some way related to transition and can be disrupted by prematurely forcing the boundary layer on the rotor into a turbulent state.

Experiments with the vertical axis wind turbine were also undertaken with the same motivation to further understand Reynolds number effects for the canonical case of laminar inflow. Data validation was again performed to check the validity of all measurements by repeating Reynolds number cases several times at various combinations of density and velocity. The five-blade rotor was initially examined as it matched the scaled geometry of an actual field turbine, although the Re_D values achieved in the HRTF were twice as high as measured in the field. Reynolds number trends were characterized in detail for this wide range spanning an entire order of magnitude from $500,000 \leq Re_D \leq 5 \times 10^6$. Initially the power coefficient showed an increase commensurate with larger Re_D values, and then displayed clear plateau behavior once the Reynolds number was sufficiently large. Slight variation was ob-

served in this behavior as a function of λ, indicating that another non-dimensional parameter could more effectively characterize Reynolds number effects on C_p. Considering the method of VAWT operation, a chord-based Reynolds number was defined using the maximum velocity possible at the blade, the chord length, and free-stream fluid properties. Power coefficient plotted as a function of this new Reynolds number clearly exemplified invariance when $Re_c \geq 1.5 \times 10^6$. This threshold Re_c value was found to characterize all tip speed ratios tested. To further evaluate the validity of using the chord-based Reynolds number to quantify Re effects, a number of different solidities were also tested by reducing the blade number from five to four, three, and two. The same methodology was applied to these results as the five blade rotor, with power coefficient invariance observed for the three and four blade rotors but not the two. The threshold Re_c value which characterized C_p invariance of the five blade rotor was also found to apply to the three and four blade versions. This was a surprising result as the performance of the turbine is clearly affected by solidity, whereas the Reynolds number effects have no direct dependency. Therefore solidity and tip speed ratio determined the Reynolds invariant power coefficient value, but do not directly alter the threshold at which invariance occurs. Finally the three, four, and five blade rotor power curves were normalized with their respective invariant values. The resulting curve showed excellent agreement among all three solidities. This again having the direct result that once the invariant power curve is known, only a small number of additional experiments are needed to retrieve the Reynolds number dependency of a particular rotor. There is even some indication that the definition of Re_c and the limit found for the VAWT is more universally appropriate for numerous geometries and operating conditions.

For the first time, the Reynolds dependent behavior of the horizontal and vertical axis wind turbine have been experimentally demonstrated for a wide range of Re which encompasses field-scale values. This has provided a first look into scaling effects

and the important case of Reynolds number invariance for turbine operation. The setup and results presented here provide a solid foundation on which future studies into a multitude of turbine operational parameters can be made. For instance, the well characterized experiments described here can be used as a baseline of comparison for off-design conditions such as the case of HAWT mis-alignment with the incoming flow (yaw), unsteady operation such as startup and shutdown, and drive-train control studies could all be made with direct aerodynamic coupling. Furthermore, detailed investigations of the turbine wake can be made with the goal of understanding wake development, structure, and turbulent properties.

Bibliography

Akbari, M. H. and Price, S. J. (2003). Simulation of dynamic stall for a NACA 0012 airfoil using a vortex method. *Journal of fluids and structures*, 17(6):855–874.

Armstrong, S., Fiedler, A., and Tullis, S. (2012). Flow separation on a high Reynolds number, high solidity vertical axis wind turbine with straight and canted blades and canted blades with fences. *Renewable Energy*, 41:13–22.

Ashok, A., Van Buren, T., and Smits, A. (2015). Asymmetries in the wake of a submarine model in pitch. *Journal of Fluid Mechanics*, 774:416–442.

Bahaj, A. S., Molland, A. F., Chaplin, J. R., and Batten, W. M. J. (2007). Power and thrust measurements of marine current turbines under various hydrodynamic flow conditions in a cavitation tunnel and a towing tank. *Renewable Energy*, 32(3):407–426.

Bak, C., Johansen, J., and Andersen, P. B. (2006). Three-dimensional corrections of airfoil characteristics based on pressure distributions. In *Proceedings of the European Wind Energy Conference*, pages 1–10.

Banks, W. H. H. and Gadd, G. E. (1963). Delaying effect of rotation on laminar separation. *AIAA journal*, 1(4):941–941.

Bhutta, M. M. A., Hayat, N., Farooq, A. U., Ali, Z., Jamil, S. R., and Hussain, Z. (2012). Vertical axis wind turbine–a review of various configurations and design techniques. *Renewable and Sustainable Energy Reviews*, 16(4):1926–1939.

Blackwell, B. F., Sheldahl, R. E., and Feltz, L. V. (1976). Wind tunnel performance data for the Darrieus wind turbine with NACA 0012 blades. Technical Report SAND76-0130, Sandia Laboratories, Albuquerque, N. Mex. (USA).

Blanco, M. I. (2009). The economics of wind energy. *Renewable and sustainable energy reviews*, 13:1372–1382.

Braslow, A. L. and Knox, E. C. (1958). Simplified method for determination of critical height of distributed roughness particles for a boundary layer transition at Mach numbers from 0 to 5. Technical Report 4363, National Advisory Committee for Aeronautics, Langley, VA (US).

Carr, L. W. (1988). Progress in analysis and prediction of dynamic stall. *Journal of aircraft*, 25(1):6–17.

Chamorro, L. P., Arndt, R. A., and Sotiropoulos, F. (2011). Reynolds number dependence of turbulence statistics in the wake of wind turbines. *Wind Energy*, 15:733–742.

Chaviaropoulos, P. K. and Hansen, M. O. L. (2000). Investigating three-dimensional and rotational effects on wind turbine blades by means of a quasi-3D Navier-Stokes solver. *Journal of Fluids Engineering*, 122(2):330–336.

Chen, T. and Liou, L. (2011). Blockage corrections in wind tunnel tests of small horizontal-axis wind turbines. *Experimental Thermal and Fluid Science*, 35:565–569.

Cotrell, J., Stehly, T., Johnson, J., Roberts, J. O., Parker, Z., Scott, G., and Heimiller, D. (2014). Analysis of transportation and logistics challenges affecting the deployment of larger wind turbines: summary of results. Technical Report TP-5000-61063, National Renewable Energy Lab, Golden, Col. (USA).

Dabiri, J. O. (2011). Potential order-of-magnitude enhancement of wind farm power density via counter-rotating vertical-axis wind turbine arrays. *Journal of renewable and sustainable energy*, 3(043104).

de Vries, O. (1983). On the theory of the horizontal-axis wind turbine. *Annual Review of Fluid Mechanics*, 15:77–96.

Drela, M. (1989). XFOIL: An analysis and design system for low Reynolds number airfoils. Low Reynolds number aerodynamics lecture notes.

Du, Z. and Selig, M. S. (2000). The effect of rotation on the boundary layer of a wind turbine blade. *Renewable Energy*, 20(2):167–181.

Dumitrescu, H., Cardoş, V., and Dumitrache, A. (2007). Modelling of inboard stall delay due to rotation. In *Journal of Physics: Conference Series*, volume 75 of *012022*. IOP Publishing.

Ehrmann, R. S., Wilcox, B., White, E. B., and Maniaci, D. C. (2017). Effect of surface roughness on wind turbine performance. Technical Report SAND2017-10669, Sandia National Laboratories, Albuquerque, N. Mex. (USA).

Elford, C. M. (2015). High Reynolds number hydrokinetic turbine force analysis and test equipment design. Online.

FloWind (1996). Final project report: High energy rotor development, test and evaluation. Technical Report SAND96-2205, Sandia Laboratories and FloWind Corporation.

Glauert, H. (1935). Airplane propellers. In *Aerodynamic theory*, pages 169–360. Springer, Berlin, Germany.

Guntur, S. (2013). *A detailed study of the rotational augmentation and dynamic stall phenomena for wind turbines*. PhD thesis, Technical University of Denmark, Department of Mechanical Engineering, Nils Koppels Allé, Building 403, DK-2800 Lyngby, DK. PhD-0022.

Hansen, A. C. and Butterfield, C. P. (1993). Aerodynamics of horizontal-axis wind turbines. *Annual Review of Fluid Mechanics*, 25(1):115–149.

Hansen, M. H., Gaunaa, M., and Madsen, H. A. (2004). A Beddoes-Leishman type dynamic stall model in state-space and indicial formulations. Technical Report Risø-R-1354, Forskningscenter Risoe, (DK).

Hansen, M. O. L. (2007). *Aerodynamics of Wind Turbines*, volume 17. Earthscan.

Islam, M., Ting, D. S., and Fartaj, A. (2008). Aerodynamic models for darrieus-type straight-bladed vertical axis wind turbines. *Renewable and Sustainable Energy Reviews*, 12:1087–1109.

Jacobs, E. N. and Sherman, A. (1937). Airfoil section characteristics as affected by variations of the Reynolds number. Technical Report 586, National Advisory Committee for Aeronautics, Langley, VA (US).

Jamieson, P. (2018). *Innovation in wind turbine design*. John Wiley & Sons.

Jiménez, J. M., Hultmark, M., and Smits, A. J. (2010). The intermediate wake of a body of revolution at high Reynolds numbers. *Journal of Fluid Mechanics*, 659:516–539.

Jiménez, J. M., Reynolds, R., and Smits, A. J. (2000). Preliminary velocity measurements in the wake of a submarine model. In *APS Division of Fluid Dynamics Meeting Abstracts*, volume 1.

Keyence Corporation (2018). Introduction to roughness. Online. Accessed: 08-08-2018.

Kiefer, J., Miller, M. A., Hultmark, M., and Hansen, M. O. (2016). Effects of finite aspect ratio on wind turbine airfoil measurements. *Journal of Physics Conference Series*, 753(022040).

Kundu, P. K. and Cohen, I. M. (2008). *Fluid Mechanics*. Elsevier, fourth edition.

Laneville, A. and Vittecoq, P. (1986). Dynamic stall: the case of the vertical axis wind turbine. *Journal of Solar Energy Engineering*, 108(2):140–145.

Larsen, J. W., Nielsen, S. R. K., and Krenk, S. (2007). Dynamic stall model for wind turbine airfoils. *Journal of Fluids and Structures*, 23(7):959–982.

Lee, M. K. K. (2015). Small-scale vertical axis wind turbine design for testing and optimization in the Princeton high Reynolds number test facility. Online.

Lindenburg, C. (2004). Modelling of rotational augmentation based on engineering considerations and measurements. In *European Wind Energy Conference, London (UK)*, pages 22–25.

Llorente, E., Gorostidi, A., Jacobs, M., Timmer, W., Munduate, X., and Pires, O. (2014). Wind tunnel tests of wind turbine airfoils at high Reynolds numbers. *Journal of Physics: Conference Series*, 524(012012).

Loftin, L. K. J. and Bursnall, W. J. (1948). The effects of variations in Reynolds number between 3.0×10^6 and 25.0×10^6 upon the aerodynamic characteristics of a number of NACA 6-series airfoil sections. Technical Report 1773, National Advisory Committee for Aeronautics, Langely, VA (US).

Lohry, M. W. and Martinelli, L. (2016). Unsteady Reynolds-averaged Navier-Stokes simulation of crossflow rotors, scaling, and blockage effects. *AIAA Journal*, 54(12):3828–3839.

Lorber, P. F. and Carta, F. O. (1988). Airfoil dynamic stall at constant pitch rate and high Reynolds number. *Journal of Aircraft*, 25(6):548–556.

Madsen, H. A. and Christensen, H. F. (1990). On the relative importance of rotational, unsteady and three-dimensional effects on the HAWT rotor aerodynamics. *Wind Engineering*, pages 405–415.

Madsen, H. A., Mikkelsen, R., Øye, S., Bak, C., and Johansen, J. (2007). A detailed investigation of the blade element momentum (BEM) model based on analytical and numerical results and proposal for modifications of the BEM model. *Journal of Physics: Conference Series*, 75(1).

McCroskey, W. J. (1981). The phenomenon of dynamic stall. Technical Report 81264, National Aeronautics and Space Administration, Moffett Field, California (USA).

Mikkelsen, R. F. (2004). *Actuator disc methods applied to wind turbines*. PhD thesis, Technical University of Denmark, Department of Mechanical Engineering, Nils Koppels Allé, Building 403, DK-2800 Lyngby, DK. MEK-FM-PHD 2003-02.

Miley, S. J. (1982). A catalog of low Reynolds number airfoil data for wind turbine applications. Technical report, Texas A&M University.

Miller, M. A., Duvvuri, S., Brownstein, I., Lee, M., Dabiri, J. O., and Hultmark, M. (2018). Vertical axis wind turbine experiments at full dynamic similarity. *Journal of Fluid Mechanics*, 844:707–720.

Miller, M. A., Kiefer, J., Westergaard, C., and Hultmark, M. (2016). Model wind turbines tested at full-scale similarity. *Journal of Physics: Conference Series*, 753(032018).

Mueller, T. J. (1985). The influence of laminar separation and transition on low Reynolds number airfoil hystersis. *Journal of Aircraft*, 22:763–770.

Øye, S. (1991). Dynamic stall simulated as time lag of separation. In *Proceedings of the 4th IEA Symposium on the Aerodynamics of Wind Turbines*, Rome, Italy.

Paraschivoiu, I. (1981). Double-multiple streamtube model for Darrieus wind turbines. In *Wind Turbine Dynamics*.

Phidd, A. (2015). Design, manufacturing, and analysis of a horizontal axis wind turbine for high Reynolds numbers. Online.

Pires, O., Munduate, X., Ceyhan, O., Jacobs, M., and Snel, H. (2016). Analysis of high Reynolds numbers effects on a wind turbine airfoil using 2D wind tunnel test data. *Journal of Physics: Conference Series*, 753.

Ramsay, R. R., Hoffman, M. J., and Gregorek, G. M. (1996). Effects of grit roughness and pitch oscillations on the S801 airfoil. Technical Report TP-442-7818, National Renewable Energy Lab, Golden, Col. (USA).

Reynolds, R. M. (1953). Preliminary results of an investigation of the effects of spinner shape on the characteristics of an NACA D-type cowl behind a three-blade propeller, including the characteristics of the propeller at negative thrust. Technical report, DTIC Document.

Robinson, M. C., Hand, M. M., Simms, D. A., and Schreck, S. J. (1999). Horizontal axis wind turbine aerodynamics: three-dimensional, unsteady, and separated flow influences. In *Proceedings of FEDSM99 3rd ASME/JSME Joint Fluids Engineering Conference*.

Sanderse, B., van der Pijl, S., and Koren, B. (2011). Review of computational fluid dynamics for wind turbine wake aerodynamics. *Wind Energy*, 14:799–819.

Sardar, A. M. (2001). *Centrifugal fans: similarity, scaling laws, and fan performance*. PhD thesis, State University of New York at Buffalo.

Schepers, J. and Snel, H. (2007). Model experiments in controlled conditions. Report ENC-E-07-042, ECN.

Schepers, J. G. (2012). *Engineering models in wind energy aerodynamics: development, implementation and analysis using dedicated aerodynamic measurements*. PhD thesis, Delft University of Technology, Delft, Netherlands.

Schepers, J. G., Boorsma, K., Bon, A., Kim, C., and Cho, T. (2011). Results from Mexnext: Analysis of detailed aerodynamic measurements on a 4.5 m diameter rotor placed in the large German Dutch wind tunnel DNW. Technical Report ECN-M-11-034, Energy Research Center of the Netherlands, Petten, (NL).

Schlichting, H. (2000). *Boundary-Layer Theory*. McGraw-Hill, New York (USA), eigth edition.

Schreck, S. and Robinson, M. (2002). Rotational augmentation of horizontal axis wind turbine blade aerodynamic response. *Wind Energy*, 5(2-3):133–150.

Schreck, S. and Robinson, M. (2004). Tip speed ratio influences on rotationally augmented boundary layer topology and aerodynamic force generation. *Journal of solar energy engineering*, 126(4):1025–1033.

Schreck, S., Sant, T., and Micallef, D. (2010). Rotational augmentation disparities in the MEXICO and UAE phase VI experiments. In *In Proceedings of the 3rd EWEA Conference - Torque 2010*.

Sheldahl, R. E., Klimas, P. C., and Feltz, L. V. (1980). Aerodynamic performance of a 5-metre-diameter Darrieus turbine with extruded aluminum NACA-0015 blades. Technical Report SAND80-0179, Sandia Laboratories, Albuquerque, N. Mex. (USA).

Shigley, J. E., Budynas, R. G., and Mischke, C. R. (2004). *Mechanical engineering design*. McGraw-hill.

Simms, D., Schreck, S., Hand, M., and Fingersh, L. J. (2001). NREL Unsteady Aerodynamics Experiment in the NASA-Ames wind tunnel: a comparison of predictions to measurements. Report TP-500-29494, National Renewable Energy Lab, Golden, Col. (USA).

Smits, A. J. (2009). Viscous Flows and Turbulence. Lectures in Fluid Mechanics.

Snel, H., Houwink, R., Bosschers, J., et al. (1994). Sectional prediction of lift coefficients on rotating wind turbine blades in stall. Technical Report ECN-C-93-052, ECN.

Snel, H., Schepers, J. G., and Montgomerie, B. (2007). The MEXICO project (Model Experiments in Controlled Conditions): the database and first results of data processing and interpretation. In *Journal of Physics: Conference Series*, volume 75, page 012014. IOP Publishing.

Somers, D. M. and Tangler, J. L. (2000). Wind tunnel tests of two airfoils for wind turbines operating at high Reynolds numbers. Technical report, National Renewable Energy Lab., Golden, CO (US).

Spera, D. A. (2009). *Wind Turbine Technology: Fundamental Concepts in Wind Turbine Engineering*. ASME Press, second edition.

Strickland, J. H. (1975). The Darrieus turbine: a performance prediction model using multiple streamtubes. Technical Report SAND-75-0431, Sandia Laboratories, Albuquerque, N. Mex. (USA).

Tang, L. (2017). Design of a small-scale vertical axis wind turbine for testing in the Princeton high Reynolds number test facility and comparison to full-scale turbines. Online.

Vallikivi, M., Hultmark, M., and Smits, A. J. (2015). Turbulent boundary layer statistics at very high Reynolds number. *Journal of Fluid Mechanics*, 779:371–389.

van Kuik, G., Peinke, J., Nijssen, R., Lekou, D., Mann, J., Sørensen, J., Ferreira, C., van Wingerden, J., Schlipf, D., Gebraad, P., Polinder, H., Abrahamsen, A., van Bussel, G., Sørensen, J., Tavner, P., Bottasso, C., Muskulus, M., Matha, D., Lindeboom, H., Degraer, S., Kramer, O., Lehnhoff, S., Sonnenschein, M., Sørensen, P., Künneke, R., Morthorst, P., and Skytte, K. (2016). *Long-term research challenges in wind energy - a research agenda by the European Academy of Wind Energy*. Springer.

Vermeer, L., Sørensen, J., and Crespo, A. (2003). Wind turbine wake aerodynamics. *Progress in Aerospace Sciences*, 39:467–510.

Vestas Corporation (1994). *General Specifications Vestas V27-225 kW, 50 Hz. Windturbine*.

Viterna, L. A. and Janetzke, D. C. (1982). Theoretical and experimental power from large horizontal-axis wind turbines. Technical Report NASA-TM-82944, National Aeronautics and Space Administration, Lewis Research Center, Cleveland, OH (US).

Wiser, R., Hand, M., Seel, J., and Paulos, B. (2016). Reducing wind energy costs through increased turbine size: Is the sky the limit? Technical report, Lawrence Berkeley National Laboratory, Berkeley, CA (USA).

Worstell, M. H. (1979). Aerodynamic performance of the 17-metre-diameter Darrieus wind turbine. Technical Report SAND78-1737, Sandia Laboratories, Albuquerque, N. Mex. (USA).

Zagarola, M. V. (1996). *Mean-flow scaling of turbulent pipe flow*. PhD thesis, Princeton University, Princeton, NJ, USA.

Appendix A

HAWT Tower and Gearbox Design

This appendix covers the design methodology for the horizontal axis wind turbine model tower and gearbox. The tower and support structure were designed to accurately locate the rotor at the tunnel centerline, transfer all forces and shaft power generated to the measurement stack while minimizing deflections, and limit wake disturbances by having a small frontal area and externally representing a realistic tower geometry. An initial discussion is given for the highest loading cases which could be encountered by an ideal model operating in the facility. These parameters are used as input to the gearbox design equations. The section concludes with a discussion of results from the finite element analysis performed on the tower/nacelle.

A.1 Operating Envelope

The base rotor geometry was chosen to minimize tunnel blockage, keep rotational rates mechanically feasible, and produce features which are machinable with standardized processes. For these reasons a model diameter of $D = 20$ (cm) was chosen as the baseline case, which gives a blockage of $A_{rotor}/A_{tunnel} = 16.7\%$. In addition, the

smaller feature sizes were estimated to be the airfoil sections at the rotor tip, with a chord length on the order of 1 to 10% of the radius. This range gives chord lengths which are on the order of 1 to 10 (mm). Even if relatively thin airfoils are selected, such as 14%, the airfoil thickness from chords of 3.6 (mm) upwards should be realizable with standard machining practices given a minimum thickness of 0.5 (mm) (per our manufacturer, QMMLine Incorporated).

The maximum turbine power was then estimated at the extreme case using the theoretical Betz's limit of $C_{p,\text{Betz}} = 16/27$ and an assumed $C_t = 1.0$, the upper limit of turbine performance can be estimated as a function of tunnel conditions, provided a value of λ is specified. This type of analysis was undertaken to preliminarily quantify the model loads for a number of tip speed values, an example plot using $\lambda = 5.0$ is shown in figure A.1 to give an idea of the operating space.

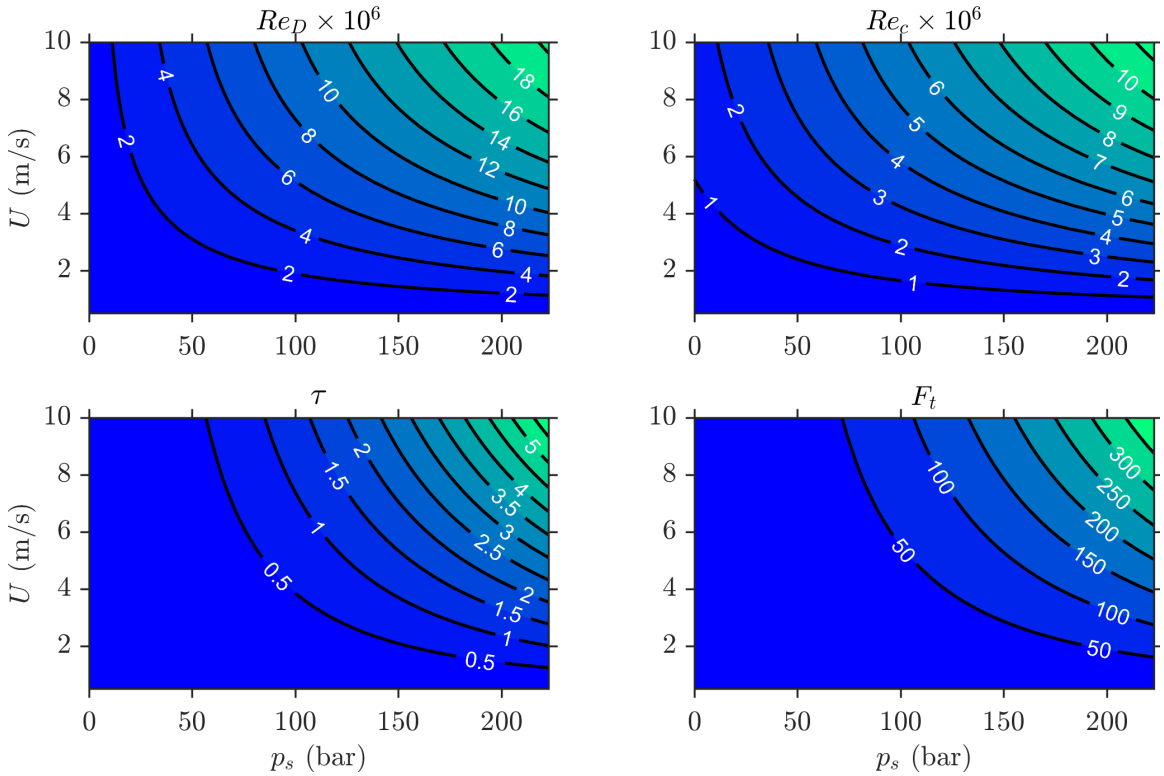

Figure A.1: Operating space plots for a model with $D = 20$ (cm) and $\lambda = 5.0$ with an assumed $C_p = 16/27$ and $C_t = 1$.

For the model, it was assumed that access would be needed to the full range of λ from near zero at startup to values approaching ten. Based on this the range, the rotational speeds could approach 1000 (rad/s) or $9,550$ (r.p.m.) for a free-stream velocity of 10 (m/s). Note that these are the maximum possible values which could be seen given the theoretical capabilities in the HRTF wind tunnel, in reality the operating conditions were typically much lower, especially the rotational speeds, during actual experiments.

A.2 Shaft and Gear Analysis

With the basic input loads determined, the analysis could continue by determining how these loads enter the tower support structure via the input shaft and gearbox assembly. The gearbox was designed to use straight-cut miter gears, which by definition are 1:1 ratio and mounted at right angles to each other. The reaction forces acting on miter gears can be broken down into components:

$$W_t = \text{Tangential force} = \tau / r_{avg} \tag{A.1}$$

where τ is the torque acting on the shaft, and r_{avg} is the pitch radius at the midpoint of the gear tooth (Shigley et al., 2004). Denoting the pressure angle of the gear as ϕ and the cone angle as γ, the additional reaction forces can be found as:

$$W_r = \text{Radial force} = W_t \tan(\phi) \cos(\gamma) \tag{A.2}$$

.

$$W_a = \text{Axial force} = W_t \tan(\phi) \sin(\gamma) \tag{A.3}$$

The diagram of figure A.2 gives both the free-body reaction forces and the input torque τ_{in}. In principle, the input torque enters indirectly via the loads generated at

the gear which are in turn supported by the bearings. The axial thrust force, F_t, is assumed to always enter in the negative x direction as shown in the diagram.

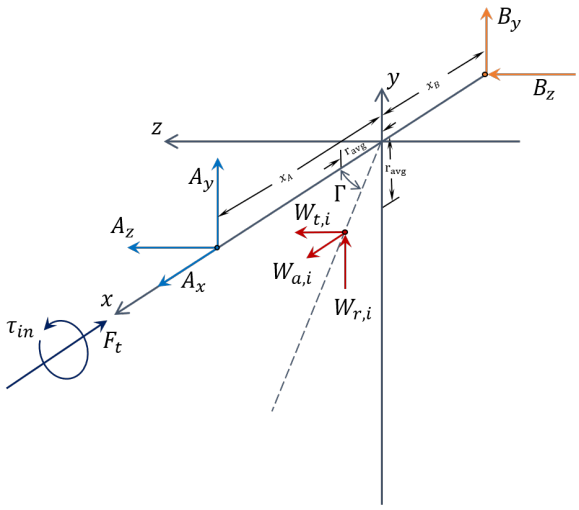

Figure A.2: Free body diagram of the gearbox input shaft. Note that in this configuration, bearing A takes the thrust loading.

Balancing the forces in Y, Z, and X:

$$A_y + B_y + W_r = 0 \tag{A.4}$$

$$A_z + B_z + W_t = 0 \tag{A.5}$$

$$-F_t + A_x + W_a = 0 \tag{A.6}$$

An interesting result of this arrangement is that the axial gear reaction force W_a acts in the opposite direction of any applied thrust force. Thus this configuration inherently reduces the loading on the bearings instead of one where the gear is located on the negative side of the x axis. The moments are then straightforward to solve, using the right hand rule to determine sign. Summing moments about the Y axis (Z-X plane):

$$A_z(x_A + x_B) + W_t(r_{avg} + x_B) = 0 \tag{A.7}$$

Similarly about the Z axis (Y-X plane):

$$A_y(x_A + x_B) + W_r(r_{avg} + x_B) + W_a r_{avg} = 0 \tag{A.8}$$

which gives the reaction forces in terms of the gear loadings for both bearings. This analysis is repeated for the output shaft with the difference being that the gear is outboard the bearings. Using figure A.3, this results in:

$$D_x = \frac{r_{avg}(W_r + W_a) + W_r r_{avg}}{y_C - y_D} - W_r \tag{A.9}$$

$$D_z = W_t \left(\frac{r_{avg} - y_D}{y_C - y_D} - 1 \right) \tag{A.10}$$

$$C_x = \frac{W_r y_D - r_{avg}(W_r + W_a)}{y_C - y_D} \tag{A.11}$$

$$C_y = -W_a \tag{A.12}$$

$$C_z = \frac{W_t y_D - W_t r_{avg}}{y_C - y_D} \tag{A.13}$$

$$\tau_{out} = W_t r_{avg} \tag{A.14}$$

The final equation needed to solve the free-body is the output shaft tangential force, found via an equal and opposite reaction on the gear surface such that $W_{t,o} = -W_{t,i}$, $W_{r,o} = -W_{r,i}$, and $W_{a,o} = -W_{a,i}$. Following determination of the reaction forces, the shear and bending moment diagrams are generated for each section of the shaft. To complete the fatigue analysis, these static bending moments and the torque acting on the shaft are used to find the von-Mises stress at various locations along the length. The factor of safety was then calculated at each critical location using a Modified-Goodman criterion (see Shigley et al. (2004), page 299). Critical locations were determined to be the locating holes for the miter gear pins, which are just visible on the lower gear shoulder in figure A.4.

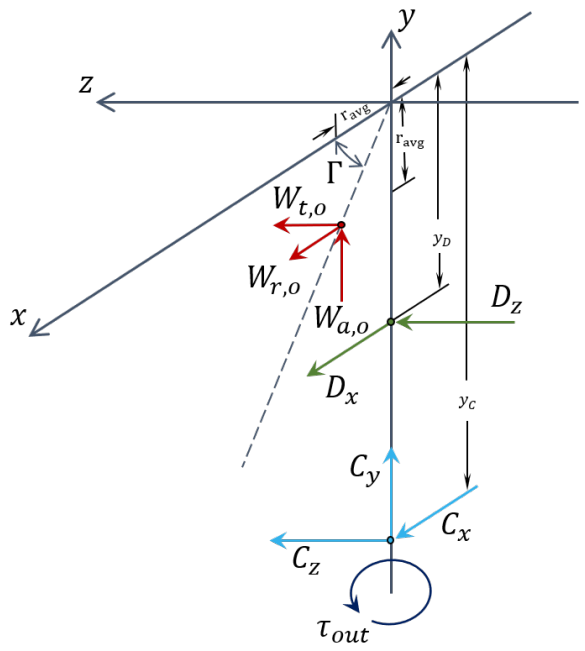

Figure A.3: Free-body diagram of the output shaft. In this configuration bearing C receives the thrust loading.

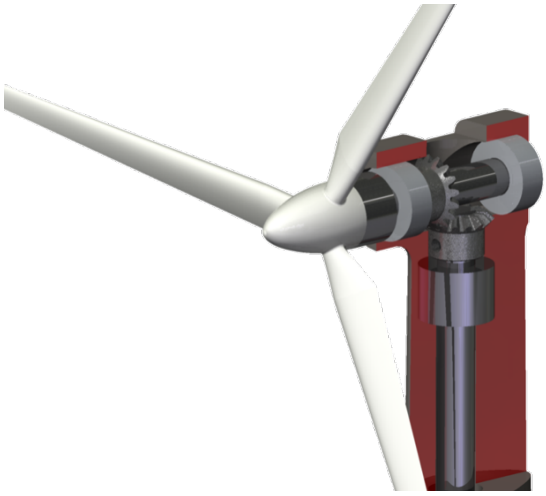

Figure A.4: Cut-away computer rendering of the gearbox during the design phase. Rotor geometry shown for reference.

Ultimately the method of gear attachment involved pressing rolled spring pins through a mounting hole in the gear and into a matching hole on the shaft. Despite the penalty due to the stress-concentrations at the hole, this was an effective means of axially locating the gear and transmitting torque to the shaft.

Equations for determining the maximum stress and factor of safety were programmed into a Matlab function. The final design had a factor of safety of 1 at the gear location when the axial torque was set to 3 (Nm) and the thrust load was 300 (N). In practice, the gearbox can withstand this high torque level, but not for extended periods of time and not if the dynamic loading considerations are taken into account. Test-rig measurements indicated that a maximum shaft torque value of 1.2 (Nm) could be sustained almost indefinitely as long as rotational speeds were kept below $4,000$ (r.p.m.). The gearbox is also very sensitive to the surface treatment of the gears themselves, and it was elected to have them carbo-nitride surface hardened to improve lifetime and wear properties. Finally, great care must be exercised when assembling the gearbox as even the slightest mis-alignment or incorrect setting of tolerances by even as much as ± 25 (microns) or ± 0.001 (inches) can cause premature failure of the gearbox. These effects are difficult to capture in any model of this type. However, this conservative approach led to a design which will robustly withstand high shaft torque loads, with the failure point being the gears themselves. This is a useful design feature as no catastrophic harm comes to the rotor or measurement stack when this occurs. Typically the rotor will stop or move to a free-spin condition, while the output shaft remains stationary. A typical HAWT gearbox lasts through many experiments, and when a failure occurs the unit can be quickly re-built in house for very low cost.

A.3 Tower and Nacelle Design

This section focuses only on the choice of geometry for the nacelle and tower, which are a single unit in the HAWT model. Typical wind turbine towers are cylindrical in shape, often with slight taper towards the top. However, there is no fixed design for commercial wind turbine towers and often research-type turbines use a scaffolding

support structure (especially the early work on turbines, see Spera (2009) for some examples). For the purposes of these experiments, it is advantageous to make the turbine tower and nacelle as compact as possible with some aerodynamic shape to reduce the drag on the assembly.

The final tower geometry chosen resembles a smoothed diamond shape, which allowed for maximum interior volume and a minimum of deflections as determined by the finite-element simulations. A cross-section of the tower geometry is represented graphically in figure A.5. This profile, with the long-axis aligned with the incoming flow, was defined in the tower part file as the section at the tunnel centerline (i.e., interior to the nacelle) while the base was defined at the tunnel wall but with all outer dimensions increased by 3 (mm), which produced a tapered tower. The two sections defined the boundaries of a blend where the intermediate geometry was interpolated by the computer aided design program CREO.

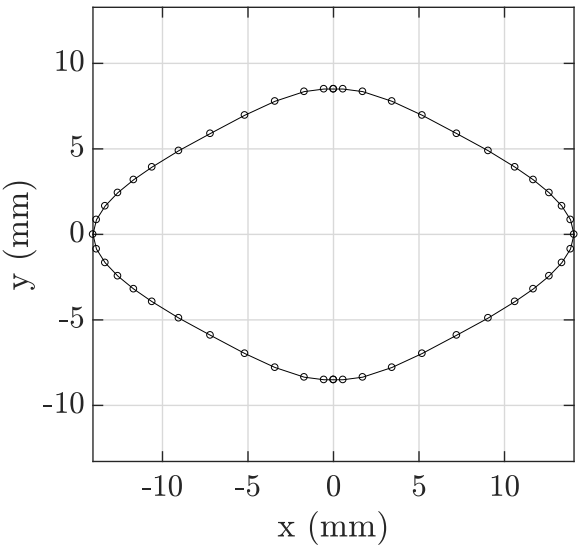

Figure A.5: Cross-section of the tower profile.

A number of simulations of the tower were performed with the finite-element package available in CREO known as Simulate. The goal of these simulations was to check both the maximum von-Mises stress inside the part and calculate the maximum tower deflection. Input loads inside the tower were determined via the equations of

section A.2 for a given thrust loading and shaft torque. A summary of the results is shown in table A.1 for a range of shaft torques with fixed thrust load and vice-versa. It would appear that shaft torque has a large influence on the material stress, while thrust force does not. There are some shaft torque loads which should be avoided as the stress values approach the yield-strength of most alloy steels. However as mentioned in section 2.4.2, the maximum shaft loading is limited by the gears themselves to values of 1.2 (Nm) or below, and therefore the tower strength and deflection values are sufficient.

Table A.1: Finite element simulation results for the tower with various applied loads.

τ_{in} (Nm)	$F_{t,\text{in}}$ (N)	Max. von-Mises Stress (MPa)	Max. Deflection (mm)
1	300	68.9	0.35
3	300	130	0.37
5	300	222	0.42
7	300	313	0.48
3	50	126	0.16
3	100	135	0.19
3	500	129	0.59